Quantum Computing Using Native Interaction in Superconducting Circuits

Takahiro Tsunoda

Wolfson College, University of Oxford

A thesis submitted for the degree of

Doctor of Philosophy

Trinity term 2021

Supervised by Dr. Peter J. Leek

Quantum Computing Using Native Interaction in Superconducting Circuits

Takahiro Tsunoda, Wolfson College, University of Oxford

Trinity Term 2021

Abstract of thesis submitted for the degree of Doctor of Philosophy

Superconducting circuits form one of the most promising hardware platforms for building a quantum computer. As the quantum computing system gets more complex as we increase the size, employing simple circuit designs and control strategies can make the task of building a large scale quantum computer easier.

This thesis describes a novel control strategy that utilises spin-echo techniques and native interaction in superconducting circuits, which reduces the cost of calibrating pulsed two-qubit gates. Spin-echo pulses are used to rescale the always-on Hamiltonian, and the timings of spin-echo pulses encode the effective coupling strengths. In collaboration with the NMR group in Oxford, two methods for scaling this technique to large numbers of qubits were explored. In the first approach, pulse sequences for an all-to-all coupled system are obtained numerically using linear programming, and it finds the time-optimal solution for up to twenty qubits and the near time-optimal solution for up to hundreds of qubits. Another approach based on graph colouring finds the near time-optimal pulse sequence analytically, allowing pulse sequences for any number of qubits. An idea based on the Hamiltonian rescaling technique was applied to implementing the variational quantum eigensolver algorithm and error mitigation on two superconducting qubits. In contrast to previous studies, the residual dispersive coupling between qubits was used for computation instead of regarding it as a source of error.

Lastly, the detailed dynamics of the residual dispersive coupling in superconducting circuits were investigated to predict the practicality of spin-echo-based quantum computing on superconducting circuits. The Hamiltonian rescaling protocol assumes the always-on coupling to be diagonal, such as Ising Hamiltonian, but deviation from the pure Ising interaction was observed in the strongly coupled superconducting qubits. The origin of the deviation was identified analytically, and the circuit design criteria to suppress the deviation are presented.

ACKNOWLEDGEMENTS

Countless people supported me during the PhD. Here, I would like to acknowledge the contributions of some of them who made this journey possible and rewarding.

First and foremost, I want to express my sincere gratitude to my supervisor, Dr. Peter Leek. Working with you on Coaxmon, scaling it up, and exploring new ideas on this platform was a remarkable experience. I appreciated the scientific culture in the lab you fostered and enjoyed honest and rigorous scientific discussions with you. Your genuine approach to science is an inspiration for me today. I thank my co-supervisor, Professor Simon Benjamin, for introducing me to a novel area of research on near-term quantum algorithms and quantum error mitigation. My dissertation benefited from a unique direction thanks to the collaboration with the NMR group led by Professor Jonathan Jones.

I acknowledge the generous support of the Nakajima Foundation and the Masason Foundation, who provided me with the financial means to pursue this research project. I appreciate Wolfson College and Sir Tim Hitchens for creating a diverse and welcoming community and for offering me various forms of support during my time at the college.

I would like to express my gratitude to my colleagues in the Leek lab for their support and collaboration throughout this project. In particular, I want to thank Andrew Patterson for inspiring me to use parasitic coupling as a computational resource. What started as a casual coffee chat turned into a fascinating research direction. I also want to acknowledge Joseph Rahamim's guidance and expertise in building a Circuit QED experimental setup. I thank Peter Spring, who has been a great buddy inside and outside the lab. You made my PhD life entertaining and fulfilling. Thank you for your friendship and support. I am also grateful to Dr. Brian Vlastakis, who encouraged me to advance my ideas and advised me on the details of the experiment.

He taught me how to become an independent and confident experimentalist. To my lab mates, Riccardo, Matthias, Giulio, James, Shuxiang, Simone, Giovanna, Martina, Boris, Salha, Kitti, Mustafa and Vivek, I appreciate all the discussions and excellent feedback that polished my research.

I would like to extend my sincere thanks to Suguru Endo, Martin Nicolle, and Shinichi Sunami for their stimulating physics conversations in our weekly journal club. They helped me develop a solid background in quantum control and measurement theories. I also thank Gaurav Bhole for his cooperation on optimal control and spin-echo sequences. You have taught me a lot of useful NMR techniques through our discussions.

Yuki Haba was my inspiration for pursuing a PhD abroad. I am deeply grateful for his constant support and encouragement since we made this decision together.

Outside the lab, I thank Oxford University Association Football Club and Micky Lewis for giving me an amazing opportunity to play football at a high level with the Blues. This was one of my football career's most rewarding and enjoyable experiences and enriched my Oxford journey immensely.

Last but not least, I thank my family for their love, understanding and encouragement during these challenging times. Kanako, thank you for your invaluable contribution to the final stage of my PhD. You were always there to support and cheer me up. Hideko and Nobuhiro, you have always been there for me since I was a child. I appreciate you for encouraging me to pursue my dreams and goals throughout my life.

Contents

Chapter 1

Introduction

1.1 Quantum computing

Quantum mechanics is one of the most successful subfields in science. Not only does it serve as the foundation of modern physics, but it also benefits every corner of cutting-edge technologies such as materials development, energy production and drug discoveries. Nevertheless, we have only scratched the surface of its full potential because the full-scale analysis of a quantum system is limited to few tens of particles restricted by the current computational capability [1].

In order to overcome the computational limit of classical computers, Richard Feynman proposed a *quantum computer*, which uses real quantum effects to simulate quantum phenomena [2]. David Deutsch extended Feynman's idea to the concept of universal quantum computation and claimed that a universal quantum computer can simulate any phenomena in the physical world that cannot be reproduced by classical Turing machines [3] . The underlying idea of these quantum computers was to engineer a controllable quantum system that simulates other quantum systems by programming the controllable degrees of freedom.

Since then, there have been numerous studies on theoretical and experimental quantum computing. Seth Lloyd supported Feynman's idea by showing that a programmable quantum computer can simulate anly local quantum systems exponentially faster than classical computers by compiling the quantum simulation with a sequence of quantum logic gates [4]. Furthermore, an exponential speed-up of the factoring algorithm [5] and a quadratic speed-up of the search algorithm [6] proved the capability of universal quantum computers beyond the quantum simulation applications.

On the experimental side, various hardware platforms have been proposed for practical quantum computing such as trapped-ions [7, 8, 9], superconducting circuits [10, 11], nuclear magnetic resonance [12, 13], photonics [14], quantum dots [15], and cold atoms [16]. Each approach has different pros and cons in terms of coherence time, processing speed and scalability, and we are still in the exploration phase of deciding the suitable physical implementation. Still, some platforms are reaching the computational limit of classical computers in specific tasks [17, 18]. For example, a 53-qubit superconducting quantum processor performed a quantum computational task in 200 seconds, with the claim it would take the most powerful supercomputer 10000 years to execute this task [17].

The ultimate goal of quantum computer engineering is to build a fault-tolerant universal quantum computer, which has an error correcting mechanism that protects the quantum information from decoherence and other quantum noise. In theory, quantum error correction enables a quantum computer to operate indefinitely, which opens the door to implementing the above-mentioned quantum algorithms that will probably require much longer operation time than the lifetime of each qubit. Proof-of-principle experiments of quantum error correction have been implemented in various error correcting codes [19, 20], but it may still take decades before fault-tolerant quantum computers can solve hard problems [21]. Typical quantum error correcting codes require many physical qubits to make a logical qubit; for example, the current superconducting circuit architecture will need millions of qubits to implement a Shor's algorithm fault-tolerantly [22]. In that sense, we are only at the beginning of developing useful and reliable quantum computers, and we still need more breakthroughs in hardware and algorithms in the years to come.

1.2 Circuit model quantum computation

At the present time, the majority of quantum computing theorists and experimentalists work together to realise the *circuit model* of quantum computation. In the circuit model, quantum algorithms are implemented by applying a sequence of quantum logic gates to a network of qubits[1]. Although quantum gates are quantum mechanical, the programmability of the circuit model resembles the algorithm implementation on digital computers, which allows quantum computing theorists to evaluate the quantum computational complexity. In theory, any quantum algorithm can be decomposed to the *universal gate set* that typically consists of local control and two-body interactions in some physical form. Therefore, experimentalists aim to engineer the universal gate set using available physical resources they have. For the past few decades, the circuit model provided the quantum computing community with a common language so that theorists and experimentalists can pursue the same objectives.

However, the idealism of the circuit model gives strong constraints on engineering the quantum hardware. To meet the specification of a specific quantum gate, one has to engineer a quantum dynamics that realises the exact matrix elements of the desired unitary operation. Although the artificial quantum gate is far from the natural

---

[1] Mathematically, quantum gates are unitary matrices acting on local qubits and a quantum algorithm can be interpreted as a matrix product of many matrices acting on a large qubits' state that are intractable to classical computers.

quantum dynamics, any deviation from the target operation is counted as errors in the circuit model regardless of whether the deviated evolution is coherent or incoherent. For instance, quantum algorithms assume two-qubit gates to be turned on and off at will, so the ability to tune the coupling strength between qubits is crucial in reducing errors in the circuit model implementation. In the case of superconducting circuits, the always-on native couplings between qubits are regarded as error sources because they cannot be turned off on demand. Instead, there have been a number of proposals to generate interactions with high on/off ratio to make the system of superconducting qubits resemble the circuit model as closely as possible For example, the high on/off ratio can be achieved by incorporating tunability into circuit elements [23, 24] or applying external control fields with specific resonance conditions [25, 26]. However, these approaches require additional engineering complexities, such as crowding of circuit elements in a quantum processor or relentless calibration routine to realise the specific target unitary operation. These complexities increase as we add more qubits, and it is a daunting task to scale the same approach to millions of qubits.

1.3 Alternative approaches

Although the circuit model has served as an interface between theoretical and experimental quantum computing, we are not restricted to this model. The experimental constraints can be loosened if we could shift the common ground to the hardware side, at the cost of additional efforts on the algorithm development. This is reasonable in the current situation, because the bottleneck of the quantum computer development is in the experimental side. In the end, it is a matter of balancing the trade-off between difficulties in the hardware and the software development, and we should choose a quantum computing architecture that achieves a good balance between the hardware and the software constraints.

1.3.1 Hardware-efficient gates

One approach is to use hardware-efficient gates [27]. The hardware-efficient gate uses the same physical resource as a typical two-qubit gate, but does not specify exact unitary operation, which saves the cost of precise calibration[2]. The hardware-efficient gate acts as an analogue operation compared to the digital approach taken in the circuit model, which makes it easier to implement on the hardware, but increases the difficulty of compiling quantum algorithms. Still, since a universal quantum computation can be implemented by any two-qubit interaction and local control [29], in principle, hardware-efficient gates are sufficient to implement any quantum algorithms if there is a systematic way to compile quantum algorithms. Although it is impossible to compile quantum algorithms using unpredictable two-qubit interactions by hand, we can use them with help from a classical computer.

The first application of the hardware-efficient gate was applied to a quantum simulation using a quantum-classical hybrid algorithm called the Variational Quantum Eigensolver (VQE) [27]. The VQE is an optimisation algorithm designed to run a useful quantum algorithm on qubits with limited lifetime. It uses a quantum computer to store a trial wave function (=cost function) of an optimisation problem and uses a classical optimisation subroutine to find the solution[3]. Hardware-efficient gates are suitable for the VQE algorithms because the detail of the quantum evolution is not crucial as long as the quantum processor finds the optimum [30]. The hardware-efficient gate approach has been used successfully to find the ground state energies of

---

[2] Here, we assume the hardware-efficient gate as a physical entanglement generator that does not care the details of the evolution, and leaves unexpected terms in the operation [28]

[3] With the help of a classical subroutine, the hybrid algorithm benefits from avoiding the phase estimation algorithm which requires long and coherent gates for its accurate implementation. However, we note that the phase estimation algorithm gives a better scaling in terms of precision than the quantum-classical hybrid algorithm [30].

small-scale chemical compounds and a spin chain using the hardware-efficient gates originating from the cross-resonance interaction in superconducting circuits [27].

However, the scalability of using unstructured hardware-efficient gates has been questioned over the past years. There has been a concern about the barren plateau [31, 32], where gradients of the cost function used for the gradient-based quantum-classical algorithms become nearly zero over vast areas of the parameters space. Such barren plateaus are known to make random states produced by the hardware-efficient trial wave function hard to find solutions as they scale up. To avoid the barren plateau, they have proposed to include the structure provided by the original optimisation problem in the trial wave function, which is difficult for hardware-efficient entanglers that do not specify the interaction type. Moreover, ultimately, non-programmable two-qubit interactions are not suitable for compiling large-scale quantum algorithms such as Shor's algorithm and Grover's algorithm. Following these developments, a natural question arises: Is there a quantum computing architecture that achieves hardware-efficiency and programmability at the same time? This thesis aims to provide a solution to this question.

1.3.2 Programmable hardware-efficient gates

The compilation problem of hardware-efficient gates gets much simpler if we restrict the interaction type. While the hardware-efficient approach in [27] considered a general two-qubit interaction, which includes multiple non-commuting two-qubit terms, we can consider a more simple interaction such as Ising interaction. Since the Ising interaction can be obtained natively in various hardware platforms, we consider it as a hardware-efficient operation. With always-on Ising interactions across the qubits lattice, free evolution provides a universal quantum computation when combined with single-qubit gates, but the simple application of the simultaneous native interaction is not a convenient one as it corresponds to a complex pattern of evolutions.

To this end, the nuclear magnetic resonance (NMR) technique can be applied, where spin echoes [33] are used to replace the native Hamiltonian with a more convenient average Hamiltonian, in which the size of interactions are rescaled to achieve desired operation [34, 35, 36, 37]. In this paradigm, two-qubit operations are generated by the native Ising interaction and the desired operations are programmed by timings of spin-echo pulses, which manages both hardware-efficiency and programmability. In small scale simulations of the novel operating strategy, it has been shown that practical quantum algorithms such as quantum simulation and quantum Fourier transform perform better than the traditional circuit model compilation [34, 37]. However, their compiling method of rescaling the always-on Ising Hamiltonian was applicable to only six qubits or less, and the scalability of the protocol was not proven completely.

Our works in Refs. [35, 36] focused on the scalability of the spin-echo based compilation scheme, demonstrating algorithms that design Hamiltonian rescaling spin-echo sequences with nearly the shortest possible total time, and showing that the protocol is applicable to 150 qubits for all-to-all coupled system and billions of qubits for the nearest-neighbour coupled system. These works open up the possibility of programming large-scale quantum algorithms using the static Ising interaction in practical hardware platforms.

1.4 Quantum computing using native interaction

In general, the spin-echo-based approach does not assume how the interactions are generated, so the protocol can be implemented either by native Ising interaction or the pulsed interaction as long as their physical Hamiltonians are well-defined[4]. In the

---

[4] Specifically, the total system Hamiltonian has to commute with itself.

work described in this thesis, we chose to work with the native Ising interaction in superconducting circuits for several practical reasons. Firstly, the native interaction does not use active microwave pulses for the entanglement generation, which helps to reduce the heat load on the quantum computing system. Secondly, the native interaction is already present in the superconducting circuit, which does not require additional circuit elements or careful signal calibration of two-qubit operations. We will look into these features closely in the following subsection.

1.4.1 Power consumption in quantum computers

Current quantum processors are operated by a sequence of quantum gates in the form of electromagnetic pulses going through coaxial cables inside the dilution refrigerator. Due to a limited qubit lifetime, the current processing strategy aims to process the information as fast as possible to minimise incoherent errors. In this paradigm, quantum processors are driven restlessly by fast gates with hardware compilation efficient in time, which leads to a high duty cycle. However, the scalability of this approach might soon be limited by the power consumption of the cryogenic system and signal generators that scale with the number of qubits. Each pulse adds an active heat load on the system and the control line brings the room-temperature thermal noise to the system that results in a passive heat load. Although the heat generated by each pulse is very small, power consumption of the quantum computing system will be dominated by the cooling power that takes away the total heat that increases with the number of qubits [38],

$$P_{\mathrm{load}} = P_{\mathrm{pass}} + P_{\mathrm{act}} \times D, \tag{1.1}$$

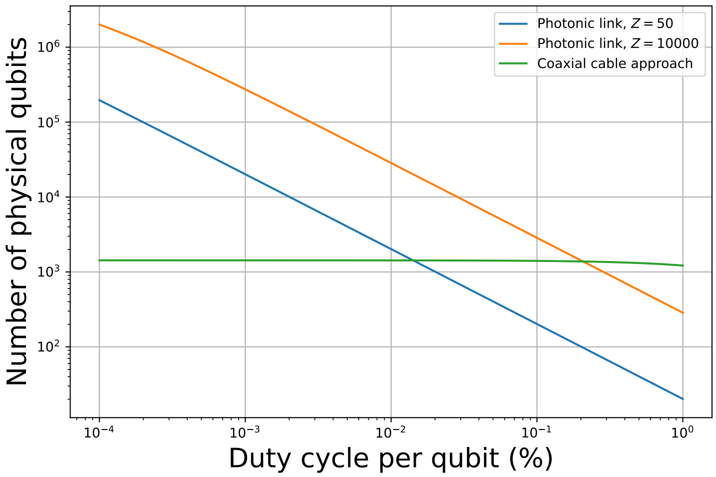

Figure 1.1: Number of qubits available for different kinds of signal input wiring. Adopted from [38].

where N is the number of qubits, $P_{\text{pass,act}}$ is the heat load of the passive and the active load per qubit, and D is the duty cycle of quantum operations. Suppose the cooling power P_{cool} is limited, the number of available qubits is bounded by $N_{\text{limit}} = P_{\text{cool}}/P_{\text{load}}$, so we can only increase the number of qubits by increasing the cooling power of the refrigeration system or decreasing the duty cycle, which counteracts with the restless operation using active gates. A recent study considering a controlling strategy using flux and microwave pulses estimated that the current cryogenic systems can hold up to only $N_{\text{limit}} = 360$ qubits due to the limitation set by the heat load [39]. The number of available qubits can be increased incrementally by improving the cooling power of the cryogenic system, but we will soon need a large technological leap to reach millions of qubits needed for fault-tolerant quantum computation [22]. Although the current trend in the superconducting quantum computing field treats the heating problem as a technical challenge in the cryogenic system and signal wirings, we consider it an issue that could be improved in the processor domain by changing the operating strategy.

1.4.2 Native interaction in superconducting circuits

Instead of applying active entangling gates to quantum processors, we can utilise native interaction naturally present in superconducting circuits for quantum entanglement generation. In a typical superconducting circuit, qubits are linked by electric circuits, producing unavoidable quantum interaction between qubits. These naturally occurring couplings are often called residual couplings because they can not be turned off, producing systematic errors. However, the entanglement generation by the residual coupling does not require any external drives, which is desirable to reduce the duty cycle during quantum computing operation significantly. In a sense, the native interaction acts as an on-chip entanglement generator which saves additional circuits, external signal generators, excessive signal flow and power consumption.

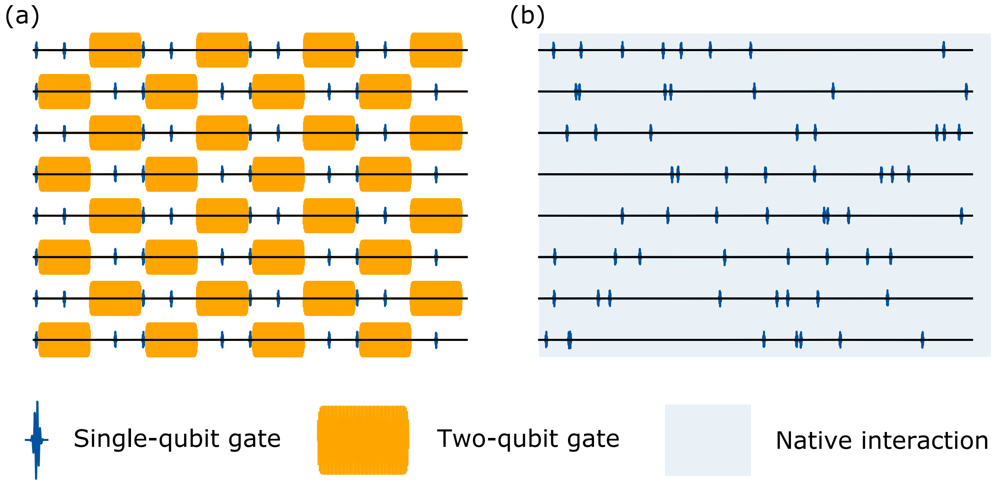

Figure 1.2: Pulse sequence of many-qubit operation in two control strategies. (a) Gate-based approach using active single-qubit and two-qubit gates to compile quantum algorithms on the hardware. (b) Hardware compilation by the native-interaction. The shaded blue area describes the always-on background interaction in the system that does not require active pulses to generate entanglement. Timings of spin-echo pulses determine phases acquired by Ising couplings, which can be used as a subroutine for various quantum algorithms. The reduction of the duty cycle can be calculated by comparing the area inside the envelopes of the active pulses in each case.

As we discussed in the previous section, in principle, the universal quantum computation can be performed using any interaction and local unitary operations [29], so we can implement any quantum algorithms using the residual coupling and single-qubit control on each qubit. In addition, the Ising interaction [40] can be directly implemented to subroutines in many useful quantum algorithms such as the quantum Fourier transform [37], the quantum phase estimation, the surface code error syndrome [22, 41], the quantum approximate optimisation algorithm [42] and the variational quantum eigensolver [43].

Since the native interaction in superconducting circuits is the Ising-type interaction, our goal is to compile quantum algorithms using the native interaction and spin-echo sequences. Specifically, our scheme compiles quantum algorithms by a sequence of active single-qubit gates such as spin-echo and basis transformation, and the free-evolution of the system by the residual Ising coupling. This way, the power consumption only originates from active single-qubit operations and passive heat load, and the duty cycle is reduced by replacing active two-qubit gates by the native interaction.

1.5 Outline

The main scope of this thesis is to introduce the novel quantum computing strategy using native interaction in supercondudcting circuits and discuss the practicality of the scheme by experiments and theoretical analysis.

Chapter 2 reviews the theory and the practice of superconducting circuits, using our experimental setup as an example. Chapter 3 gives the overview of the experimental calibration routine developed to efficiently tune up single qubit gates to high fidelity, for use in exploring algorithms exploiting the native interaction. This chapter serves as a foundation of the experimental methods used throughout this thesis. Chapter 4 presents the first demonstration of utilising the native interaction in a superconducting circuit for quantum algorithm application. We have implemented a variational quantum eigensolver to find the ground state energy of the H_2 molecule and applied a hardware-efficient error mitigation technique to extend the limit of the current noisy quantum processor. Chapter 5 introduces the general hardware compilation scheme using the native interaction and spin-echo sequences for large-scale quantum computation. This chapter aims to answer the question I raised in the introduction, whether the native interaction can replace the conventional pulsed approach and reduce the duty cycle of the quantum operation or not. Chapter 6 explores the limitation of our architecture by implementing experiments on strongly coupled qubits. The performance of the scheme is ultimately limited by how fast the entangling operation of the native interaction can become, and we have investigated the potential problems of having strong couplings by experiments. This chapter provides valuable information to determine the native interaction strengths in superconducting circuits and we have outlined the design criteria for future device. Lastly, Chapter 7 summarises our results and show an outlook of the future development of the scheme presented in this thesis.

Chapter 2

Quantum computing with superconducting circuits

This chapter introduces the concept of quantum computing and how it can be implemented in superconducting circuits. First, we briefly introduce the essential mathematical tools to describe quantum information processing. We then review state of the art in quantum computing using superconducting circuits and explain the circuit quantum electrodynamics (circuit QED) theory. In the second half, we show how the circuit QED theory can be transferred to real-world superconducting electric circuits and practical quantum computing system. As an example, we explain a quantum computing system built in our lab, which was developed and operated for the main experiments in later chapters.

2.1 Theory

In this section, we explain how a superconducting quantum computer works in theory. First, we begin with the quantum computing basics to introduce the mathematical model of a quantum computer, which is crucial in understanding quantum algorithms and quantum information theory. We then review the development of quantum computers on the hardware side, summarising various approaches to realise a quantum computer. Specifically, we introduce circuit QED [44] to explain the characteristics and the behaviour of superconducting circuits. As a whole, this section aims to link the theory of quantum computing with the physics of superconducting electrical circuits.

2.1.1 Quantum computing basics

To perform a logic operation on a computer, we need a medium to store information. Just like classical computers describe information by *bit*s, quantum computers represent quantum information by *qubit*s [45].

Physically, a qubit is a quantum system that can take two states. The two-state system is the simplest form of a quantum system that can exist, making it the most primitive quantum information element. Following the notation in quantum mechanics, we represent a qubit state by a state vector in a Hilbert space $\mathscr{H}^2$. Particularly, we define two states as $|0\rangle = \left(\begin{smallmatrix}1\\0\end{smallmatrix}\right)$, $|1\rangle = \left(\begin{smallmatrix}0\\1\end{smallmatrix}\right)$ and their superposition state as,

$$|\psi\rangle = c_0 |0\rangle + c_1 |1\rangle \tag{2.1}$$

where c_0 and c_1 are complex amplitudes whose square of the absolute values dictate the system's probability to be in either of the eigenstates. The ability to control the complex amplitude and access superposition states are some of the features that distinguish qubits from classical bits.

The physics of the two-state system is well-formulated in the study of a spin-1/2 particle, so we exploit their mathematical tools to discuss a qubit's properties. Bloch sphere picture gives us insights into qubit's dynamics, which is useful when analysing

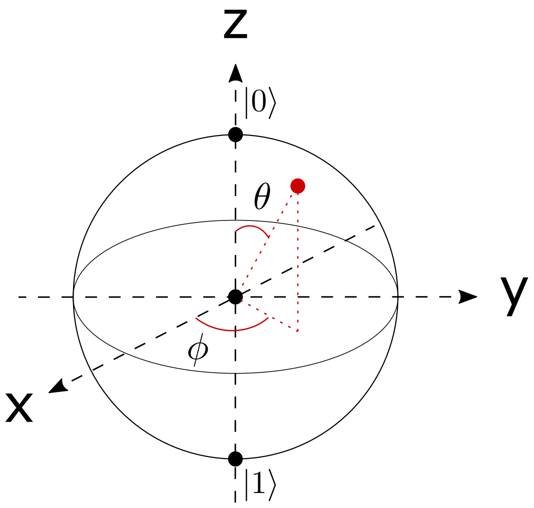

Figure 2.1: Bloch sphere picture of a quantum state. The red point on the surface of the Bloch sphere represents a state vector $|\psi\rangle = \cos\frac{\theta}{2}|0\rangle + e^{-i\phi}\sin\frac{\theta}{2}|1\rangle$.

single-qubit.

Since $|c_0|^2$ and $|c_1|^2$ are probabilities, they satisfy the relation $|c_0|^2 + |c_1|^2 = 1$, so we can map the complex amplitudes to $c_0 = \cos\frac{\theta}{2}$ and $c_1 = e^{-i\phi}\sin\frac{\theta}{2}$, where θ and ϕ are the polar coordinate in real space. The state vector $|\psi\rangle \in \mathscr{H}^2$ can be mapped to a vector $\vec{v} \in \mathbb{R}^3$, called the Bloch vector, directing a point on the unit sphere, called the Bloch sphere. The Bloch vector $\vec{v} = (x, y, z)$ of a state vector $|\psi\rangle = \cos\frac{\theta}{2}|0\rangle + e^{-i\phi}\sin\frac{\theta}{2}|1\rangle$ is represented as a projection to each axis of the Bloch sphere,

$$\begin{aligned} x &= \langle\psi|\hat{X}|\psi\rangle = \cos\phi\sin\theta, \\ y &= \langle\psi|\hat{Y}|\psi\rangle = \sin\phi\sin\theta, \\ z &= \langle\psi|\hat{Z}|\psi\rangle = \cos\theta, \end{aligned} \tag{2.2}$$

using Pauli operators,

$$\hat{X} = \begin{pmatrix} 0 & 1 \\ 1 & 0 \end{pmatrix}, \ \hat{Y} \ = \ \begin{pmatrix} 0 & -i \\ i & 0 \end{pmatrix}, \ \hat{Z} = \begin{pmatrix} 1 & 0 \\ 0 & -1 \end{pmatrix}, \ \hat{I} = \begin{pmatrix} 1 & 0 \\ 0 & 1 \end{pmatrix}. \tag{2.3}$$

In principle, we can describe any single-qubit evolution by the Bloch vector's motion on the Bloch sphere.

Qubit dynamics and operation

In general, a quantum system's dynamics is determined by the Schrodinger equation and the system Hamiltonian $\hat{\mathcal{H}}$,

$$i\hbar\frac{\partial}{\partial t}\left|\psi(t)\right\rangle \ = \ \hat{\mathcal{H}}\left|\psi(t)\right\rangle. \tag{2.4}$$

Suppose the system Hamiltonian is defined by $\hat{\mathcal{H}}/\hbar = -\frac{\omega}{2}\hat{Z}$, and the initial state was $\left|\psi(0)\right\rangle = \begin{pmatrix} \cos\frac{\theta}{2} \\ e^{-i\phi}\sin\frac{\theta}{2} \end{pmatrix}$, the state evolves as

$$\left|\psi(t)\right\rangle = e^{\frac{i\omega t}{2}\hat{Z}}\left|\psi(0)\right\rangle = e^{\frac{i\omega t}{2}}\begin{pmatrix} \cos\frac{\theta}{2} \\ e^{-i(\phi+\omega t)}\sin\frac{\theta}{2} \end{pmatrix}. \tag{2.5}$$

This operation is equivalent to rotating the Bloch vector, Eq. (2.2) around the z-axis of the Bloch sphere by a rotation matrix in real space,

$$\begin{pmatrix} \cos(\phi+\omega t)\sin\theta \\ \sin(\phi+\omega t)\sin\theta \\ \cos\theta \end{pmatrix} = \begin{pmatrix} \cos\omega t & -\sin\omega t & 0 \\ \sin\omega t & \cos\omega t & 0 \\ 0 & 0 & 1 \end{pmatrix}\begin{pmatrix} \cos\phi\sin\theta \\ \sin\phi\sin\theta \\ \cos\theta \end{pmatrix}. \tag{2.6}$$

Here we ignored the global phase since it doesn't affect the nature of the operation and the superposition state. Similarly, the Bloch vector's rotation around each axis can be described as the exponential of Pauli matrices, so-called rotation operators acting on $|\psi\rangle \in \mathscr{H}^2$.

$$\hat{R}_x(\theta) = e^{-\frac{i\theta\hat{X}}{2}} = \cos\frac{\theta}{2}\hat{I} - i\sin\frac{\theta}{2}\hat{X}, \tag{2.7}$$

$$\hat{R}_y(\theta) = e^{-\frac{i\theta\hat{Y}}{2}} = \cos\frac{\theta}{2}\hat{I} - i\sin\frac{\theta}{2}\hat{Y}, \tag{2.8}$$

$$\hat{R}_z(\theta) = e^{-\frac{i\theta\hat{Z}}{2}} = \cos\frac{\theta}{2}\hat{I} - i\sin\frac{\theta}{2}\hat{Z}. \tag{2.9}$$

Just like we need rotations around two axes to move a point to any other points on the unit sphere's surface, two rotation operators suffice for the arbitrary control of a single qubit. In general, any operation on a qubit can be fully characterised by a single-qubit Hamiltonian defined on the Pauli-basis and we will use this property to characterise single-qubit operation experimentally.

Similarly, we can describe two-qubit dynamics in the Pauli-basis and the interaction is characterised by the tensor product of Pauli operators. For example, $\hat{\mathcal{H}}/\hbar = \frac{\zeta}{4}\hat{Z} \otimes \hat{Z}$ generates interaction between two qubits, which enables an entanglement of a two-qubit state $|\psi\rangle_1 \otimes |\psi\rangle_2$. We can obtain the Bloch vector using the same method as the single-qubit case. However, for a two-qubit system, there are $4 \times 4 = 16$ Pauli operators, so the two-qubit state $|\psi\rangle_1 \otimes |\psi\rangle_2$ is mapped to a Bloch vector in 15-dimensional space. We have omitted one degree of freedom because the square sum of the complex amplitudes of the two-qubit state has to be 1. Experimentally, the act of projecting the state vector to each Pauli-basis is called a quantum state tomography [46], equivalent to plotting a point on the Bloch sphere for a one-qubit case. It helps us understand the complex dynamics of a two-qubit system, so we will revisit the two-qubit Bloch vector and the quantum state tomography in later chapters.

Relation to later chapters

In principle, universal quantum computation can be implemented using any entangling interaction and arbitrary one-qubit operations mentioned in this section [29]. Therefore, by combining one-qubit operation and native two-qubit interaction, we can run any quantum algorithms if we can efficiently compile algorithms to physical hardware with native interaction.

The central theme of this thesis is to introduce a novel hardware compilation scheme on quantum processors with native two-qubit interaction. In the following sections, we will explain how the native two-qubit interaction arises in superconducting circuits and how to achieve universal one-qubit control on the Bloch sphere. We then give a proof-of-principle experiment of a quantum algorithm implementation by the native gate in Chapter 4 and introduce the theoretical development of the hardware compilation scheme in Chapter 5.

2.1.2 Hardware development of quantum computers

In the previous subsection, we have introduced a theoretical background on quantum information processing, assuming that a qubit is a quantum two-level system. Practically, there are various hardware platforms to realise the two-level system such as trapped-ions [7, 8, 9], superconducting circuits [10, 11] and nuclear magnetic resonance [12, 13].

For many years, the cavity quantum electrodynamics (cavity QED) has provided a theoretical framework to describe the quantum information processing of each hardware platform, explaining the interplay between the qubits' coherent dynamics and decoherence, essential to understanding the practicalities of quantum information processing in each platform [47]. With tools that enable the quantitative analysis of decoherence, experiments on the light-matter interaction have hugely developed, and it helped understand how the environment plays a role in coherent quantum dynamics [48].

Following the development of the cavity QED in natural systems, the same approach has been explored in solid state systems. In 1999 an artificial two-level system was realised in a single-cooper-pair box [10], and the field of superconducting qubit has developed dramatically ever since. In 2004 the strong coupling between a superconducting qubit and an on-chip cavity was realised [11] and the field of the circuit quantum electrodynamics (circuit QED) emerged [44]. The circuit QED made the theoretical and experimental toolsets in the cavity QED transferrable to superconducting circuit experiments, which accelerated the development of this field. Most significantly, cavity QED experiments in various parameter regimes could be designed by specifying the circuit dimensions of superconducting circuits, deepening the understanding of the cavity QED, including properties in unconventional parameter regimes [49, 50].

Along with demonstrating the proof-of-principle experiments, the circuit QED guided designing the optimal superconducting quantum circuit for quantum computing applications. The circuit QED played a crucial role in inventing the transmon qubit [51], which is the standard qubit design in the current quantum computing application. Through circuit QED analysis of the dephasing and coupling mechanisms in superconducting circuits, they have provided the design criteria for long coherence qubits while maintaining high fidelity control and readout desirable for quantum computing. As of 2021, the coherence time of superconducting qubits has been extended 10^5 times after many generations of qubit designs since 1999 [52].

Building on top of the device developments, the superconducting circuit community has also been exploring ways to improve multi-qubit operation. In particular, various coupling schemes have been proposed to implement fast two-qubit gates to apply as many gates in a limited qubit lifetime as possible, which led to a high-fidelity many-qubits operation in 20-50 qubits scale [17, 53]. However, further efforts are needed to scale the system to more qubits required for large-scale quantum computation. Conventional multi-qubit operation schemes need tailored calibration routines for external control fields with specific resonance condition [25] or additional circuits for tunability [23, 24], which add more engineering complexity than operating a simple superconducting circuit. As the number of qubits increase in a quantum processor, these engineering difficulties in fabricating and controlling the device add up.

To avoid the complexity of superconducting circuit layout and operation strategy in a large scale, we have explored ways to simplify superconducting circuit design and operation for future scalability. In our *coaxmon* architecture [54], control and readout wirings were taken out of the qubit and the resonator plane, which reduced the circuit complexity of the superconducting circuit. The simplicity in the circuit design reduces the fabrication complexity and makes it easier to investigate noise channels.

This thesis aims to simplify multi-qubit operation in many-qubits superconducting circuits including the coaxmon architecture. In our novel controlling strategy, the multi-qubit operation is generated by native interaction in superconducting circuits, which does not depend too much on active operations. The following subsections review the circuit QED theory, which leads to explaining our coaxmon architecture in the next section and derives the native interaction in superconducting circuits crucial for the quantum computing strategy presented in this thesis.

2.1.3 Circuit quantum electrodynamics (circuit QED)

Basic elements of superconducting circuits

In an electric circuit, a harmonic mode can be engineered using a single inductor and capacitor, connected in parallel (see Fig. 2.2). The LC circuit acts as a resonator that stores photons whose energy levels are determined by the circuit's resonant frequency $\omega = \frac{1}{\sqrt{LC}}$,

$$\mathcal{H}_R = \frac{q^2}{2C} + \frac{\phi^2}{2L}, \tag{2.10}$$

where q is the charge on the capacitor and ϕ is the flux passing through the inductor. Since the Hamiltonian satisfies the following relation,

$$\begin{aligned} \frac{\partial \mathcal{H}_R}{\partial q} &= \frac{q}{C} = -L\frac{\partial I}{\partial t} = -\dot{\phi}, && (2.11) \\ \frac{\partial \mathcal{H}_R}{\partial \phi} &= \frac{\phi}{L} = I = \dot{q}, && (2.12) \end{aligned}$$

we can regard q and ϕ as the system's canonical variables, and we can apply the canonical quantisation. By treating $\hat{\phi}$ and $\hat{q}$ as quantum variables, we can rewrite the Hamiltonian as $\hat{\mathcal{H}}_R = \frac{\hat{q}^2}{2C} + \frac{\hat{\phi}^2}{2L}$, with the commutation relation $[\hat{\phi}, \hat{q}] = i\hbar$.

Although the Hamiltonian helps us describing the quantum behaviour of charge and flux degrees of freedom, these variables are not suitable in the cavity QED formalism where physical systems are described in the photon-number basis. To describe the system in the photon-number basis, we apply the second quantisation to the system Hamiltonian by replacing the charge and the flux variables by,

$$\begin{aligned} \hat{\phi} &= \sqrt{\frac{\hbar Z_C}{2}}(\hat{a}^\dagger + \hat{a}), && (2.13) \\ \hat{q} &= i\sqrt{\frac{\hbar}{2Z_C}}(\hat{a}^\dagger - \hat{a}), && (2.14) \end{aligned}$$

where $\hat{a}$ and $\hat{a}^\dagger$ are annihilation and creation operators, with $Z_C = \sqrt{\frac{L}{C}}$ being the characteristic impedance of the resonator. Now, the Hamiltonian is,

$$\hat{\mathcal{H}}_R = \hbar\omega_r\Big(\hat{a}^\dagger\hat{a} + \frac{1}{2}\Big). \tag{2.15}$$

Unless the system is completely decoupled from the environment, the LC resonator loses its photons at a rate of κ. We can characterise how much the system is coupled to the environment by the quality factor $Q = \frac{\omega_r}{\kappa}$, which determines essential device properties, such as the readout efficiency and the resonator-induced dephasing of a qubit [55].

Although we can observe an LC circuit in the quantum mechanical ground state, the equally-spaced energy levels don't allow one to access well-defined two energy levels to address a qubit. To create a qubit, we need to introduce anharmonicity to the circuit, and the Josephson Junction plays the role. The Josephson Junction is a non-dissipative circuit component having an insulating barrier between two superconducting electrodes that pass through superconducting current. The superconducting current across the Josephson Junction has the property of $I = I_0 \sin\theta$, where θ is the phase difference between the two superconducting electrodes, which is related to the flux stored across the junction ϕ by $\theta = \frac{2\pi\phi}{\Phi_0}$, with $\Phi_0 = \frac{h}{2e}$ the flux quantum. Because of this relation, the Josephson Junction behaves as a non-linear inductance that depends on the flux,

$$L(\phi) = \Big(\frac{\partial I}{\partial \phi}\Big)^{-1} = \frac{\Phi_0}{2\pi I_0 \cos\frac{2\pi\phi}{\Phi_0}}, \tag{2.16}$$

which adds the anharmonicity to the circuit when we replace the LC resonator's inductance with the Josephson Junction (see Fig. 2.2). We can also derive the energy around the non-linear inductance by $E = \int V(t)I(t)dt = \int(\frac{d\phi}{dt})I(t)dt =$

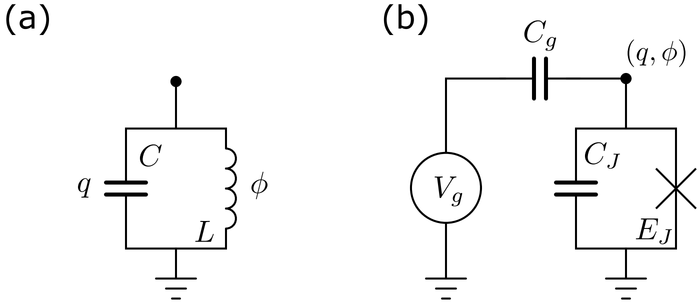

Figure 2.2: Circuit diagrams of basic superconducting circuit elements. (a) An LC resonator. (b) A superconducting qubit consisting of a capacitance and a Josephson junction. Circuits' dynamics can be investigated by solving the equations of motion of the charge q and the flux ϕ defined on the black nodes indicated in the circuits.

$-E_J \sin\left(\frac{2\pi\phi}{\Phi_0}\right)$, where $E_J = \frac{\Phi_0 I_0}{2\pi}$ is the Josephson energy. Assuming a capacitance coupling to an external gate voltage $V_g = \frac{q_g}{C_g}$ as shown in the Fig. 2.2, the total Hamiltonian of a superconducting qubit can be derived similarly to the LC circuit as follows,

$$\hat{\mathcal{H}} = \frac{(\hat{q} - q_g)^2}{2C_\Sigma} - E_J \cos\left(\frac{2\pi\hat{\phi}}{\Phi_0}\right) \tag{2.17}$$

$$= 4E_C(\hat{n} - n_g)^2 - E_J \cos\left(\hat{\theta}\right), \tag{2.18}$$

where $C_\Sigma = C_g + C_J$ is the total capacitance to the ground [51]. In the second line, we have defined the charge and the phase bases ensuring the commutation relation $[\hat{\theta}, \hat{n}] = i$, where $\hat{\theta} = \frac{2\pi\hat{\phi}}{\Phi_0}$, $\hat{n} = \frac{\hat{q}}{2e}$, $n_g = \frac{q_g}{2e}$ and the charging energy $E_C = \frac{e^2}{2C_\Sigma}$. The second term in the Hamiltonian introduces the anharmonicity to the energy levels, and we can assign the two lowest levels as a qubit.

The non-linearity of the energy levels depend heavily on the ratio $\frac{E_J}{E_C}$ [51], which is a crucial parameter when we design superconducting qubits. When $\frac{E_J}{E_C}$ is small, the qubit transition frequency is not robust to the charge fluctuation, making it prone to decoherence. On the other hand, the anharmonicity of the energy levels decreases as we increase $\frac{E_J}{E_C}$, which adds difficulty when we control the state of a qubit. Therefore, there is a trade-off between large and small $\frac{E_J}{E_C}$, and we will explore how the essential properties of superconducting qubits such as charge dispersion and anharmonicity scale with $\frac{E_J}{E_C}$ in the following.

The charge dispersion of the energy levels can be obtained by diagonalising the qubit Hamiltonian (2.18) in the charge basis (see Fig. 2.3). As we can see from the figure, the charge dispersion decreases with increasing $\frac{E_J}{E_C}$, and [51] showed the exponential decrease of the charge dispersion with $\sqrt{\frac{E_J}{E_C}}$.

Because of this, we typically aim $E_J/E_C > 50$, and in this regime, we can approximate the Hamiltonian as follows [56],

$$\hat{\mathcal{H}}_Q \approx 4E_C\hat{n}^2 + \frac{E_J}{2}\hat{\theta}^2 - \frac{E_J}{4}\hat{\theta}^4. \tag{2.19}$$

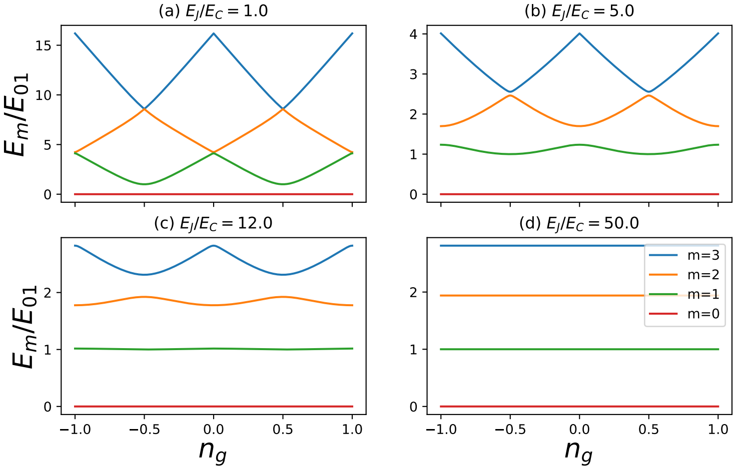

Figure 2.3: Charge dispersion of the transmon energy levels. The energy levels are obtained by numerically diagonalising the transmon Hamiltonian in the charge basis, and the mth energy level E_m is normalised by the energy difference between the ground and the first excited states E_{01}. We can see that the energy levels become more robust to the offset charge n_g fluctuation as we increase E_J/E_C.

Changing the basis to the number basis using the second quantisation,

$$\hat{\theta} = \left(\frac{E_C}{2E_J}\right)^{\frac{1}{4}}(\hat{b}^\dagger + \hat{b}), \tag{2.20}$$

$$\hat{n} = \frac{i}{2}\left(\frac{E_J}{2E_C}\right)^{\frac{1}{4}}(\hat{b}^\dagger - \hat{b}), \tag{2.21}$$

we arrive at an approximated Hamiltonian,

$$\hat{\mathcal{H}}_Q \approx \sqrt{8E_J E_C}\hat{b}^\dagger\hat{b} - \frac{E_C}{12}(\hat{b}^\dagger + \hat{b})^4 \tag{2.22}$$

$$\approx \hbar\omega_q\hat{b}^\dagger\hat{b} + \frac{\alpha}{2}\hat{b}^\dagger\hat{b}^\dagger\hat{b}\hat{b}, \tag{2.23}$$

where $E_{01} = \hbar\omega_q \approx \sqrt{8E_J E_C} - E_C$ is the resonant frequency of the qubit and $\alpha \approx -E_c$ is the anharmonicity of the qubit energy levels. In the second line, we have applied the rotating wave approximation to ignore the fast oscillating terms. In contrast to the exponentially decreasing charge dispersion with $\frac{E_J}{E_C}$, the anharmonicity $\frac{E_C}{E_{01}} \approx (\frac{8E_J}{E_C})^{-\frac{1}{2}}$ decreases with a weak power law to $\frac{E_J}{E_C}$ [51]. Therefore, the $\frac{E_J}{E_C}$ ratio is set around $50 \sim 100$ so that the charge dispersion does not limit coherence time of the qubit and the anharmonicity is kept large to suppress the leakage to higher levels. Qubits designed around this regime are called *transmons* and we set our qubit's $\frac{E_J}{E_C}$ in this range. Note that, we will use *transmon* and *qubit* interchangeably in the following sections.

To obtain a more accurate value of E_J and E_C from measured qubit frequency $\omega_q = E_{01}/\hbar$ and anharmonicity $\hbar\alpha = 2E_{01} - E_{02}$, we can approximate E_J and E_C

using the fifth-order perturbation theory presented in [57] as follows,

$$\begin{aligned} \hbar\omega_q &\approx \sqrt{8E_JE_C} - E_C\Big(1 + \frac{1}{2^2}\xi + \frac{21}{2^7}\xi^2 + \frac{19}{2^7}\xi^3 + \frac{5319}{2^{15}}\xi^4\Big), \quad (2.24) \\ \hbar\alpha &\approx -E_C\Big(1 + \frac{9}{2^4}\xi + \frac{81}{2^7}\xi^2 + \frac{3645}{2^{12}}\xi^3 + \frac{46899}{2^{15}}\xi^4\Big), \quad (2.25) \\ \xi &= \sqrt{\frac{2E_C}{E_J}}. \end{aligned}$$

Coupling superconducting circuits

We have discussed how the main ingredients of the cavity QED experiments, an atom and a cavity, can be engineered using superconducting electrical circuits. In this section, we explain the coupling mechanism in the artificial quantum system, and we consider a capacitance connecting two superconducting circuit elements described in Fig. 2.2. At the beginning of the derivation, we do not have to specify whether the coupled circuit elements are (a) an LC resonator and a qubit or (b) two qubits. The Hamiltonian of the composite quantum circuit can be derived by applying the circuit quantisation technique, called "the method of nodes" [58]. In the method of nodes, we label each island in the circuit by number (i=1,2) to distinguish each node's charge q_i and flux ϕ_i (i=1,2) variables. Charges on the nodes can be described by a set of

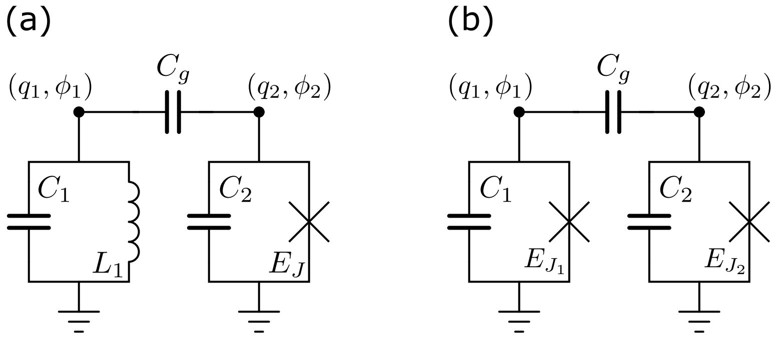

Figure 2.4: Circuit diagrams of coupled superconducting circuit elements. (a) Resonator-qubit coupling. (b) Qubit-qubit coupling.

equations of motion,

$$q_1 = C_1\dot{\phi}_1 + C_g(\dot{\phi}_1 - \dot{\phi}_2), \tag{2.26}$$

$$q_2 = C_g(\dot{\phi}_2 - \dot{\phi}_1) + C_2\dot{\phi}_2, \tag{2.27}$$

which can be expressed in a simple form $\boldsymbol{q} = \boldsymbol{C}\dot{\boldsymbol{\phi}}$, where a capacitance matrix $\mathbf{C}$ is defined by,

$$\boldsymbol{C} = \begin{pmatrix} C_g + C_1 & -C_g \\ -C_g & C_2 + C_g \end{pmatrix}. \tag{2.28}$$

Since there is no inductive coupling between node 1 and 2, we can regard flux on each node independently and it doesn't contribute to the coupling term in the Hamiltonian. Here we leave the potential energy as V and discuss the details after we specified the coupled elements. The total Hamiltonian can be described by the capacitance matrix and the potential energy,

$$\mathcal{H} = \frac{1}{2}\boldsymbol{q}^{\boldsymbol{T}}\boldsymbol{C}\boldsymbol{q} + V \tag{2.29}$$

$$= \frac{(C_2 + C_g)q_q^2 + 2C_g q_1 q_2 + (C_g + C_1)q_1^2}{2(C_1C_2 + C_2C_g + C_gC_1)} + V. \tag{2.30}$$

To investigate the coupling, we focus on a term that involves q_1q_2, which has effects from both nodes. The specifics of the coupling term depends on how we apply the second quantisation to each node, and we need to consider whether the node is connected to a transmon or an LC resonator.

Resonator-qubit coupling

In a case where a resonator is on the node 1 and a qubit is on the node 2, we substitute (2.14) and (2.21) for $\hat{q}_1 = 2e \cdot \hat{n}_1,\ \hat{\phi}_1 = \frac{\Phi_0}{2\pi} \cdot \hat{\theta}_1,\ \hat{q}_2 = 2e \cdot \hat{n}_2$ and $\hat{\phi}_2 = \frac{\Phi_0}{2\pi} \cdot \hat{\theta}_2$ to obtain the coupling term in terms of the annihilation and the creation operators,

$$\begin{aligned}
\hat{\mathcal{H}}_{\text{Coupling}} &= \frac{2C_g \hat{q}_1 \hat{q}_2}{2(C_1C_2 + C_2C_g + C_gC_1)} && (2.31)\\
&= -\frac{eC_g\sqrt{\frac{\hbar}{Z_r}}\left(\frac{E_J}{E_C}\right)^{\frac{1}{4}}}{2(C_1C_2 + C_2C_g + C_gC_1)}(\hat{a}_1^\dagger - \hat{a}_1)(\hat{b}_2^\dagger - \hat{b}_2^\dagger) && (2.32)\\
&= -\hbar g(\hat{a}_1^\dagger - \hat{a}_1)(\hat{b}_2^\dagger - \hat{b}_2^\dagger), && (2.33)
\end{aligned}$$

where $Z_r = \sqrt{\frac{L_1}{C_1}}$ is the characteristic impedance of the resonator and g is the coupling strength between a qubit and a resonator. In the limit of $C_1, C_2 \gg C_g$, we can approximate the coupling strength as,

$$g \approx \omega_r \frac{C_g}{C_2}\left(\frac{E_J}{2E_C}\right)^{\frac{1}{4}}\sqrt{\frac{\pi Z_r}{R_0}}, \tag{2.34}$$

where ω_r is the resonant frequency of the resonator, and $R_0 = \frac{h}{e^2}$ is the resistance quantum. Previously, we have seen that a large $\frac{E_J}{E_C}$ ratio makes a qubit insensitive to the charge degrees of freedom, which increases the qubit's decoherence time. However, the less sensitivity to charge means the inability to discriminate the qubit's state by directly measuring the charge degrees of freedom. This is fine because we see from (2.34) that the coupling to a resonator strengthens with increasing $\frac{E_J}{E_C}$, and we can use the resonator to probe the qubit's state. The transmon qubits use this coupling mechanism to read out the qubit state by a coupled-resonator indirectly [11].

Lastly, the energy contribution from the inductive elements can be summarised as a potential energy $V = \frac{\phi_1^2}{2L_1} - E_J\cos\left(\frac{2\pi\phi_2}{\Phi_0}\right)$. Using a similar method to deriving a resonator and a qubit Hamiltonian, we obtain the total Hamiltonian as,

$$\begin{aligned}\hat{\mathcal{H}}_{R-Q} &= \hbar\omega_r(\hat{a}_1^\dagger\hat{a}_1 + \frac{1}{2}) + \hbar\omega_q\hat{b}_2^\dagger\hat{b}_2 + \frac{\hbar\alpha}{2}\hat{b}_2^\dagger\hat{b}_2^\dagger\hat{b}_2\hat{b}_2 - \hbar g(\hat{a}_1^\dagger - \hat{a}_1)(\hat{b}_2^\dagger - \hat{b}_2^\dagger) \quad (2.35)\\ &\approx \hbar\omega_r(\hat{a}_1^\dagger\hat{a}_1 + \frac{1}{2}) + \hbar\omega_q\hat{b}_2^\dagger\hat{b}_2 + \frac{\hbar\alpha}{2}\hat{b}_2^\dagger\hat{b}_2^\dagger\hat{b}_2\hat{b}_2 + \hbar g(\hat{a}_1^\dagger\hat{b}_2 + \hat{a}_1\hat{b}_2^\dagger), \quad (2.36)\end{aligned}$$

where $\hat{a}_1^\dagger, \hat{a}_1$, and $\hat{b}_2^\dagger, \hat{b}_2$ are operators that excite or lower modes at node 1 and 2, and we have applied the rotating wave approximation in the second line.

Qubit-qubit coupling

In the case of a qubit-qubit coupling, we apply the second quantisation by substituting (2.21) to the charge and the flux variables on both nodes. The coupling Hamiltonian can be obtained as,

$$\begin{aligned}\hat{\mathcal{H}}_{\text{Coupling}} &= -\frac{e^2C_g\left(\frac{E_{J_1}}{E_{C_1}}\right)^{\frac{1}{4}}\left(\frac{E_{J_2}}{E_{C_2}}\right)^{\frac{1}{4}}}{\sqrt{2}\Big(C_1C_2 + C_2C_g + C_gC_1\Big)}(\hat{b}_1^\dagger - \hat{b}_1)(\hat{b}_2^\dagger - \hat{b}_2^\dagger) \quad (2.37)\\ &= -\hbar J(\hat{b}_1^\dagger - \hat{b}_1)(\hat{b}_2^\dagger - \hat{b}_2^\dagger), \quad (2.38)\end{aligned}$$

where we denote J as the coupling strength between two qubits. In the limit of $C_1, C_2 \gg C_g$, we can approximate the coupling strength as,

$$J \approx \frac{2C_g}{C_1C_2}\Big(\frac{E_{J_1}}{2E_{C_1}}\Big)^{\frac{1}{4}}\Big(\frac{E_{J_2}}{2E_{C_2}}\Big)^{\frac{1}{4}}\frac{\pi}{R_0}. \quad (2.39)$$

Lastly, the energy contribution from the inductive elements can be summarised as a potential energy $V = \sum_{i=1,2} -E_{J_1}\cos\Big(\frac{2\pi\phi_i}{\Phi_0}\Big)$, so the second quantised Hamiltonian can be derived as,

$$\hat{\mathcal{H}}_{Q-Q} = \sum_{i=1,2}\Big(\hbar\omega_{q_i}\hat{b}_i^\dagger\hat{b}_i + \frac{\hbar\alpha_i}{2}\hat{b}_i^\dagger\hat{b}_i^\dagger\hat{b}_i\hat{b}_i\Big) - \hbar J(\hat{b}_1^\dagger - \hat{b}_1)(\hat{b}_2^\dagger - \hat{b}_2^\dagger) \tag{2.40}$$

$$\approx \sum_{i=1,2}\Big(\hbar\omega_{q_i}\hat{b}_i^\dagger\hat{b}_i + \frac{\hbar\alpha_i}{2}\hat{b}_i^\dagger\hat{b}_i^\dagger\hat{b}_i\hat{b}_i\Big) + \hbar J(\hat{b}_1^\dagger\hat{b}_2 + \hat{b}_1\hat{b}_2^\dagger), \tag{2.41}$$

where we have ignored the fast-oscillating terms in the coupling term.

Coupling in the dispersive regime

We have seen that a quantum processor's crucial parameters, such as resonant frequencies of resonators and qubits and their coupling strength, can be engineered by specifying suitable electric circuit parameters. The circuit QED formalism enabled us to design cavity QED experiments on circuits, which opened an ample parameter space to explore circuit parameters depending on our needs.

Particularly, in the aim of building a quantum processor, we set the qubit-resonator detuning to be much larger than their coupling strength. The parameter range of $g \ll \Delta_{q-r}$ is so-called the dispersive regime, and it is advantageous for the lifetime enhancement [40, 59] and reading out the qubit's state [51]. We also set qubit-qubit detuning to be large enough so that the drive on one qubit does not excite other qubits. Typical coupling strength J is much smaller than the detuning $J \ll \Delta_{q-q}$ [60], so we can assume the qubit-qubit coupling is in the dispersive regime as well.

The dispersive coupling is the core of this thesis as we exploit it in the readout and the two-qubit operation of a quantum processor. Here, we will show how the dispersive coupling shifts the energy levels for both resonator and qubit and discuss the application of the dispersive shift in quantum information processing. Since the coupling terms of the qubit-resonator system and the qubit-qubit system have similar forms, we can approximate the Hamiltonian similarly, using the second-order perturbation theory. Regarding the general Hamiltonian $\hat{\mathcal{H}} = \hat{\mathcal{H}}_0 + \hat{V}$, where we consider $\hat{V} = \hbar g(\hat{c}_1^\dagger \hat{c}_2 + \hat{c}_1 \hat{c}_2^\dagger)$ as a perturbation to an uncoupled Hamiltonian $\hat{\mathcal{H}}_0$, we can find the first and second-order approximation as,

$$\hat{\mathcal{H}}^{(1)} = \sum_i \langle i| V |i\rangle |i\rangle \langle i| = 0, \tag{2.42}$$

$$\hat{\mathcal{H}}^{(2)} = \sum_i \sum_j \frac{\langle i|V|j\rangle \langle j|V|i\rangle}{E_i - E_j} |i\rangle \langle i|, \tag{2.43}$$

where E_i and $|i\rangle$ are the eigenenergies and the eigenvectors of the original Hamiltonian $\hat{\mathcal{H}}_0 |i\rangle = E_i |i\rangle$, and we assume the eigenenergies are non-degenerate. Here, the Hilbert space is spanned by $|i\rangle = |m, n\rangle = |m\rangle \otimes |n\rangle$, where $|m\rangle$ and $|n\rangle$ are Fock states of each modes labelled by 1 and 2. The first-order approximation vanishes in this case because the coupling term $\hat{V} = \hbar g(\hat{c}_1^\dagger \hat{c}_2 + \hat{c}_1 \hat{c}_2^\dagger)$ has no diagonal elements. Terms in the second order approximation become non-zero for nearby transitions,

$$\left\langle V'_+ \right\rangle = \langle m, n| V |m-1, n+1\rangle = \hbar g \sqrt{m}\sqrt{n+1}, \tag{2.44}$$

$$\left\langle V'_- \right\rangle = \langle m, n| V |m+1, b-1\rangle = \hbar g \sqrt{m+1}\sqrt{n}, \tag{2.45}$$

and we obtain the second-order perturbation as follows,

$$\begin{aligned} \hat{\mathcal{H}}^{(2)} &= (\hbar g)^2 \sum_{m,n} \Big(\frac{\left\langle V'_+ \right\rangle \left\langle V'_+ \right\rangle^\dagger}{E_{m,n} - E_{m-1,n+1}} + \frac{\left\langle V'_- \right\rangle \left\langle V'_- \right\rangle^\dagger}{E_{m,n} - E_{m+1,n-1}} \Big) |m, n\rangle \langle m, n| \\ &= (\hbar g)^2 \sum_{m,n} \Big(\frac{m(n+1)}{E_{m,n} - E_{m-1,n+1}} + \frac{(m+1)n}{E_{m,n} - E_{m+1,n-1}} \Big) |m, n\rangle \langle m, n| . \end{aligned} \tag{2.46}$$

Coefficients of the above Hamiltonian depend on the system's energy levels, so we will consider the following cases separately, (1) resonator-qubit coupling and (2) qubit-qubit coupling.

(1) Resonator-qubit dispersive coupling

For a composite system that consists of one resonator mode and one transmon mode, the energy levels are $E_{m,n} = \hbar(m\omega_r + n\omega_q + \frac{1}{2}n(n-1)\alpha)$, so we substitute it for the denominators of terms in (2.46) and we obtain,

$$\begin{aligned}\hat{\mathcal{H}}_{R-Q} &\approx \hat{\mathcal{H}}^{(0)} + \hat{\mathcal{H}}^{(1)} + \hat{\mathcal{H}}^{(2)} \\ &= \hbar\omega_r \hat{a}_1^\dagger \hat{a}_1 + \hbar\omega_q \hat{b}_2^\dagger \hat{b}_2 + \frac{\hbar\alpha}{2}\hat{b}_2^\dagger \hat{b}_2^\dagger \hat{b}_2 \hat{b}_2 + \hbar\sum_{n=0}(\Lambda_n + \chi_n \hat{a}_1^\dagger \hat{a}_1)\left|n\right\rangle\left\langle n\right|, \qquad (2.47)\end{aligned}$$

where, $\Lambda_n = \frac{ng^2}{\Delta_{q-r}+(n-1)\alpha}$, $\chi_n = \frac{ng^2}{\Delta_{q-r}+(n-1)\alpha} - \frac{(n+1)g^2}{\Delta_{q-r}+n\alpha}$, and $\Delta_{q-r} = \omega_q - \omega_r$. Practically, we operate a qubit in the computational basis $n = 0, 1$, so we consider the following truncated Hamiltonian.

$$\hat{\mathcal{H}}_{R-Q}/\hbar \approx \omega_r' \hat{a}_1^\dagger \hat{a}_1 - \frac{\omega_q'}{2}\hat{Z} - \chi \hat{a}_1^\dagger \hat{a}_1 \hat{Z}, \qquad (2.48)$$

$$\chi = \frac{g^2\alpha}{\Delta_{q-r}(\Delta_{q-r}+\alpha)}, \qquad (2.49)$$

where $\hat{Z} = \left|0\right\rangle\left\langle 0\right| - \left|1\right\rangle\left\langle 1\right|$, $\omega_r' = \omega_r - \frac{g^2}{\Delta_{q-r}+\alpha}$, $\omega_q' = \omega_q + \frac{g^2}{\Delta_{q-r}}$. Note that the dressed frequencies, ω_r' and ω_q', are the ones we observe in experiments and ω_r and ω_q are the bare frequencies. χ is the dispersive shift used for reading out the state of the qubit. Depending on the qubit's state, the operator $\hat{Z}$ puts positive or negative sign on the interaction operator $\pm\hbar\chi\hat{a}_1^\dagger \hat{a}_1$, which shifts the resonant frequency of the resonator to $\hbar\omega_r' \pm \chi$ depending on the qubit's state. We can therefore measure the qubit's state by sending a microwave signal to the coupled resonator and observing the magnitude and the phase response [51].

(2) Qubit-qubit dispersive coupling

Similarly, the second-order perturbation of the qubit-qubit coupling is written as,

$$\begin{aligned}\hat{\mathcal{H}}^{(2)}_{Q-Q} &\approx \hbar J^2 \sum_{m,n} \chi_{m,n} \left|m,n\right\rangle \left\langle m,n\right|, \qquad (2.50)\\ \chi_{m,n} &= \frac{m(n+1)}{\Delta_{12}+(m-1)\alpha_1/\hbar - n\alpha_2/\hbar} - \frac{(m+1)n}{\Delta_{12}+m\alpha_1/\hbar-(n-1)\alpha_2/\hbar},\end{aligned}$$

where $\Delta_{12} = \omega_{q_1} - \omega_{q_2}$, and the total perturbed Hamiltonian can be simplified in the computational basis as,

$$\hat{\mathcal{H}}_{Q-Q}/\hbar \approx -\frac{\omega'_{q_1}}{2}\hat{Z}_1 - \frac{\omega'_{q_2}}{2}\hat{Z}_2 + \frac{\zeta}{4}\hat{Z}_1\hat{Z}_2, \qquad (2.51)$$

$$\zeta = -\frac{2J^2(\alpha_1+\alpha_2)}{(\Delta_{12}+\alpha_1)(\alpha_2-\Delta_{12})}. \qquad (2.52)$$

where $\hat{Z}_1 = \hat{Z}\otimes\hat{I}$, $\hat{Z}_2 = \hat{I}\otimes\hat{Z}$, $\omega'_{q_1} = \omega_{q_1} + \frac{J^2}{\Delta_{12}} + \zeta/2$, $\omega'_{q_2} = \omega_{q_2} - \frac{J^2}{\Delta_{12}} + \zeta/2$. Note that bare qubit frequencies ω_{q_1} and ω_{q_2} include shifts made by qubit-resonator coupling derived in the previous subsection (the bare frequencies of $\hat{\mathcal{H}}_{Q-Q}$ correspond to ω'_q in Eq. (2.48)). We have plotted the coupling strength ζ depending on the detuning Δ_{12}, coupling J and anharmonicities α_1, α_2 in Figure 2.5.

The qubit-qubit dispersive coupling is often referred to as the "residual coupling" since the coupling persists as long as qubits are connected by fixed capacitance [56]. If we consider a larger grid of qubits, there are multiple always-on coupling with different coupling strengths that may seem too complex to use as a computational resource. However, since the coupling is already present after fabricating the device, if we could find a way to control them to shape the desired operation simultaneously, we would not have to add extra circuitry nor external drive to generate entanglement in a many-qubit system.

To make use of the static Hamiltonian (2.51), we adopt techniques from the Nu-

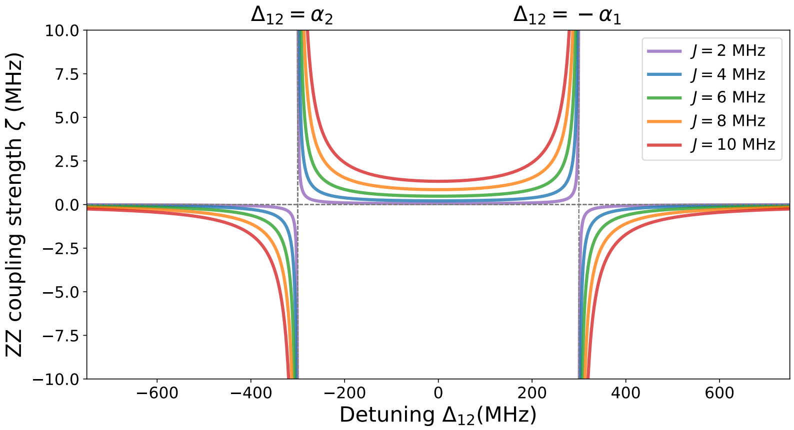

Figure 2.5: The ZZ coupling strength ζ depending on the detuning Δ_{12} and the capacitive coupling strength J. We observe poles at $\Delta_{12} = -\alpha_1$ and α_2.

clear Magnetic Resonance (NMR) community since their system has the same form of Ising Hamiltonian [61], and they have developed a dynamical decoupling pulse sequence [62] to operate quantum algorithms in such an always-on Hamiltonian. The idea is to use spin-echo sequences to decouple or refocus part of the coupling network during the time evolution such that the whole system evolves under desired effective Hamiltonian [63, 64]. In Chapter 5, we will introduce novel dynamical decoupling techniques to use the always-on ZZ coupling to operate arbitrary simultaneous two-qubit operation with much more efficient scaling in time and pulse count than in the conventional approach [35, 36].

2.2 Practice

In the previous section, we have introduced the circuit QED to give a theoretical background for manipulating and reading out quantum information in superconducting circuits, and the relation to the circuit theory was explained. This section covers details of the superconducting circuit and experimental apparatus operated in our lab to implement quantum computing experiments using superconducting qubits. The aim of this section is to bridge quantum physics and engineering by showing the methodology of quantum information processing in real-world devices.

2.2.1 Coaxial Circuit QED

In a typical circuit QED architecture, a qubit circuit and an LC resonator are coupled to compose one unit cell of a quantum processor and are accessed by control and readout lines. These components can be laid out in the same plane, similar to a CPU chip, using nano-fabrication technology in the silicon industry. However, the crowding of the circuit elements introduces cross-talks, unwanted decoherence channel and hinders the extensibility. Especially, the surface code, one of the most promising quantum error-correcting schemes, requires qubits to be laid out in a two-dimensional grid, which demands the control and readout lines to be accessed from an additional dimension.

In the coaxial circuit QED architecture, qubits and resonators are accessed by coaxial wiring running perpendicular to the circuit plane to overcome the processor chip crowding and the extensibility problems. The coaxial circuit QED architecture has a qubit and a resonator circuit fabricated on opposing sides of a substrate, and they are capacitively coupled through the substrate. We send and receive signals through out-of-plane wirings perpendicular to the superconducting circuit plane, which takes out wirings from the processor chip, minimising unnecessary cross-talks and decoherence channels. Fig. 2.6 shows the schematics of the coaxial circuit QED architecture. Both qubit and resonator circuits have inner and outer islands connected by a Josephson junction or a spiral inductor. The dimension of the circuits determines the crucial parameters of the qubit and the resonator that define the system Hamiltonian (2.36) of the circuit QED system. The anharmonicity of the qubit E_C is set by the radius of the inner island, and the Josephson inductance sets the

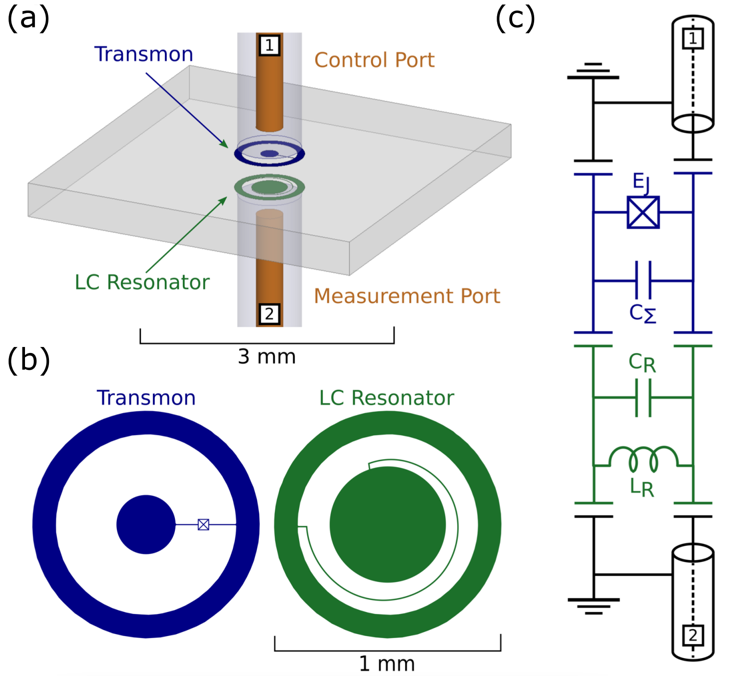

Figure 2.6: The Coaxmon architecture. (a) Schematic of the double-sided circuit QED architecture with perpendicular wirings. A resonator is printed on the opposite side of a qubit circuit, and they are capacitively coupled through the substrate. (b) Geometry of the transmon and the LC resonator circuits. (c) The equivalent circuit of the coupled transmon-resonator system in the Coaxmon architecture. Colours in the circuit diagram correspond to the colours of the transmon and the LC resonator diagrams of (b).

qubit's resonant frequency ω_q. We can set the resonator's resonant frequency ω_r by the inductance between the islands, determined by the length of the spiral inductance. The coupling between the qubit and the resonator can be represented by a lumped element model, and the coupling strength g can be predicted by computing the capacitance matrix of the coupled system by an electrostatic simulation. Furthermore, we can introduce coupling between qubits by adding capacitance arms between qubits shown in Fig. 2.7. The coupling strengths are determined by the overlap of the arms and the gap between them, and they can be simulated by the electrostatic simulation as well. The relation between the coupling strength and the dimension of the capacitance arms was investigated by a colleague in the lab [65].

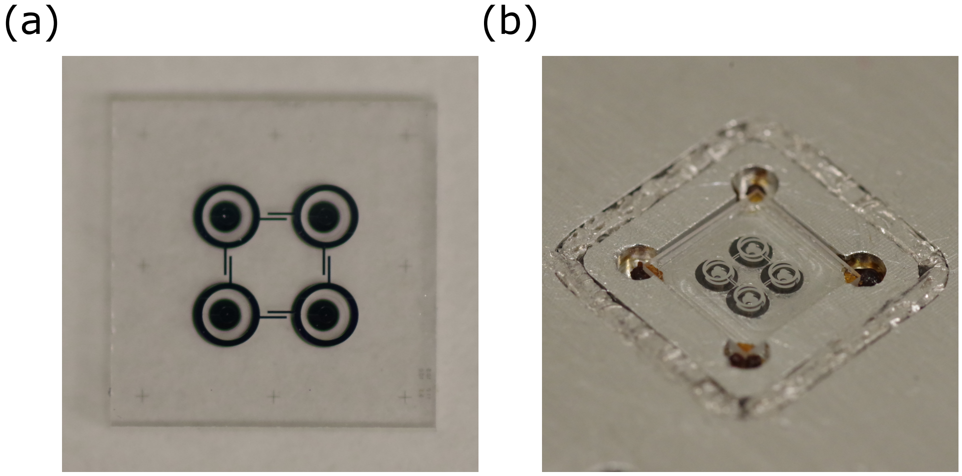

Figure 2.7: Photos of the four-qubit device used in this thesis. (a) Four coaxmon qubits coupled by capacitance arms. (b) The four-qubit sample mounted on a sample holder. The chip is fixed by GE varnish at the corner and the outer gap is filled with indium to electrically connect both sides of the sample holder.

For experiments presented in this thesis, we have used two samples, called device 2Q1 and 4Q3, the first generation two-qubit device and the third generation four-qubit device in our lab. They are designed and fabricated by colleagues in the lab, and the author of this thesis chose them for the main experiments in this thesis since their relatively strong coupling strengths were suitable for demonstrating the always-on quantum computing experiments. The author of this thesis characterised both devices, and the device parameters are listed in the Appendix A.1.

Sample holder

To hold the coaxmon chip firmly, we place it in an aluminium sample holder. Each unit of coaxmon is weakly coupled to coaxial cable pins from both sides to be accessed from external microwave electronics. Coaxial cable pins penetrate holes that are drilled through the sample holder perpendicular to the sample. The sample holder is covered by an aluminium magnetic shield to keep the sample unaffected by external magnetic field.

The distance between a qubit and a control pin is well-calibrated such that we can drive qubits sufficiently strongly and not let quantum information decay through the drive port. The decay to the external environment is quantified by κ, contributing to the T_1 obtained in experiments. The distance between a resonator and a pin is also crucial because the rate of reading out the quantum information from the resonator depends on how well they are coupled. The fast readout is essential when we want to do feedback measurements such as quantum error-correcting syndrome, so it would be better to have the pin distance as close as possible. At the same time, a qubit decays through the coupled resonator by the Purcell effect [59], so we want the resonator to be isolated from the environment as much as possible. As for the sample holders we used for our experiments presented in this thesis, we chose the pin distance to be $d_{\text{pin}} = 1.1$ mm not to limit the qubit lifetime.

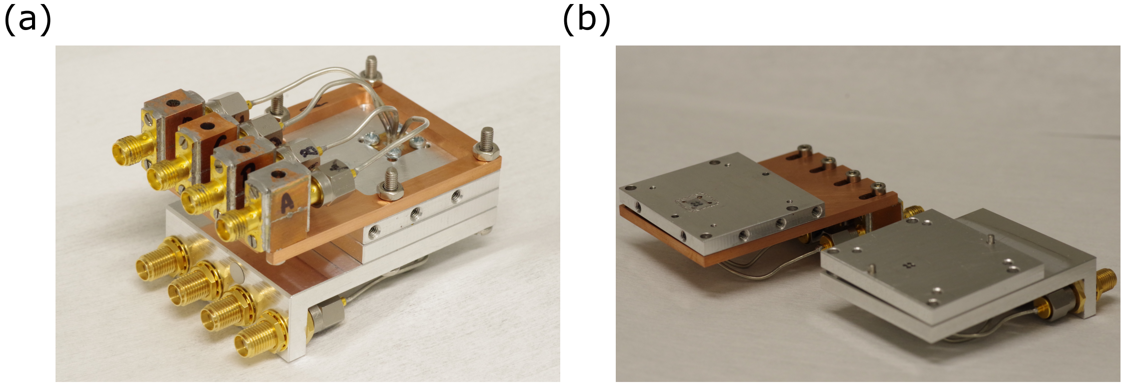

Figure 2.8: Sample holder for the four-qubit device. (a) Image of the assembled sampled holder. Eight SMA cable connectors are routed to four qubit ports and four resonator ports. (b) Image of the dismantled sample holder.

2.2.2 Signal input for qubits and resonators

To control qubits and perform the readout, we send coherent drives from the external microwave sources to qubits and resonators. The total Hamiltonian under the coherent drive can be described as $\hat{\mathcal{H}} = \hat{\mathcal{H}}_0 + \hat{\mathcal{H}}_d$, where $\hat{\mathcal{H}}_0$ is the static system

Hamiltonian and $\hat{\mathcal{H}}_d$ is the drive Hamiltonian,

$$\hat{\mathcal{H}}_d = \hbar\Big[\epsilon(t)\hat{a}^\dagger e^{-i(\omega_d t+\phi_d)} + \epsilon(t)^*\hat{a}e^{i(\omega_d t+\phi_d)}\Big], \tag{2.53}$$

which can be turned on and off on demand by choosing the time-dependent amplitude $\epsilon(t)$. For example, a coherent drive close to the qubit's resonant frequency can be written as,

$$\hat{\mathcal{H}}_{q+drive} = \hbar\omega_q\hat{b}^\dagger\hat{b} + \frac{\hbar\alpha}{2}\hat{b}^\dagger\hat{b}^\dagger\hat{b}\hat{b} + \hbar\epsilon_q(t)\Big[\hat{b}^\dagger e^{-i(\omega_d t+\phi_d)} + \hat{b}e^{i(\omega_d t+\phi_d)}\Big]. \tag{2.54}$$

If we set the drive frequency as $\omega_d = \omega_q - \delta_q$, the drive frame qubit Hamiltonian can be written as,

$$\begin{aligned}\hat{\mathcal{H}}'_{q+drive} &= \hbar\delta_q\hat{b}^\dagger\hat{b} + \frac{\hbar\alpha}{2}\hat{b}^\dagger\hat{b}^\dagger\hat{b}\hat{b} + \hbar\epsilon_q(t)\Big[\hat{b}^\dagger e^{-i\phi_d} + \hat{b}e^{i\phi_d}\Big] &(2.55)\\ &\approx -\frac{\hbar\delta_q}{2}\hat{Z} + \frac{2\hbar\epsilon_q(t)}{2}\Big[\cos\phi_d\hat{X} + \sin\phi_d\hat{Y}\Big], &(2.56)\end{aligned}$$

where the second line describes the coherent drive in the computational basis, and we can parameterise arbitrary single-qubit control by δ_q, ϕ_d and $\epsilon_q(t)$, which are tunable by external microwave electronics.

Similarly, when we drive the resonator at its resonant frequency $\omega_d = \omega_r$, we find the Hamiltonian as,

$$\hat{\mathcal{H}}_{r+drive} = \hbar(\omega_r + \chi\hat{Z})\hat{a}^\dagger\hat{a} + \hbar\epsilon_r(t)\Big[\hat{a}^\dagger e^{-i(\omega_r t+\phi_d)} + \hat{a}e^{i(\omega_r t+\phi_d)}\Big]. \tag{2.57}$$

In this instance, we have assumed that the qubit state is arbitrary, so we kept the dispersive coupling term $\chi\hat{Z}\hat{a}^\dagger\hat{a}$. Moving to a frame rotating at $\omega_d = \omega_r \pm \chi$, we see the resonator state evolves in different trajectories by,

$$\hat{\mathcal{H}}'_{r+drive} \;=\; \hbar\epsilon_r(t)\Big[\hat{a}^\dagger e^{-i(\mp\chi t+\phi_d)} + \hat{a}e^{i(\mp\chi t+\phi_d)}\Big], \tag{2.58}$$

depending on the qubit state. Reading out the output from the resonator at some time t specifies the state of the resonator in the phase space, which tells us whether the qubit was in the ground state or the excited state.

There are two measurement schemes to inspect the qubit-resonator systems: the continuous wave (CW) measurement and the pulsed measurement. CW measurement is useful in the initial phase of the system identification. The amplitude of the qubit drive, the resonator drive or both drives are fixed $\epsilon_q(t), \epsilon_r(t) = \text{const.}$, which only requires single-tone microwave drives from local oscillators without pulse shaping. Though, when both drives are simultaneously applied and are strong, we need to keep in mind that population in the resonator and the effect from multi-photon transitions might give a complicated result, which cannot be analysed straightforwardly by (2.56) and (2.58). Also, in the standard implementation of quantum algorithms, we do not want to populate the resonator during the qubit manipulation, so we do not use the CW approach for quantum algorithm implementation.

On the other hand, the pulsed measurements avoid simultaneous drive of the qubit control and the readout by pulsing each drive and applying them sequentially. The experimental setup for the pulsed measurements requires up-conversion described in the Fig. 2.9. The shape of the pulse is digitally defined by a computer, which then gets translated to an analogue signal by the Digital-to-Analog (DAC) converter. The DAC output goes to an IQ mixer where it gets up-converted by a high-frequency local oscillator. Finally, the up-converted signal goes inside the fridge through the driveline with suitable attenuation and filtering before driving the qubit-resonator system, which we will cover in the next section.

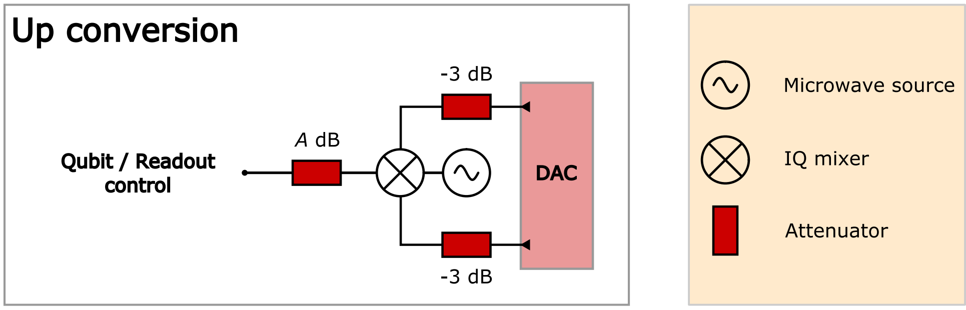

Figure 2.9: Schematic of the signal up conversion. In this diagram, the signal flows from the DAC to the qubit and readout control drive line. The IQ mixer combines the DAC signal with the local oscillator to be upconverted. The attenuator after the IQ mixer can be anything from $A = 0$dB for strong driving to $A = 30$dB for weak measurement.

2.2.3 Cryogenic setup for quantum measurements

To implement quantum measurements, we need to make sure the sample, the environment and the signals operate at the quantum level. Specifically, the thermal noise from the environment and the external signal must be suppressed at a level where it does not destroy the quantum characteristics of the system. In the case of circuit QED experiments, we use the lowest two energy levels of the qubit and populate the resonator with a few photons. To keep the qubit and the resonator in the ground state, we need to prepare an ultra-cold environment to minimise the thermal population. Moreover, signals generated in the microwave electronics carry room-temperature noise to the system in the cold environment unless we properly filter the room-temperature noise, so we need to design the experimental setup such that the thermal noise becomes minimal. This subsection introduces how we manage a low-noise experimental setup for the circuit QED experiments.

Dilution refrigerator and cryogenic wiring

Typically, we set the qubit's resonant frequency around $\omega_q = 4 \sim 6$ GHz and the resonator's resonant frequency around $\omega_r = 8 \sim 10$ GHz. To prepare a qubit in the ground state at the thermal equilibrium, we keep the device under $T = 50$ mK so that the thermal population of the excited state becomes less than $\exp\left(-\frac{\hbar\omega_q}{\mathrm{k_B}\cdot 50\ \mathrm{mK}}\right) \approx 1$ %, where $\mathrm{k_B}$ is the Boltzmann's constant. Since a commercial dilution refrigerator operates at around 15 mK at the base, we thermally connect the sample holder to the base plate to keep the qubit and the resonator cold. Furthermore, since Aluminium reaches superconductivity at $T_C = 1.2$ K, we can observe the Josephson effect at the base of the dilution refrigerator. For the experiments presented in this thesis, we use an Oxford Instruments Triton XL dilution refrigerator.

However, qubits experience higher effective temperature than 15 mK in the typical superconducting qubit experiments [66] due to the noise coming from drive lines connected to room-temperature electronics. To suppress the thermal noise from the room-temperature electronics, we design chains of attenuators and filters for the drive and the readout lines to minimise unwanted excitation and thermal population. Fig. 2.10 summarises the essential components and the wiring inside the fridge, and we will explain each function below.

To suppress the black body radiation from the cascading temperature stages, approximately -60 dB attenuation is needed between 300 K and the base plate, so we distribute -20 dB attenuators at the 4 K, 200 mK and 15 mK stage. When the cooling power at each stage surpasses the heat dissipation of the attached attenuator, we can assume that the attenuator is in equilibrium and the noise level becomes at the level of the thermal noise of the attached plate.

After the chain of attenuators, qubit input lines connect to the sample holder directly. On the other hand, each resonator has access to two lines; an input line to populate photons in the resonator and an output line to collect the output signals from the resonator. Two lines are connected to a circulator that routes the input signal to the sample holder and the signal from the sample to exit the fridge through the output line. Conversely, the sequence of circulators shuts the room-temerature noise through the output line not to enter the sample holder. Filters between the circulator and

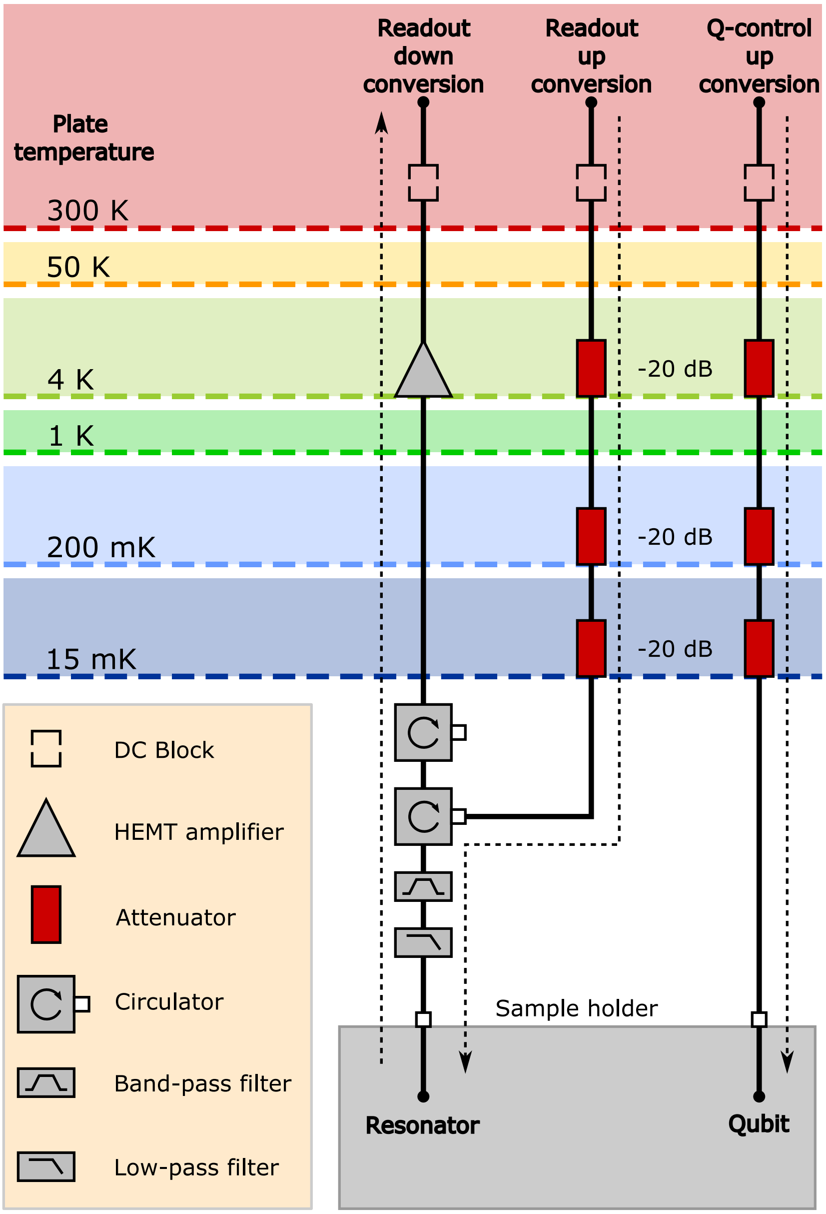

Figure 2.10: Schematic of the experimental setup and the signal flow in the dilution refrigerator. Input signals from external microwave sources go through chains of attenuators to minimise the inflow of the room temperature thermal noise. The signal output lines have circulators to allow signals to transmit in one direction where signals from the sample go out of the dilution refrigerator, but the thermal noise from the outside can not enter the quantum circuit.

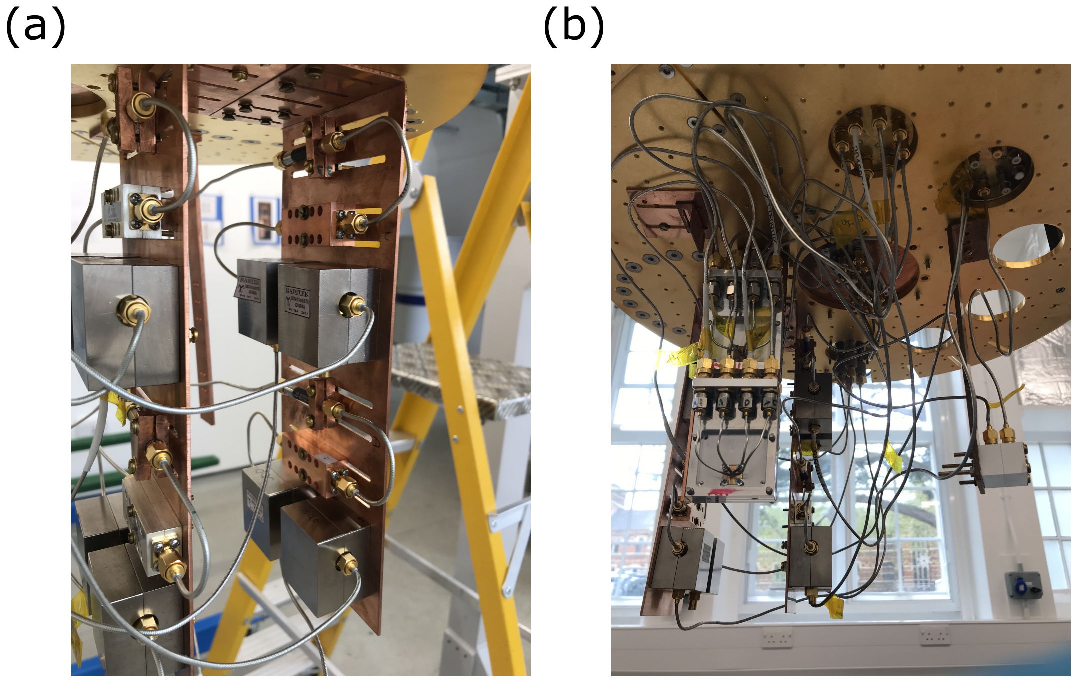

Figure 2.11: Photos of the wiring at the base plate. (a) Chains of circulators and filters in the output lines for four-qubit experiments. (b) Sample holders and signal input cables.

the sample holder minimise unnecessary frequency components of the input signal to reach the sample. The band-pass filter cuts the signal outside $8 \sim 12$ GHz, so the qubit drive does not enter the output line.

The wiring configuration of Fig. 2.10 allows us to implement transmission and reflective measurements. Both measurement methods collect data from the output line, but the transmission measurement is implemented by driving the resonator through the qubit port, and the reflective measurement is done by driving through the resonator port. In the output line, we use superconducting cables made of NbTi to minimise the signal loss after getting out of the sample holder. At the 4 K stage, we amplify the signal by the High Electron Mobility Transistor (HEMT), which is a commercially available amplifier that operates at 4 K. Although the HEMT effectively amplifies the signal with very little additional noise, the noise of the readout signal is limited to the noise temperature of the HEMT, which is 4 K, and this sets the ultimate limit of the signal detection efficiency of our measurement setup. Various superconducting non-linear devices such as Josephson Parametric Amplifiers (JPA) [67] and Josephson Travelling Wave Parametric Amplifiers (JTWPA) [68] achieve the near-quantum limited amplification at the base temperature, which could increase the signal-to-noise ratio and enable the single-shot readout in our system in the future.

2.2.4 Demodulation of the output signal

Outside the fridge, the output signals go through series of amplification and demodulation before they are recorded by a digital computer. The most important step in the process is the down conversion using an IQ mixer. The signal output from the fridge $\hat{V}_o(t) = A_o(e^{-\omega_{RF}t}\hat{a} + e^{\omega_{RF}t}\hat{a}^\dagger)$ and the local oscillator $V_{LO}(t) = A_{LO}\cos(\omega_{LO}t - \phi_{LO})$ get mixed at the IQ mixers as follows [56],

$$\begin{aligned} \hat{V}_{mix}(t) &= \hat{V}_o(t) \cdot V_{LO}(t) && (2.59) \\ &\approx \cos(\phi_{LO})\hat{V}_I(t) + \sin(\phi_{LO})\hat{V}_Q(t) && (2.60) \end{aligned}$$

where $\hat{V}_I(t) = A_{IF}[\cos(\omega_{IF}t)\hat{I} - \sin(\omega_{IF}t)\hat{Q}]$, $\hat{V}_Q(t) = A_{IF}[\cos(\omega_{IF}t)\hat{Q} + \sin(\omega_{IF}t)\hat{I}]]$, $A_{IF} = A_o \cdot A_{LO}$, $\omega_{IF} = \omega_{LO} - \omega_{RF}$, $\hat{I} = \frac{\hat{a}^\dagger + \hat{a}}{2}$ and $\hat{Q} = \frac{i(\hat{a}^\dagger - \hat{a})}{2}$. We have ignored the high-frequency terms in the second line since low-pass filters will filter them out after the IQ mixer. $\hat{V}_I(t)$ and $\hat{V}_Q(t)$ can be obtained by mixing the local oscillator having the phase of $\phi_{LO} = 0, \frac{\pi}{2}$, and the IQ mixers output these from the I-channel and the Q-channel. Lastly, signals from these channels get recorded by the Analog-Digital-Converter (ADC), and we then get on the frame rotating at ω_{IF} by applying a suitable

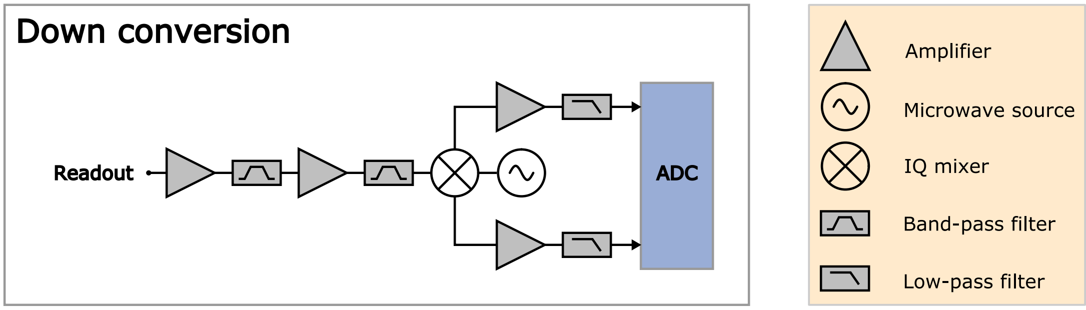

Figure 2.12: Schematic of the signal down conversion. In this diagram, the signal flows from left to right. The output signal from the sample goes through a chain of amplifiers with suitable filtering at each stage. The IQ mixer takes out the In-phase and the Quadrature-phase component of the signal, and the analogue-to-digital converter (ADC) transforms them into digital signals that can be stored in a computer.

rotation matrix digitally.

$$\begin{pmatrix} \hat{I}(t) \\ \hat{Q}(t) \end{pmatrix} = \begin{pmatrix} \cos(\omega_{IF} t) & \sin(\omega_{IF} t) \\ -\sin(\omega_{IF} t) & \cos(\omega_{IF} t) \end{pmatrix} \begin{pmatrix} \hat{V}_I(t) \\ \hat{V}_Q(t) \end{pmatrix} . \tag{2.61}$$

Finally, $\hat{I}(t)$ and $\hat{Q}(t)$ are integrated over some time window, and the integrated values are plotted on a two-dimensional plane so-called the I-Q plane, where we plot our measurement results in the later chapters.

Chapter 3

Calibration and tune-up of Circuit QED devices

In this chapter, we explain the experimental techniques to characterise and operate circuit QED devices. Previously, we have introduced the circuit QED theory and the hardware to realise quantum information processing in superconducting circuits. To make the hardware useful for practical applications, one has to develop a protocol that realises the high-fidelity operation of the quantum system, so an accurate system identification and calibration routine are required. Here, we introduce the procedure to systematically characterise a quantum circuit and calibrate control parameters for practical quantum algorithm implementation.

The calibration routine is categorised into two steps, system identification and quantum gate tune-up. The system identification is usually implemented in the early stage of experiments to identify the superconducting device's physical parameters. Device parameters found at this stage are essential in succeeding experiments and valuable for analysing experimental results and guiding the circuit design of the next-generation devices. After obtaining the basic device parameters, we implement a sequence of quantum control calibration experiments to maximise the quantum state's controllability. Since the device and the control systems drift over time, we need to repeat the calibration routine regularly. Therefore, it is vital to develop an efficient and accurate tune-up routine to calibrate the system to save time for the main experiments.

This chapter contains two sections, introducing the system identification and the quantum gate tune-up routine implemented in our lab. In the first part, we review the circuit QED representation of a two-qubit superconducting circuit and explain the characterisation routine to find the analytical model's parameters. In the second part, we will introduce the quantum gate calibration routine. For an overview of this chapter, Fig. 3.1 shows our tune-up routine and directs each step of the routine to the subsection in this chapter.

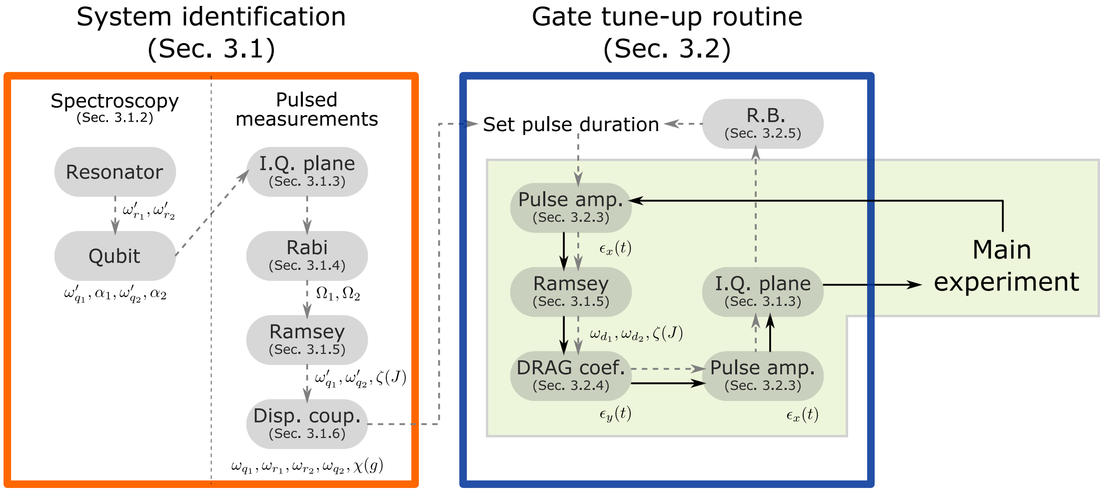

Figure 3.1: Overview of this chapter. Here we categorised experimental procedures to bring up a circuit QED system for quantum computing experiments. Grey dotted arrows indicate preparation experiments required before the main experiment. Black arrows show the calibration routine during the main experiment to minimise the systematic error caused by drifts of the instruments and the device parameters.

3.1 System identification

This section introduces procedures to characterise superconducting devices using the experimental setup presented in the previous chapter. Although classical electromagnetism and circuit theory play roles in characterising the basic circuit properties, the search for crucial experimental parameters in quantum information processing (QIP) requires experimental tools different from conventional electrical engineering. Specifically, to reveal the quantum properties of the superconducting circuits, we use spectroscopic and pulsed measurement techniques similar to those used in the nuclear magnetic resonance (NMR). Here, we introduce a sequence of experimental techniques (see the orange box in Fig. 3.1) to find superconducting circuit parameters linking several formulae derived in the theory chapter. This section aims to bridge the theory and practical aspects of the circuit QED formalism by giving concrete examples of the experimental results on device 4Q3[1].

3.1.1 The circuit QED model for a 2-qubit device

The goal of the system identification for the circuit QED system is to determine the circuit parameters from experimentally obtainable parameters. The more accurate the theoretical prediction is, the more precisely we learn about the system, which is crucial in analysing advanced experiments and designing new devices. As we have seen in previous sections, the circuit QED formalism plays a crucial role in interfacing between the theoretical model and experiments [11, 51, 69, 70]. In this section, we first review the circuit QED formulae that relate experimental observables to the device parameters. Particularly, we revisit equation (2.15), (2.23), (2.36), (2.41) from the previous chapter to model a system with two qubits and resonators. It serves as

---

[1] Device 4Q3 is a four qubit device fabricated by a colleague in our lab and we used two of the four qubits for our experiments. The device parameters are presented in the Appendix A.1

a suitable example to explain our system identification routine since the two-qubit system is the simplest coupled qubits system in multi-qubit architectures, and we use a two-qubit superconducting quantum processor in the main experimental results of this thesis. The total Hamiltonian of a 2-qubit device is as follows,

$$\hat{\mathcal{H}}_{Processor} = \sum_{i=1,2}\Big(\hat{\mathcal{H}}_{R_i} + \hat{\mathcal{H}}_{Q_i} + \hat{\mathcal{H}}_{R_i-Q_i}\Big) + \hat{\mathcal{H}}_{Q_1-Q_2} \tag{3.1}$$

$$\hat{\mathcal{H}}_{R_i} = \hbar\omega_{r_i}(\hat{a}_i^\dagger\hat{a}_i + \frac{1}{2}) \tag{3.2}$$

$$\hat{\mathcal{H}}_{Q_i} = \hbar\omega_{q_i}\hat{b}_i^\dagger\hat{b}_i + \frac{\hbar\alpha_i}{2}\hat{b}_i^\dagger\hat{b}_i^\dagger\hat{b}_i\hat{b}_i \tag{3.3}$$

$$\hat{\mathcal{H}}_{R_i-Q_i} = \hbar g_i(\hat{a}_i\hat{b}_i^\dagger + \hat{b}_i\hat{a}_i^\dagger) \tag{3.4}$$

$$\hat{\mathcal{H}}_{Q_1-Q_2} = \hbar J(\hat{b}_1\hat{b}_2^\dagger + \hat{b}_2\hat{b}_1^\dagger) \tag{3.5}$$

where, $\hat{a}_i$ and $\hat{b}_i$ are annihilation operators of a resonator and a qubit in the ith qubit-resonator unit cell. Parameters ω_{r_i} and ω_{q_i} are the resonant frequencies of a resonator and a qubit, α_i is the anharmonicity of the ith qubit, g_i is the coupling strength between a resonator and a qubit in a unit cell and J is the coupling strength between qubits. The cross-talk between a resonator and a qubit in different unit cells is negligible in this architecture, so we have ignored the inter-cell resonator-qubit coupling terms $\hat{\mathcal{H}}_{R_1-Q_2}$ and $\hat{\mathcal{H}}_{R_2-Q_1}$ [54]. We have designed our qubits in the transmon regimes, so the duffing oscillator approximation (3.3) and the rotating wave approximation (3.4), (3.5) are valid, and we consider that these parameters are sufficient to characterise and numerically simulate the target system.

The aim of this section's system identification protocol is to determine $\omega_{r_i}, \omega_{q_i}, \alpha_i, g_i$ and J by a sequence of experiments with a sensible order. The number of parameters that characterise a two-qubit quantum processor is eleven since it consists of two qubits, two resonators and three coupling capacitors. To determine these parameters, we implement different kinds of characterisation experiments such as resonator spectroscopy, qubit spectroscopy, Rabi oscillation, and Ramsey interferometry. In the following, we give a step-by-step introduction to the system identification protocol using data taken from actual experiments. Although we focus on the two-qubit case, the experimental sequence introduced in this section can be generalised to any number of qubits.

3.1.2 Device characterisation by spectroscopy

Resonator spectroscopy

In the circuit QED architecture, each qubit is coupled to a dedicated resonator to read out the qubit's state. Since it is difficult to observe transmons directly in the charge basis [51], the first step of the circuit QED experiment is to inspect the resonators' physical properties. Typically, a resonator is modelled as an LC circuit, so we have a rough estimate of the resonant frequency by the circuit design and its electrostatic simulation.

Having a rough estimate of the resonator frequency, we search for the more precise frequency by spectroscopy, an experimental technique originated in the atomic physics community. The spectroscopy is implemented by sending a continuous-wave microwave drive to the system and sweeping the drive frequency to find the resonance. Fig. 3.2 shows the S_{11} response of a reflective measurement on one of the resonators used in our experiments. By fitting the resonator response using the fitting routine developed by Peter Spring and Matthias Mergenthaler [54], we have found 4Q3/Q1's resonator's resonant frequency $\omega_{r0}/2\pi = 10.837$ GHz, the internal quality factor $Q_{int} = 3.2 \times 10^4$ and the external quality factor $Q_{ext} = 6.3 \times 10^3$. Note that the resonator that is dispersively coupled to a qubit has a different resonant frequency depending on the qubit's state, and the resonant frequency obtained here is the one with the qubit in the ground state.

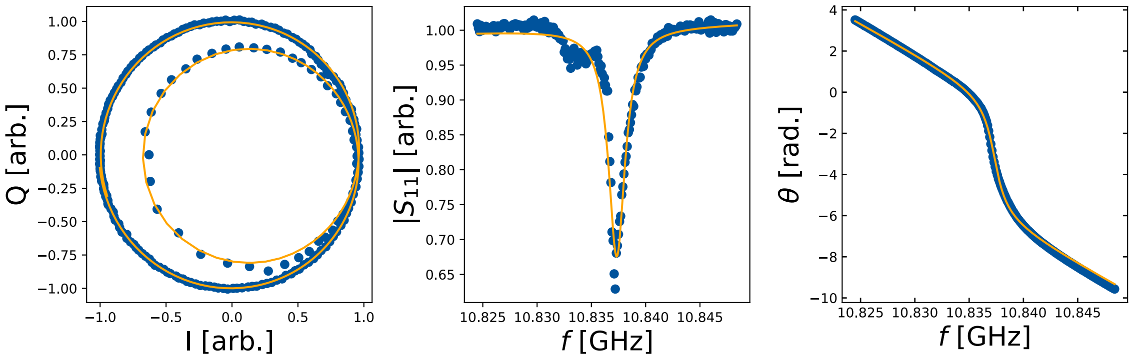

Figure 3.2: Resonator spectroscopy plotted in magnitude, phase and the IQ plane. By fitting the resonator response, we obtain the resonant frequency $\omega_r/2\pi = f_r = 10.837$ GHz, the internal quality factor $Q_{int} = 3.2 \times 10^4$ and the external quality factor $Q_{ext} = 6.3 \times 10^3$. The fitting function takes the effects of the signal lines into account and the details of the function can be found in [54].

Qubit spectroscopy

In the qubit spectroscopy, the resonator response is used as a reference to find the qubit's resonant frequency. In addition to the microwave drive fixed to the resonator's resonant frequency ω_{r0}, we send another drive to the qubit and sweep the drive frequency. Assuming that the qubit and the resonator are dispersively coupled, we can expect that the resonator's resonant frequency gets shifted depending on the qubit's state [11]. When the qubit drive is on resonance with the qubit's resonant frequency, the qubit gets populated which results in the change in the resonator's response due to the dispersive shift. Fig. 3.3 shows the two-dimensional plot of the qubit spectroscopy swept by the qubit drive frequency and the qubit drive power. We can find multiple features flagged by change in the S_{11} response indicated by transition in colours and this is typical for a transmon qubit. From the plot, we can obtain the qubit's resonant frequency $\omega_{01}/2\pi = 6.780$ GHz and the anharmonicity $\alpha/2\pi = \omega_{02} - \omega_{01} = -322$ MHz, and we use this α to derive the charging energy E_C later in Subsec. 3.1.5.

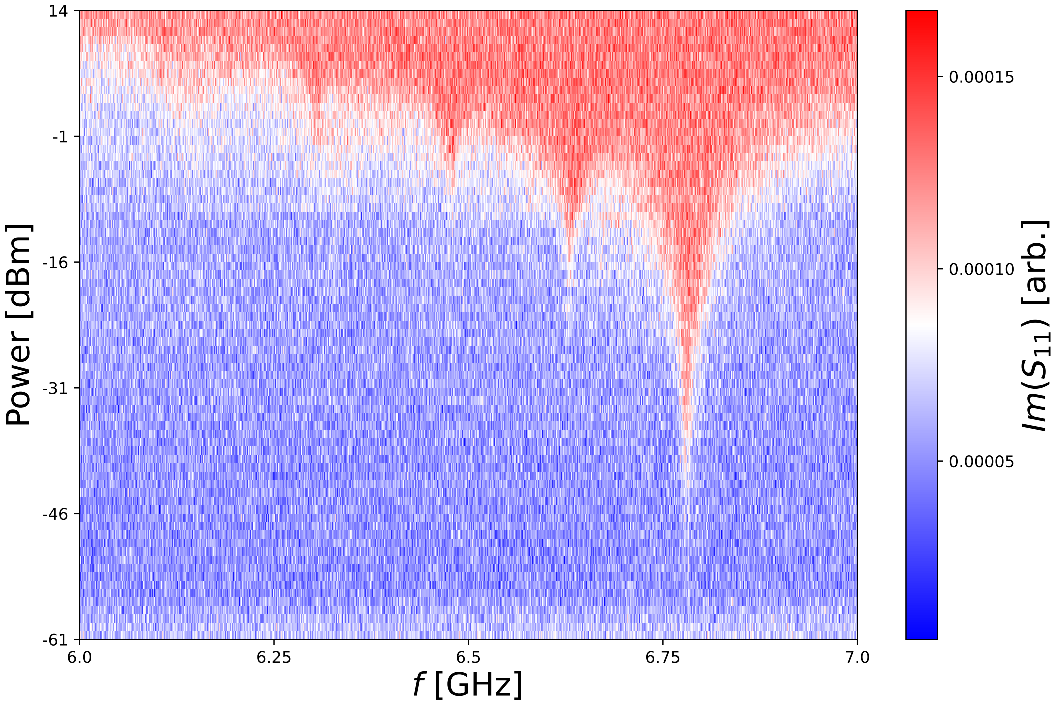

Figure 3.3: Qubit spectroscopy swept by drive frequency and power. The imaginary part of the reflected signal (S_{11}) is plotted on the graph, and the change in colour shows the resonance of the drive and qubit's transition frequencies. Five peaks in the plot are expected to be f_{01}, $f_{02}/2$, $f_{12} \approx f_{03}/3$, $f_{13}/2$, $f_{23} \approx f_{14}/3$ from right to left.

3.1.3 Quantum state discrimination on the IQ plane

Pulsed measurements

After obtaining the initial estimate of the qubit's and the resonator's resonant frequencies, we further characterise the system based on pulsed measurements. In the pulsed approach, we instruct qubit control and readout by a series of microwave pulses. This way, the resonator is in its ground state when the qubit is driven, which avoids the photon-number dephasing of the qubit. Also a qubit and a resonator are not driven simultaneously, so each dynamics is isolated from the other. Since the resonant frequency of a component in a dispersively coupled system depends on the population of the other component, it is important to fix the population of the qubit (resonator) when finding the control (readout) parameters of the resonator (qubit).

Readout result on the IQ plane

In the pulsed measurements, a resonator is populated only for a finite time, so we window the output signal to collect as much information and less noise as possible. As we introduced in Section 2.2.4, we demodulate the windowed output signal, and we obtain the In-phase voltage and the Quadrature phase voltage. Therefore, we can map the resonator's response of each measurement to a point on the IQ plane, and the result of the dispersive readout results in two different coordinates in the IQ plane depending on the qubit's state. When we prepare a qubit in the ground state or the excited state, and measure them many times, we see two clouds in the IQ plane as Fig. 3.4, and the spread of the distribution comes from the noise of the output signal. The signal-to-noise ratio (SNR) is defined by the ratio of the distance between the centre points of the distributions and the standard deviation. In the ideal case of high SNR, there is minimal overlap between each distribution so that we can set a threshold at the middle of each distribution and count the population of the qubit's state. With high SNR, we can even infer the qubit's state with single shot, which is vital for feedback measurements, but the so-called single-shot readout requires low-noise amplifiers such as JPA [67] or TWPA [68]. Since they are not available in our lab currently, we took an alternative approach called averaged measurements.

Without significant amplification, we typically find two distributions overlapping like Fig. 3.4(b), leading to infidelity in the single-shot readout. However, if we are only interested in the ensemble average of observables, which is the case for various applications such as quantum state tomography, the single-shot readout is unnecessary. Suppose we prepare a qubit in the steady-state and repeat the measurement

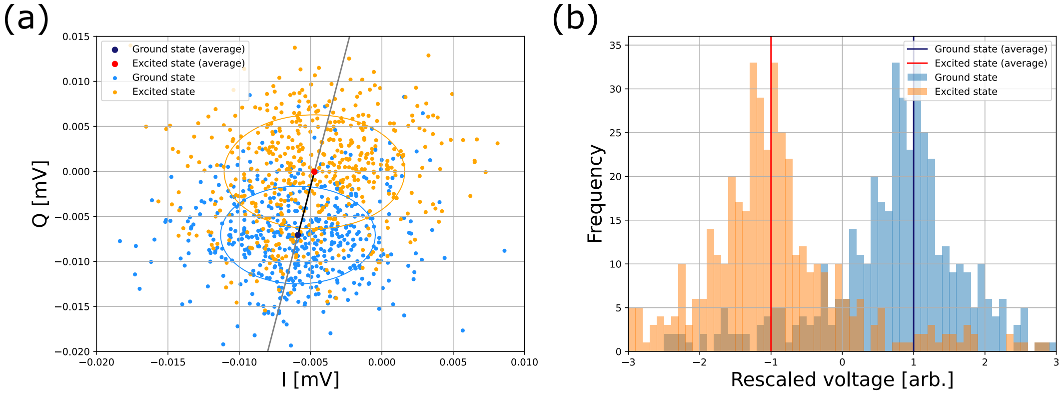

Figure 3.4: Quantum state discrimination in the IQ plane. (a) Single-shot measurement results on the IQ plane. Here, a qubit is prepared in the ground state (blue) or the excited state (orange). Dark blue and red dots are the average coordinates of the ground and the excited state results. Circles indicate that points inside the regions are within the standard deviation from the averaged points. We define our z-basis on the black line between the blue and the red points. When we measure a particular quantum state by the averaged measurement, we get an averaged point in the IQ plane, and we project it to the black line to obtain the expectation value $\langle \hat{Z} \rangle$. For example, the averaged point of the ground state (blue dot) returns $\langle \hat{Z} \rangle = 1$ and the excited state (red dot) returns $\langle \hat{Z} \rangle = -1$. (b) The distribution of measurement results prepared in the ground state (blue) or the excited state (orange). All shots in (a) are projected to the grey line to generate the histogram. The horizontal axis is rescaled to the same scale as the z-basis, where $+1$ (dark blue line) and -1 (red line) corresponding to the dark blue and red dots in (a) indicating the mean value of each distribution.

many times. The average of the measurement results converges to a point on the IQ plane, and we can define the steady state's coordinate as the ground state on the IQ plane. Similarly, we define the excited state on the IQ plane by measuring the qubit's excited state many times. Now, consider preparing a superposition state and taking the average of the measurement results. The averaged signal converges to a point and can be projected to a line that goes through the ground and the excited states coordinates. The population of the qubit state can be inferred by the internal ratio of the projected point dividing the line between the ground and the excited states (black line in Fig. 3.4). Throughout this thesis, we estimate the z-basis population

$\langle \hat{Z} \rangle$ using the averaged measurement, and denote the measured pseudo-population by $\langle \widetilde{Z} \rangle$.

In practical measurements, the reliability of the z-basis depends on how accurately we prepare the excited state, hence the fidelity of the π-rotation of the qubit. Although we do not assume a perfect π-pulse at the beginning of the calibration, later characterisation experiments such as the Ramsey interferometry and single-qubit gate pulse shaping are not sensitive to the absolute value of the z-basis, so we can proceed with the calibration routine with the tentative z-basis.

3.1.4 Rabi oscillation

We have seen in Section 2.2.2 that a qubit's state can be controlled by sending a microwave at the qubit's resonant frequency. To target a particular superposition state on the Bloch sphere (2.6), we shape our control pulse to a specific amplitude and phase. The most frequently occurring rotation angles are π and $\frac{\pi}{2}$, which are utilised in various characterisation experiments such as Ramsey interferometry, the Spin-echo experiment and the Randomised Benchmarking [71]. To find the suitable pulse parameters for the π and $\frac{\pi}{2}$ rotation, we first check the Rabi frequency of a given microwave drive. We implement the Rabi oscillation experiment by sending a square pulse of fixed-amplitude A to a qubit and sweeping the pulse duration, and we obtain the Rabi frequency Ω of the applied field (see Fig. 3.5).

Typically, we first decide the duration of the π and $\frac{\pi}{2}$ pulses and calibrate the pulse amplitudes experimentally. When the drive is not too strong, Ω scales linearly to A, so we can estimate the amplitude A' for a π-pulse of duration T' by the following extrapolation,

$$A' = \frac{\Omega'}{\Omega} A = \frac{A}{2\Omega T'}. \tag{3.6}$$

where $\Omega' = \frac{1}{2T'}$ is the target Rabi frequency of the drive that achieves π-rotation in time T'. The pulse area $A \cdot T$ is a useful metric for determining the pulse amplitude for other pulse shapes such as the Gaussian and the Blackman envelope. For example, the amplitude of a Gaussian pulse of duration T' can be set by calculating the amplitude A_G that makes the area inside the Gaussian envelope match $A' \cdot T'$,

$$\int_0^T A_G \exp\left(-\frac{(t - T'/2)^2}{2\sigma^2}\right) dt = A \cdot T, \tag{3.7}$$

where σ is the standard deviation that determines the curvature of the Gaussian envelope and we have assumed that the pulse is truncated at the edge.

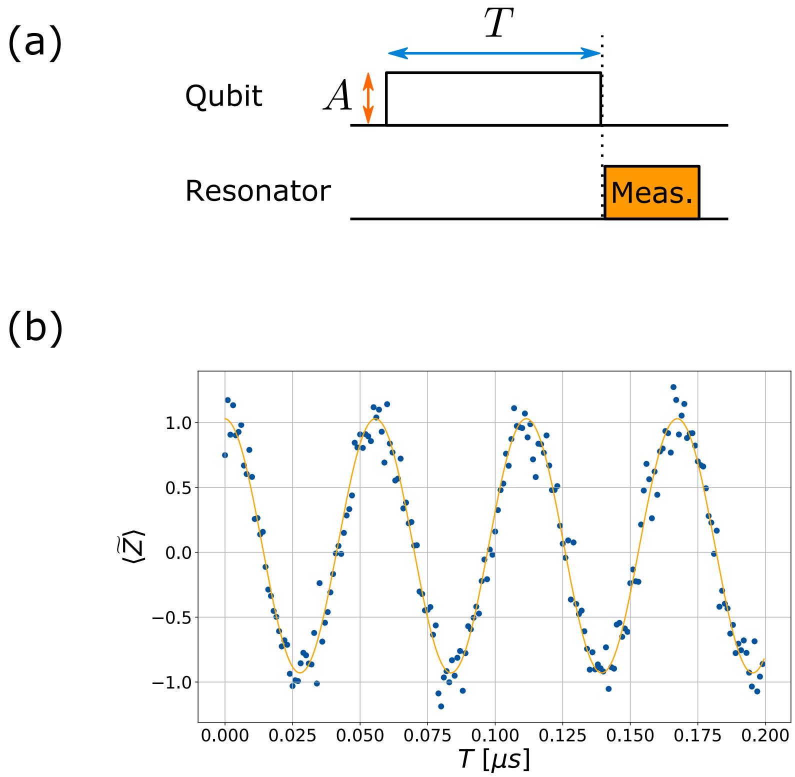

Figure 3.5: Rabi oscillation experiment. (a) Pulse sequence of the Rabi oscillation experiment. In the pulsed measurements, we send a qubit drive pulse and a measurement pulse without an overlap in time. (b) The data taken from the actual experiment. We estimate the Rabi frequency Ω by fixing the amplitude A and sweeping the duration T of the square pulse.

The Rabi oscillation experiment is relatively robust to the miscalibration of qubit's drive frequency, so we chose this experiment as the initial step of the pulse calibration. The fidelities of π and $\frac{\pi}{2}$ pulses generated by the simple Rabi oscillation experiment are sufficient for other characterisation experiments introduced in this section and further improvement of the single-qubit gate fidelity requires the drive frequency calibration by Ramsey interferometry, so we leave further pulse shaping calibration to the next section.

3.1.5 Ramsey interferometry

To minimise the qubit drive detuning, we find the more accurate qubit resonant frequencies by Ramsey interferometry experiments [72].

The pulse sequence of the Ramsey interferometry on one qubit is indicated in the Fig. 3.6. First, we prepare a qubit in the superposition state $|+\rangle = \frac{1}{\sqrt{2}}(|0\rangle + |1\rangle)$ by applying $\hat{Y}_{\frac{\pi}{2}}$ pulse to the ground state $|0\rangle$. We then let the qubit evolve under the drive frame Hamiltonian for time t,

$$\hat{\mathcal{H}}'/\hbar = \frac{1}{\hbar}(\hat{U}^{\dagger}\hat{\mathcal{H}}\hat{U} - i\hat{U}^{\dagger}\frac{\partial\dot{\hat{U}}}{\partial t}) = -\frac{\omega_q - \omega_d}{2}\hat{Z} = -\frac{\delta}{2}\hat{Z}, \tag{3.8}$$

where $\hat{\mathcal{H}} = -\frac{\hbar\omega_q}{2}$ is the lab frame Hamiltonian and $\hat{U} = \exp\Big(-\frac{\omega_d}{2}\hat{Z}\Big)$ is the unitary transformation to the drive frame of frequency ω_d. In the Ramsey interferometry

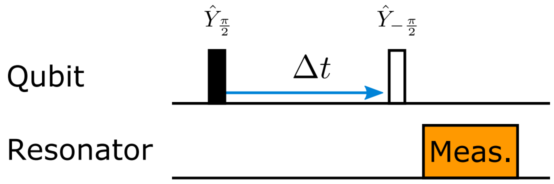

Figure 3.6: Pulse sequence of the Ramsey interferometry experiment. The black and white bars represent $\hat{Y}_{\frac{\pi}{2}}$ and $\hat{Y}_{-\frac{\pi}{2}}$ gates separated by a free-evolution of the background Hamiltonian $\hat{\mathcal{H}} = -\frac{\hbar\omega_q}{2}$ for Δt.

experiment, we find the detuning δ by measuring the qubit state in the x-basis. This is equivalent to applying $\hat{Y}_{-\frac{\pi}{2}}$ pulse to the final state $|\psi(t)\rangle = \exp\Big(\frac{-i\hat{\mathcal{H}}t}{\hbar}|+\rangle\Big)$ and reading out the qubit state in the z-basis.

$$\langle\psi(t)|\,\hat{X}\,|\psi(t)\rangle = \langle\psi(t)|\,\hat{Y}_{\frac{\pi}{2}}\hat{Z}\hat{Y}_{-\frac{\pi}{2}}\,|\psi(t)\rangle = -\sin(\delta t) \tag{3.9}$$

3.1.6 Ramsey interferometry on ZZ-coupled qubits

The situation is different for always-on coupled qubits. When the dispersive coupling (2.51) to the other qubit cannot be neglected, the background Hamiltonian of a two-qubit system in the doubly-rotated drive frame $\hat{U} = \exp\Big(-\frac{\omega_{d_1}}{2}\hat{Z}\hat{I} - \frac{\omega_{d_2}}{2}\hat{I}\hat{Z}\Big)$ becomes,

$$\hat{\mathcal{H}}'_{Q-Q}/\hbar = -\frac{\omega'_{q_1}-\omega_{d_1}}{2}\hat{Z}\hat{I} - \frac{\omega'_{q_2}-\omega_{d_2}}{2}\hat{I}\hat{Z} + \frac{\zeta}{4}\hat{Z}\hat{Z} \tag{3.10}$$

$$= -\frac{\delta_1}{2}\hat{Z}\hat{I} - \frac{\delta_2}{2}\hat{I}\hat{Z} + \frac{\zeta}{4}\hat{Z}\hat{Z}, \tag{3.11}$$

where the dressed frequencies $\omega'_{q_1} = \omega_{q_1} + \frac{J^2}{\Delta_{12}} + \frac{\zeta}{2}$, $\omega'_{q_2} = \omega_{q_2} - \frac{J^2}{\Delta_{12}} + \frac{\zeta}{2}$ and the dispersive coupling strenth $\zeta = -\frac{2J^2(\alpha_1+\alpha_2)}{(\Delta_{12}+\alpha_1)(\alpha_2-\Delta_{12})}$ are obtained from Eq. (2.51). Since there are three parameters to find, such as the detunings of one-qubit terms and the dispersive coupling strength ζ, a single run of the Ramsey interferometry is not enough. Instead, we implement the following overcomplete set of four different Ramsey interferometry experiments to determine the two-qubit Hamiltonian,

1. Initialise $|\psi(0)\rangle = |+,0\rangle$, wait for time t and measure qubit 1 in the x-basis.
   Expected result : $\langle\psi(t)|\,\hat{X}\hat{I}\,|\psi(t)\rangle = \sin\big((-\delta_1 - \frac{\zeta}{2})t\big)$
2. Initialise $|\psi(0)\rangle = |+,1\rangle$, wait for time t and measure qubit 1 in the x-basis.
   Expected result: $\langle\psi(t)|\,\hat{X}\hat{I}\,|\psi(t)\rangle = \sin\big((-\delta_1 + \frac{\zeta}{2})t\big)$
3. Initialise $|\psi(0)\rangle = |0,+\rangle$, wait for time t and measure qubit 2 in the x-basis.

Expected result: $\langle\psi(t)|\,\hat{I}\hat{X}\,|\psi(t)\rangle = \sin\bigl((-\delta_2 - \frac{\zeta}{2})t\bigr)$

4. Initialise $|\psi(0)\rangle = |1, +\rangle$, wait for time t and measure qubit 2 in the x-basis.

   Expected result: $\langle\psi(t)|\,\hat{I}\hat{X}\,|\psi(t)\rangle = \sin\bigl((-\delta_2 + \frac{\zeta}{2})t\bigr)$

Fig. 3.7 shows an example of the two-qubit Ramsey interferometry experiment, which we find the qubit frequencies $\omega'_{q_1} = 6780.24$ MHz, $\omega'_{q_2} = 7082.78$ MHz and the dispersive coupling strength $\zeta = -3.91$ MHz. With these parameters and Eq. (2.51), (2.52), we obtain the qubit-qubit coupling strength $J = 8.475$ MHz.

The two-qubit Ramsey interferometry experiment is crucial for our experiments since the qubit-qubit dispersive coupling ζ plays an important role in the quantum algorithm implementation. Due to the qubit frequencies' drifts, the drive frequency detunings and the dispersive coupling strength changes over time. Therefore, we frequently monitor the coupling strength and recalibrate drive frequencies by the

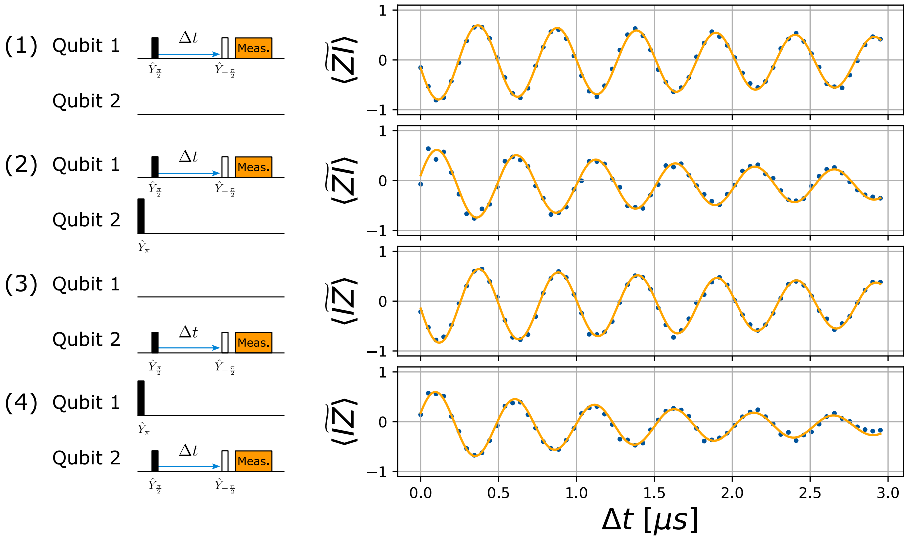

Figure 3.7: Pulse sequence and the experimental result of a two-qubit Ramsey experiment. Pulse sequences are indexed following the numbering of the experimental configurations mentioned in the main text. For simplicity of the diagram, we have put the measurement pulse and the qubit drive pulse on the same line.

two-qubit Ramsey experiment to minimise drift errors.

3.1.7 The dispersive coupling strength

The last parameter to fully characterise the two-qubit system is the dispersive coupling between a qubit and a resonator. To find the dispersive shift, we populate the qubit and observe the resonator's resonant frequency shift. Here, we excite the qubit by a π-pulse and implement the pulsed resonator spectroscopy by sweeping the drive frequency of the measurement pulse. Fig. 3.8 shows the result of the resonator spectroscopy on the first resonator of the device 4Q3 having two dips. The left dip corresponds to the resonator's resonant frequency when the qubit is excited, and the right dip is when the qubit is in the ground state. We observe two dips in the same spectroscopy because part of the excited state population relaxes during the measurement, and the resonator spectroscopy reflects both effects from the excited and the ground state population. The difference frequency between the two dips corresponds to twice the dispersive shift $\chi = 1.95$, and the centre frequency was $\omega_r' = 10835.2$ MHz. With these parameters and Eq. (2.48), (2.49), we obtain the coupling strength $g = 327.5$ MHz, the bare qubit frequency $\omega_q = 6806.7$ MHz and the bare resonator frequency $\omega_r = 10810.7$ MHz.

In this section, we provided a step-by-step introduction to fully characterising a two-qubit circuit. The sequence of characterisation experiments provided sufficient parameters such as ω_{r_i}, ω_{q_i}, α_i, g_i (i=1,2) and J to model the system using Eq. (3.1), (3.2), (3.3), (3.4) and (3.5).

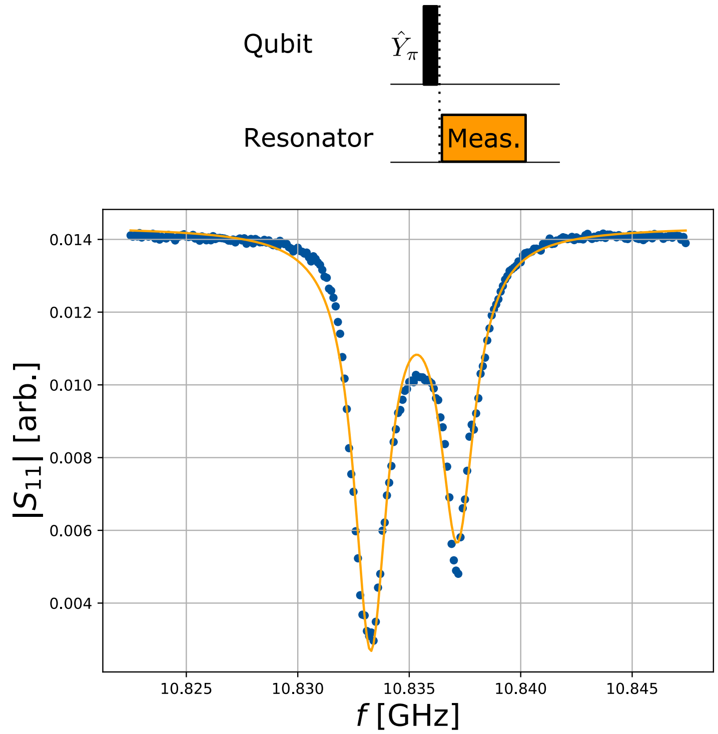

Figure 3.8: Resonator spectroscopy and the dispersive shift. Each data point in the graph is the average of 10,000 shots. Due to the averaged measurement, the resonator's response reflects both effects from the excited (left dip) and the ground (right dip) state population of the qubit.

Sec.	Parameter	2Q1		4Q3		Method
		Q1	Q2	Q1	Q2	
3.1.2	$\alpha/2\pi$ [MHz]	-299	-310	-322	-294	Qubit spectroscopy
3.1.6	$\omega'_q/2\pi$ [MHz]	6581.2	6047.3	6780.2	7082.8	State-dependent Ramsey
	$\zeta/2\pi$ [MHz]	-0.942		-3.908		
	$J/2\pi$ [MHz]	13.56		8.475		$\omega'_q, \alpha, \zeta \rightarrow$ Eq. (2.51), (2.52)
3.1.7	$\omega'_r/2\pi$ [MHz]	10542.0	9499.0	10835.2	11308.2	State-dependent spectroscopy
	$\chi/2\pi$ [MHz]	2.93	2.62	1.95	2.30	
	$g/2\pi$ [MHz]	406.8	331.1	327.5	386.5	$\omega'_r, \omega'_q, \alpha, \chi \rightarrow$ Eq. (2.48), (2.49)
	$\omega_r/2\pi$ [MHz]	10503.2	9469.9	10810.7	11275.1	
	$\omega_q/2\pi$ [MHz]	6623.0	6079.1	6806.7	7118.2	

Table 3.1: Summary of the system characterisation experiments introduced in this section and obtained values for devices we used for this thesis.

3.2 Quantum gate calibration routine

In the previous section, we have introduced the experimental procedure to characterise superconducting devices. To make the most of the characterised device for quantum information processing, we calibrate the control signal to maximise the quantum control fidelity. Building on top of the infrastructure and experimental techniques introduced in the previous sections, we will demonstrate our methodology to bring up the control system for quantum algorithm experiments. First, we overview the whole tune-up routine and discuss the motivation. We then introduce a detailed procedure of the tune-up routine and gate characterisation experiments to realise high-fidelity gates. To demonstrate the idea of the calibration routine, we chose relevant experimental results on device 2Q1 and 4Q3.

3.2.1 Overview and motivation

The goal of the gate calibration routine is to find the optimal pulse shape $\epsilon(t)$ in the following drive Hamiltonian to achieve the highest control fidelity.

$$\hat{\mathcal{H}}_{q_{drive}} = \hbar\epsilon_q(t)\left[\hat{b}^\dagger e^{-i(\omega_d+\phi_d)} + \hat{b}e^{i(\omega_d+\phi_d)}\right] \tag{3.12}$$

In principle, we can simulate the quantum device's behaviour by the physical model (3.1), (3.2), (3.3), (3.4) and (3.5), with the device parameters ω_{r_i}, ω_{q_i}, α_i, g_i (i=1,2) and J obtained in the previous section. These physical models and measured parameters should allow us to find the optimal microwave pulse shape by analytically finding the solution [73] or by numerical simulation [74]. However, pulses obtained by the off-line optimisation can not be used straight away since Eq. (3.12) assumes an ideal situation where the exact pulse shape $\epsilon_q(t)$ arrives at the qubit, which is not the case in reality. Typically, we define the pulse shape $\epsilon_q(t)$ on a digital computer, transform it to an analogue microwave pulse by the digital-to-analogue converter, upconvert the pulse to the radio frequency signal and send it through the input line before it reaches the qubit. Each component contributes to the distortion of the pulse shape, and the drift of the microwave electronics hinders reproducibility. The gate calibration routine compensates for these nonidealities in the control system and improves the qubit's control fidelity by optimising the control parameters using actual qubit measurements. The calibration protocol connects the missing link between the signal definition and the actual waveform applied to the qubit without carefully characterising the transfer function of the control system.

Since we implement the calibration routine repeatedly to minimise errors from the drift, it is crucial to develop an efficient calibration routine to save as much time for the main experiment as possible. In addition, we need to make sure that the calibration routine is robust against variation in device parameters to avoid failure in finding the optimal control parameters. The failure often comes from searching a wrong parameter range in the control parameter space, so we start searching from a broader range and narrow it down until it reaches the optimum. Furthermore, the order of calibration experiments matters because some calibration experiments use single-qubit gates to characterise specific parameters, and we might misinterpret the result by imperfect single-qubit gates. It is a chicken-and-egg situation where we need to calibrate single-qubit gates using the calibration routine that relies on the performance of single-qubit gates. Therefore, we gradually bring up both the qubit gate fidelity and the accuracy of the calibration by tailoring specific order of experiments. Considering the trade-off between efficiency, robustness and the order of experiments, we have made our tune-up routine as a flowchart of Fig. 3.1, and we will introduce each step in the following subsections.

3.2.2 Pulse shaping

In the previous section, we have assumed square pulses for the pulsed measurements. However, the square pulse has a wide frequency spread in the Fourier space, leading unwanted transitions to non-computational states. Therefore, we shape pulses by Gaussian or Blackman windows, narrowing down the pulses' bandwidth to avoid unwanted transitions. Even with the windowing function, there are some leakages to the higher excited states when we drive the qubit very hard, so the pulse shaping that avoids such leakage is desirable. A specific analytic pulse shape to minimise the leakage to the 3rd level known as Derivative Removal by Adiabatic Gate (DRAG) has been developed, which eliminates the leakage and the detuning error that cause the control errors on transmon qubits [73]. The DRAG uses the second quadrature of the pulse to minimise the leakage and dynamically control the drive frequency to reduce the detuning error caused by the ac-Stark shift,

$$\epsilon_y(t) = \frac{\epsilon_x}{2\pi\alpha}, \tag{3.13}$$

$$\delta(t) = \frac{\epsilon_x^2(t)}{4\pi\alpha} \tag{3.14}$$

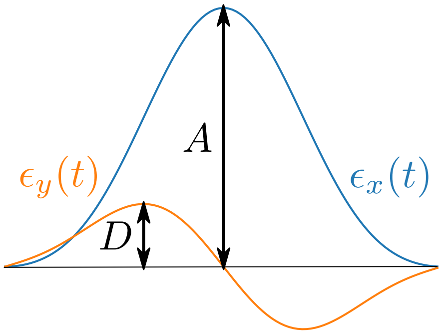

Figure 3.9: The DRAG correction applied to a pulse shaped by the Blackman window. For later use, we define the maximum amplitude of the first quadrature as $A = \max|\epsilon_x(t)|$ and the maximum amplitude of the second quadrature as $D = \max|\epsilon_y(t)|$.

where ϵ_x, ϵ_y are the first and the second quadrature of the pulse and δ is the detuning of the drive frequency from the qubit's $0-1$ transition frequency [73]. We also implement a further refinement known as half-DRAG in our tune-up routine, which allows the DRAG correction without dynamically controlling the detuning [75]. Fig. 3.9 shows the example pulse shaped by the Blackman window with the DRAG correction. Overall, the optimisation of the single-qubit gates with the half-DRAG correction requires only two parameters, the amplitude of the pulse A and the DRAG coefficient $d_{\mathrm{DRAG}} = \frac{D}{A}$, which significantly reduces the calibration complexity.

3.2.3 Amplitude tune-up

As we mentioned in the previous section, the rotation angle of the single-qubit operation is proportional to the pulse amplitude and duration. Typically, we fix the duration and optimise the pulse amplitude experimentally. As an initial guess, we set the pulse amplitude using the result from the Rabi oscillation experiment and normalising the pulse amplitude depending on the shape of the envelope. To further calibrate the pulses, we fine-tune the pulse amplitude by applying pulse trains to amplify over or under rotation errors. For example, the rotation error of $\hat{X}_{\frac{\pi}{2}}$ pulse can be amplified by the following pulse train experiment,

1. Initialise a qubit in the superposition state $|\psi\rangle_0 = |+\rangle$.
2. Apply $\hat{X}_{\frac{\pi}{2}}$ $(\hat{X}_{\pi})$ pulse $4n$ $(2n)$ times and take a measurement in the z-basis: $\langle\widetilde{Z}\rangle_n$.
3. Repeat 1. and 2. with increasing $n = 1, 2 \ldots N$.
4. Find the rotation error per gate, δ, by fitting the results $\langle\widetilde{Z}\rangle_n = 4n\delta$.

For small δ, the rotation error scales linearly to the number of pulses because when the initial state is prepared in the equator of the Bloch sphere, the total rotation

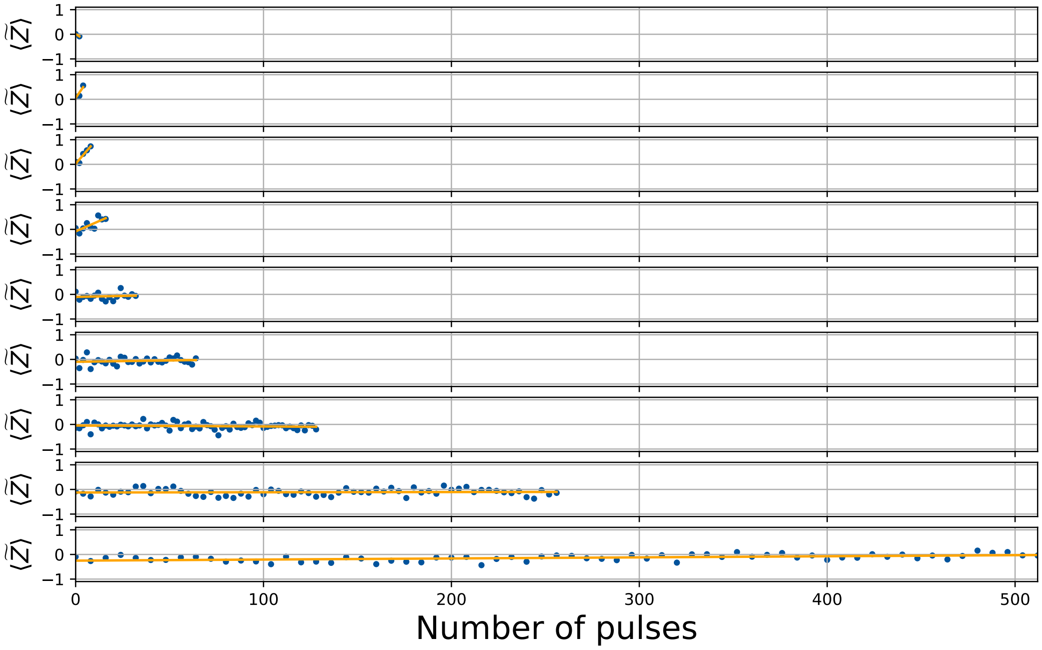

Figure 3.10: Experimental results of the amplitude calibration. Blue points indicate the final state populations after the application of pulse trains with increasing number of pulses $N = 2, 4, 8, 16, 32, 128, 256$ and 512. We can observe that the slopes of the fit is large at the beginning of the calibration ($N = 2, 4, 8, 16$), which indicate large rotation errors before the calibration.

error measured in the z-basis scales as $\sin(n\delta) \approx n\delta$. On the other hand, when the qubit was prepared in $|0\rangle$ or $|1\rangle$, the measured result scales quadratically as $\cos(n\delta) \approx 1 - \frac{(n\delta)^2}{2}$ for small δ. The quadratic scaling of the error amplification in the z-basis is much smaller than the linear scaling, so we chose to initialise the qubit in the superposition state $|+\rangle$. As we can see from the example run of the $\hat{X}_{\frac{\pi}{2}}$ pulse tune-up shown in Fig. 3.10, it takes multiple runs until it reaches the optimum. Each time we find the rotation error δ, we correct the pulse amplitude and repeat the procedure $1, 2, 3$ and 4 with increasing N until the amplitude converges. This approach allows an experimentalist to tune up high-fidelity gates by extending pulse trains until decoherence dominates the error.

3.2.4 DRAG tune-up

DRAG correction to the original pulse envelope mitigates the leakage and the detuning errors. Here, we define the DRAG coefficient d_{DRAG} as the ratio of the second quadrature amplitude D to the first quadrature amplitude A in Fig. 3.9,

$$d_{\mathrm{DRAG}} = \frac{D}{A} = \frac{\max|\epsilon_y(t)|}{\max|\epsilon_x(t)|} \tag{3.15}$$

and the initial guess of d_{DRAG} is calculated by the theoretical predication Eq. (3.13). To further fine-tune the pulse, we implement the following tune-up routine,

1. Set d_{DRAG}, and apply a gate sequence of $\hat{X}_{\pi} - \hat{Y}_{-\pi} - \hat{X}_{\pi} - \hat{Y}_{\pi}$.
2. Apply $\hat{Y}_{\frac{\pi}{2}}$ or $\hat{Y}_{-\frac{\pi}{2}}$ and measure in the z-basis to obtain $\langle \widetilde{Z}(d_{\mathrm{DRAG}})\rangle_{+}$ or $\langle \widetilde{Z}(d_{\mathrm{DRAG}})\rangle_{-}$.
3. Repeat 1. and 2. by sweeping d_{DRAG}.
4. Fit $\langle \widetilde{Z}(d_{\mathrm{DRAG}})\rangle_{\pm} = \pm\delta \cdot d_{\mathrm{DRAG}}$ and choose d_{DRAG} at the intersection.

$\pm\delta$ can be obtained by the slopes of the fits. The pulse sequence at step 1 and the final gate $\hat{Y}_{\pm\frac{\pi}{2}}$ at step 2 are chosen such that the measurement result scales linear to δ with opposite signs and can find the intersection where the error is minimal. The measurement results and the fits are displayed in Fig. 3.11.

3.2.5 Benchmarking gates

Randomized benchmarking

Having gates tuned up, we then evaluate the gate fidelity by the randomised benchmarking protocol [71, 76]. The gate fidelity obtained by randomised benchmarking is regarded as a cross-platform metric used to evaluate the performance of various

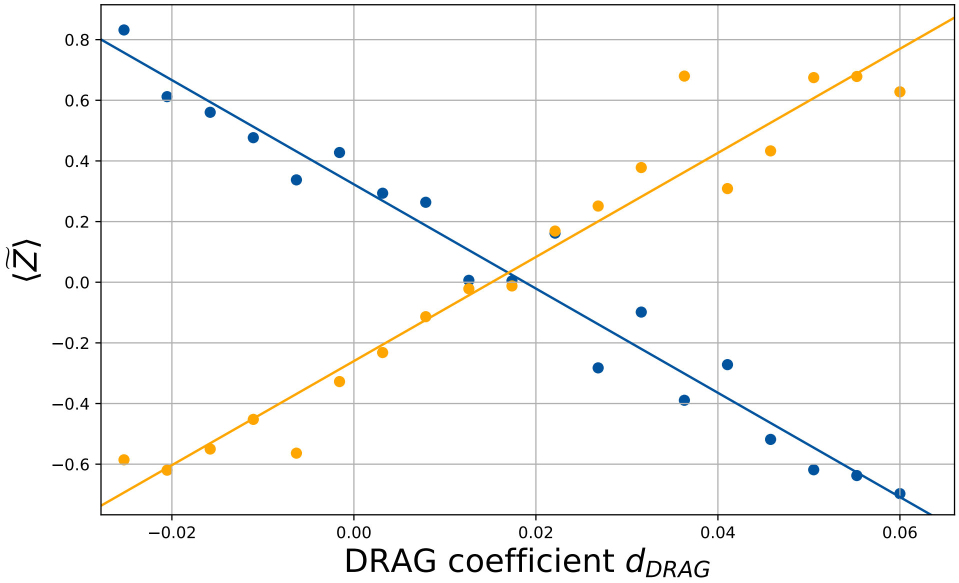

Figure 3.11: DRAG coefficient calibration. Orange (Blue) points indicate the result of $\langle\widetilde{Z}(d_{DRAG})\rangle_{+}$ ($\langle\widetilde{Z}(d_{DRAG})\rangle_{-}$).

hardware [8, 77, 78]. Here, we explain the randomised benchmarking protocol, the experimental results and how we apply it to our tune-up routine.

Similar to the amplitude tune-up, randomised benchmarking uses pulse trains to characterise small errors in gates. In a sequence of many gates, the success probability of the entire operation should decrease as we add gates. From this observation, we can roughly estimate the error per gate by the decay rate of the success probability to the number of gates in the gate sequence. However, since we don't have the knowledge of the error model of the gates, the gate sequence must not catch specific error, so we can not use a gate sequence that repeats the same gate like we did for the amplitude tune-up.

In the randomised benchmarking, applied gates are random so that a quantum state arrives at the random direction on the Bloch sphere in each step. We randomise the quantum state because we can balance the effects from various noise channels

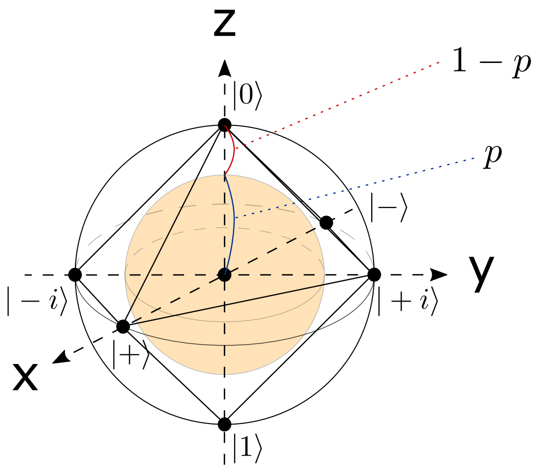

Figure 3.12: Depolarising channel and cardinal points of the Bloch sphere. The depolarising channel maps a pure state on the surface of the Bloch sphere to a state vector on a smaller sphere (orange) of radius p in the same direction. Cardinal points of the Bloch sphere corresponds to the eigenstates of one-qubit Pauli operators, $|0\rangle$, $|1\rangle$, $|\pm\rangle$ and $|\pm i\rangle$.

such as rotation error, energy relaxation and decoherence, whose effects on the system depend on the qubit's state[2]. This noise randomisation technique is called ”twirling” [76], where we can approximate the average error rate of the system's various noise channels by a depolarising channel,

$$\Lambda_d(\hat{\rho}) = p\hat{\rho} + \frac{1-p}{d}\hat{I} \tag{3.16}$$

where d is the system dimension and Λ_d is the superoperator that maps the input density matrix $\hat{\rho}$ to the depolarised density matrix $\hat{\rho}'$ [46]. Eq. (3.16) means the depolarising channel Λ_d preserves the same state $\hat{\rho}$ with probability p and completely mixes the state otherwise, which suits well with our objective to quantify the success probability of a given gate sequence. A random gate sequence of length l applied to a qubit ($d = 2$) results in a successive application of the depolarising channel Eq. (3.16)

---

[2] For example, a qubit in the ground state does not experience the energy relaxation and decoherence.

to the input state $\hat{\rho}_0$ for l times,

$$\hat{\rho}_l = \Lambda_2^l(\hat{\rho}) = p^l\hat{\rho} + \frac{1-p^l}{2}\hat{I} \tag{3.17}$$

and the success probabililty of a single shot of an experiment is defined by the state fidelity of the input state $\hat{\rho}_0$ and the final state $\hat{\rho}_l$,

$$p_l^{(i)} = \mathrm{Tr}(\hat{\rho}_0\hat{\rho}_l) = \mathrm{Tr}(\hat{\rho}_0\Lambda(\hat{\rho}_0)) = \frac{1}{2} + \frac{1}{2}p^l, \tag{3.18}$$

which decreases exponentially with increasing l. The last gate is the inverse of the previous gate sequence $\hat{U}_l = (\hat{U}_{l-1}\cdots\hat{U}_2\hat{U}_1)^{-1}$ so that the final state becomes the same state as the initial state if the application of the gate sequence was successful. Although Eq. (3.19) assumes no state preparation and measurement (SPAM) errors, in general, they will be absorbed in the y-intercept and the offset of the exponential curve,

$$p_l^{(i)} = Ap^l + B, \tag{3.19}$$

where $p_0^{(i)} = A + B$ absorbs both SPAM errors and $\lim_{l\to\infty} p_l^{(i)} = B$ reflects the measurement error. This way, the randomised benchmarking fidelity only depends on the decay rate p and is isolated from the state preparation and measurement (SPAM) errors, which could not be achieved in estimating the gate fidelity by quantum process tomography.

Typically, for a chosen gate sequence length l, we take K=40 random seeds and obtain the average success probability $\bar{p_l} = \sum_{i=1}^{K} p_l^{(i)}$. The average gate fidelity is defined by $F_{ave} = p + \frac{1-p}{d}$ and p can be obtained by fitting the experimental results $\bar{p_1}, \bar{p_2}, ..., \bar{p_L}$ for various gate sequence length $l = l_1, l_2, ..., l_L$. To save the number of

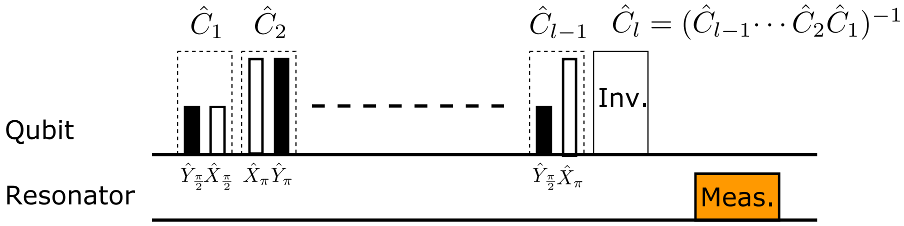

Figure 3.13: Randomised benchmarking pulse sequence. Each step of the random gate sequence is chosen from Clifford gates $\hat{C}_i$ ($i = 24$), which can be decomposed to basic physical gates. The inverse operation $\hat{C}_l$ brings back the final state to the initial state to check if the gate sequence was successful or not.

averaging, we sample from a sensible selection of discrete quantum states; cardinal points of the Bloch sphere (see Fig. 3.12), instead of random points on the Bloch sphere. This is equivalent to choosing random gates from the Clifford group[3] rather than picking from arbitrary SU(2) operation [76]. There are only twenty-four kinds of Clifford gates for single-qubit operation, so there is a significant reduction in the sampling space. Single-qubit Clifford gates can be decomposed by basic physical gates such as $\hat{X}_\pi$, $\hat{X}_{\frac{\pi}{2}}$, $\hat{Y}_\pi$, $\hat{Y}_{\frac{\pi}{2}}$ (see Appendix A.2), so we only need to calibrate pulse amplitude and the DRAG coefficient for π and $\frac{\pi}{2}$ rotations. Moreover, we can simulate the successive application of Clifford gates by classical computers [79], so the inverse operation $\hat{C}_l = (\hat{C}_{l-1}\cdots\hat{C}_2\hat{C}_1)^{-1}$ can be found efficiently. Due to the simulability of the Clifford circuit, randomised benchmarking is known to be scalable to the number of qubits, whereas the number of measurements in the quantum process tomography scales exponentially to the number of qubits.

Fig. 3.14 shows the result of the randomised benchmarking experiment of a Blackman pulse with time duration of $t = 36$ ns on device 2Q1. The obtained fidelity per Clifford gate to each qubit was, $F_{c,1} = 99.47 \pm 0.06\%$ and $F_{c,2} = 99.46 \pm 0.09\%$, and the fidelity per physical gate was, $F_{p,1} = 99.72 \pm 0.04\%$ and $F_{p,2} = 99.71 \pm 0.05\%$. The fidelity per physical gate can be calculated by considering the average number

---

[3] Single-qubit Clifford gates are single-qubit operations that map any cardinal points of the Bloch sphere to other cardinal points.

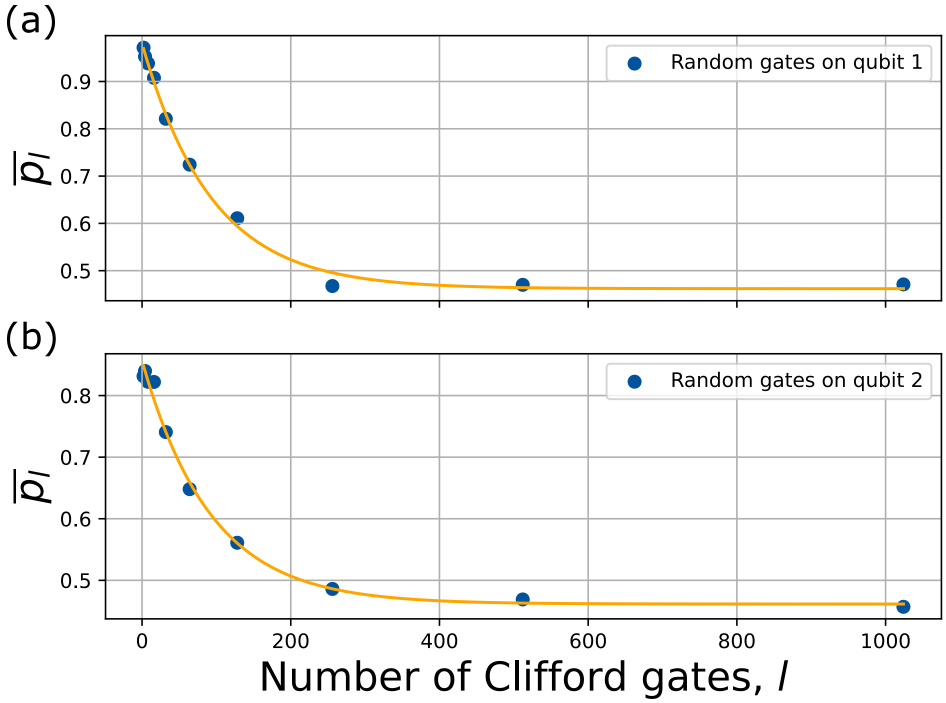

Figure 3.14: The result of the randomised benchmarking experiment on (1) qubit 1 (2Q1/Q1) and (2) qubit 2 (2Q1/Q2). The vertical axis is the final state population obtained by the population estimation protocol using the IQ plane introduced in Subsec. 3.1.3. We fit the average final state population $\bar{p}_l$ by an exponential function $\bar{p}_l = Ap^l + B$ to calculate the fidelity.

of physical gates per Clifford gate, $F_p = F_c^{\frac{1}{1.875}}$.

Simultaneous Randomized benchmarking

When we control coupled qubits, we are concerned about the cross-talk between them, and we can characterise the cross-talk by a variant of randomised benchmarking, called simultaneous randomised benchmarking. The simultaneous randomised benchmarking on two qubits compares the gate fidelity of the following experiments and extracts the addressability and the quantum cross-talk between the qubits.

1. Single-qubit randomised benchmarking on qubit 1

2. Single-qubit randomised benchmarking on qubit 2
3. Single-qubit randomised benchmarking on qubit 1 and 2 simultaneously

For each experiment $i = 1, 2, 3$, we measure the final state population $p_{00}^{(i)}$, $p_{01}^{(i)}$, $p_{10}^{(i)}$ and $p_{11}^{(i)}$ and calculate the success probability of the gate sequence. For example, in the first experiment, the success probability of the gate sequence can be described by the ground state population of the first qubit traced out by the second qubit; $p_1 = p_{00}^{(1)} + p_{01}^{(1)}$. The error per Clifford gate $r_1 = \frac{1-p_1}{2}$ can be obtained by the decay rate p_1 of the ground state population of the first qubit. On the other hand, we can measure the error per Clifford gate $r_2 = \frac{1-p_2}{2}$ of the second qubit by measuring the decay rate p_2 of the second qubit's ground state population $p_2 = p_{00}^{(2)} + p_{10}^{(2)}$. In the third experiment, $p_{00}^{(3)} + p_{01}^{(3)}$ ($p_{00}^{(3)} + p_{10}^{(3)}$) gives the success probability of the gate sequence for the first (second) qubit when the second (first) qubit is simultaneously driven, and we obtain the error per Clifford gate $r'_1 = \frac{1-p'_1}{2}$ ($r'_2 = \frac{1-p'_2}{2}$). The difference $\delta r_i = |r'_i - r_i|$ (i=1,2) tells us how much the simultaneous drive on the other qubit affects the average gate fidelity, hence gives us the information of the addressability to each qubit. Moreover, the correlated measurement gives us the magnitude of the quantum cross-talk in the system,

$$\delta\alpha = \alpha_{12} - \alpha_{1|2}\alpha_{2|1} \tag{3.20}$$

where α_{12} is the decay rate of the correlated population $p_{00}^{(3)} + p_{11}^{(3)}$, $\alpha_{1|2}$ and $\alpha_{1|2}$ gives the decay rate of the individual qubit's population $p_{00}^{(3)} + p_{01}^{(3)}$ and $p_{00}^{(3)} + p_{10}^{(3)}$.

Fig. 3.15 shows the result of the simultaneous randomised benchmarking experiment of a Blackman pulse with time duration of $t = 36$ ns on device 2Q1. The addressability defined by the error contribution from the other qubit was $\delta r_1 = 0.10 \pm 0.07\%$, $\delta r_2 = 0.24 \pm 0.12\%$ and the quantum cross talk was $\delta\alpha = 0.0077 \pm 0.0036$.

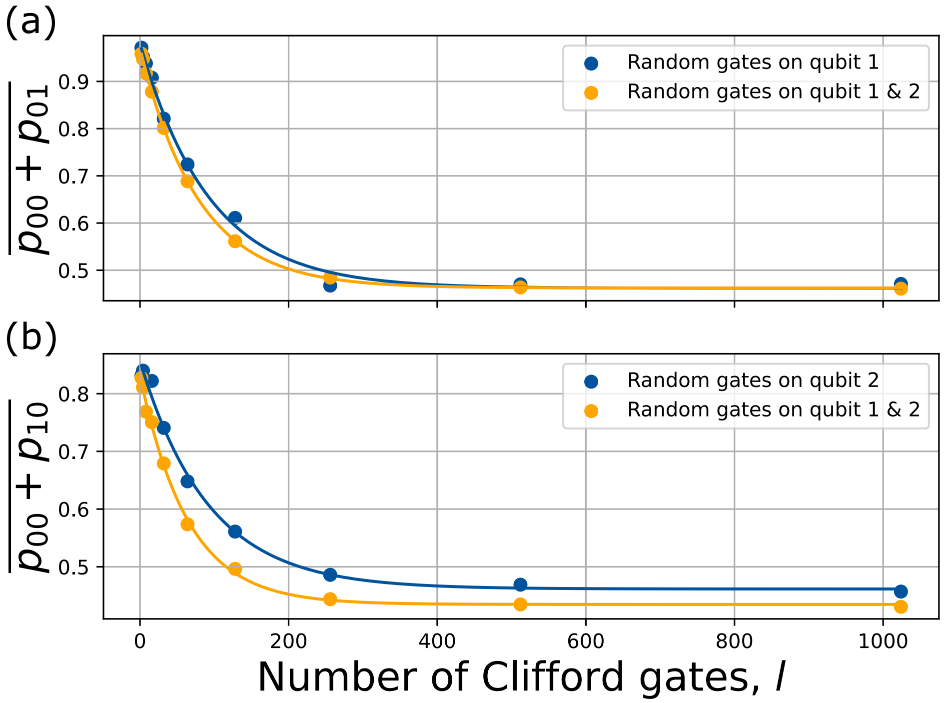

Figure 3.15: The result of the simultaneous randomised benchmarking experiment. (a) The success probability of the gate sequence ignoring the result of the second qubit of device 2Q1. (b) The success probability of the gate sequence ignoring the result of the first qubit of device 2Q1/Q1. For both cases, the success probability decays faster when random gates are applied simultaneously.

3.2.6 Summary

In this chapter, we have described a comprehensive series of characterisation and calibration experiments used to efficiently and accurately tune up a two-qubit device. The system identification and the gate tune-up routine complement each other in the sense that the system identification experiments use control electronics to identify the quantum device, and the gate tune-up routine uses the quantum device as a testbed to calibrate the control system accurately.

In summary, we overview the whole characterisation and calibration routine in Fig. 3.1. The system identification block is usually implemented right after mounting the sample, and we do not repeat it often. We then optimise the single-qubit gates and find the optimal pulse duration that achieves the maximum randomised benchmarking fidelity, indicated by a grey dashed loop in the gate tune-up routine block of Fig. 3.1. After we find the optimal pulse duration, we fix the pulse duration and execute the main experiment. During the main experiment, we repeat the gate tune-up loop inside the green area as much as run time allows to make the main result robust from the instrument drift, and monitor the system if there is a fatal failure during the measurement.

Chapter 4

Variational quantum algorithm using spin-echo techniques

Previously, we have introduced the physics of always-on coupled superconducting qubits and experimental methods to operate them for quantum information processing. In this chapter, we show a proof-of-principle quantum algorithm experiment using an always-on coupled two-qubit circuit. Here we introduce a novel hardware compilation of variational quantum eigensolver (VQE) algorithm and quantum error mitigation, using spin-echo sequence and the always-on interaction. The aim of this chapter is to show how the native interaction can be used to run a quantum algorithm by showing concrete example of actual pulse sequences used in experiments. We begin by explaining the basics of the VQE algorithm and listing important formulae used in later sections. We then show the experimental results of implementing the VQE algorithm and the quantum error mitigation using spin-echo sequence on an always-on coupled two-qubit device.

4.1 Variational Quantum Eigensolver (VQE)

The variational quantum eigensolver is a quantum-classical hybrid algorithm inspired by the variational method to simulate and find the ground state energy of a quantum many-body system. In contrast to the conventional approach of the variational method using classical computers, the VQE uses a quantum processor as a quantum data storage for the trial wave function and complements non-quantum tasks such as arithmetic and optimisation by a classical computer. The VQE has been implemented in various hardware platforms such as photonics [43], trapped-ions [80] and superconducting qubits [81] to simulate various molecules such as H_2, H_2O and H_{12}.

Along with the increase in the simulated molecule size, there have been extensive studies to make full use of noisy quantum hardware by taking realistic physical constraints and errors into account. For example, conventional two-qubit gates were replaced by hardware-efficient entanglers in the variational algorithm implementation to alleviate experimental complication [27]. In their work, they simply applied cross-resonant drive [25] to the system without cancelling unwanted terms, which allowed them to generate entanglement without needing to carefully calibrate two-qubit gates. To tackle unavoidable errors in qubits, the error mitigation technique has been invented [82, 83], and a proof-of-principle experiment has been demonstrated on superconducting qubits [84]. However, there are limitations to these methods as well. The trial wave function prepared by unstructured hardware efficient gates has difficulty in reaching the optimum due to the barren plateau in the energy landscape [31]. Also, the pulse rescaling technique applied to the error mitigation experiment in [84] requires careful calibration of two-qubit gates assuring linear scaling of errors to linear extension of pulse duration, which gives additional experimental constraint and cost.

To overcome these problems and implement hardware-efficient error-mitigated variational algorithms, we have proposed a novel hardware compilation scheme using always-on coupled device and spin-echo sequence. The spin-echo approach uses the native interaction in the hardware, but it is programmable by using dynamical decoupling techniques [35, 36], which will be further explained in Chapter 5. The aim of this chapter is to show a real-device application of the spin-echo compilation to the VQE and quantum error mitigation. In this section, we explain the theory of the VQE and the error mitigation using the actual algorithm used for simulating H_2 molecule. We then show the experimental result of the VQE implementation finding the ground state energy of the H_2 molecule in our two-qubit superconducting quantum processor in the next section.

4.1.1 VQE for H_2 molecule simulation

First, we need to prepare a trial wave function that maps the H_2 molecule Hamiltonian by a quantum processor. The trial wave function is parameterised by a reasonable guess depending on available parameters on the hardware. Here we parameterised the trial wave function according to the unitary coupled cluster theory [85, 86, 30] and formulated the trial wave function as follows,

$$|\psi(\theta)\rangle = \exp(-i\theta XY)\,|01\rangle\,, \tag{4.1}$$

where θ is a tunable parameter in a two-qubit system.

For a given trial wave function with chosen parameter θ, we calculate the total energy of the H_2 molecule. In the real space, the total energy depends on the bond distance between two hydrogen atoms d, but to compute the energy by a quantum processor, we need to map the original Hamiltonian to the qubit basis by multiple transformations [30], which in the end, acts only on two qubits. For the H_2 molecule simulation, the transformed Hamiltonian consists of one and two-body Pauli terms as follows,

$$\mathcal{H}(d) = g_0(d) + g_1(d)ZI + g_2(d)IZ + g_3(d)ZZ + g_4(d)XX + g_5(d)YY, \tag{4.2}$$

where $g_0(d), g_1(d), ..., g_5(d)$ contain the information of the H_2 molecule, and depend on the bond length between hydrogen atoms (see Appendix A.3). For each d, the cost function can be evaluated by obtaining the expectation value of the H_2 molecule Hamiltonian for a given trial wave function $|\psi(\theta)\rangle$,

$$E(\theta, d) = \langle \mathcal{H}(\theta, d)\rangle = \langle \psi(\theta)|\mathcal{H}(d)|\psi(\theta)\rangle\,. \tag{4.3}$$

Expectation values of Pauli terms $\langle ZI(\theta)\rangle$, $\langle IZ(\theta)\rangle$, $\langle ZZ(\theta)\rangle$, $\langle XX(\theta)\rangle$ and $\langle YY(\theta)\rangle$ in (4.3) are obtained by partial quantum state tomography of the trial wave function, and the total energy is calculated by a classical processor.

Lastly, the minimum energy for a given distance d can be found by searching the optimal θ in the parameter space,

$$\tilde{E}(d) = \min_{\theta} E(\theta, d). \tag{4.4}$$

In our experiments, we swept the whole parameter space $-\pi \leq \theta \leq \pi$ to find the minimum instead of implementing optimisation for each distance. The optimal bond distance is then obtained by choosing the bond distance d that gives the minimum energy,

$$E_{min} = \min_{d} \tilde{E}(d). \tag{4.5}$$

4.1.2 Quantum error mitigation by linear extrapolation

In realistic devices, quantum operations are not perfect due to various error sources. For example, qubits lose information by energy relaxation and decoherence as quantum circuit becomes deeper. Without quantum error correction, a quantum processor can not correct these errors, so the output of the quantum algorithm varies from the ideal result as accumulated error increases. However, some of the deviation from the ideal output can be corrected by post-processing using quantum error mitigation protocol [83, 82, 87, 84].

Here, we review the zero-noise extrapolation technique [83], which is one the most straightforward ways to implement quantum error mitigation. The main idea is to infer the ideal expectation value of a physical observable by additional measurements with different amount of errors. As shown in Fig. 4.1, let us suppose we measured the expectation value of one of the Pauli operators as $\langle \mathcal{P}(r) \rangle$, where r is the magnitude of error during the algorithm implementation. We then implement the same algorithm with added errors $r + \epsilon$ to obtain $\langle \mathcal{P}(r + \epsilon) \rangle$.

By extrapolating these data points, we can infer the ideal result $\langle \mathcal{P}^*(0) \rangle$ by the following formula [83],

$$\mathcal{P}(0) = \frac{(r+\epsilon)\mathcal{P}(r) - r\mathcal{P}(r+\epsilon)}{r + \epsilon - r}. \tag{4.6}$$

The linear extrapolation works when the error is small enough so that the effect of the higher order terms can be neglected in the extrapolation. In the next chapter, we use this formula for mitigating errors in the VQE experiment.

The standard error of the estimated expectation value is,

$$\Delta\mathcal{P}(0) = \frac{r^2 + (r+\epsilon)^2}{\epsilon^2}(\sigma^2(r) + \sigma^2(r+\epsilon)) \tag{4.7}$$

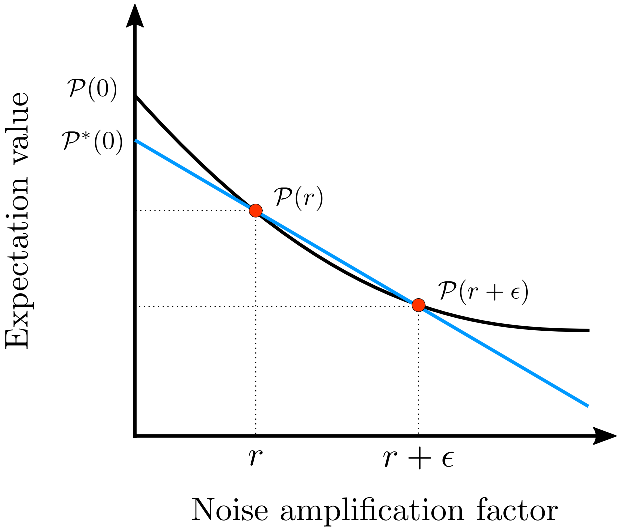

Figure 4.1: Schematic of the quantum error mitigation using zero-noise extrapolation. Black curve describes the decay of the expectation value $\mathcal{P}$ with respect to the amount of error. To estimate the expectation value in the ideal case $\mathcal{P}(0)$, we take multiple measurements with different noise amplification factors (red points) and extrapolate them to get $\mathcal{P}^*(0)$. If the error was small enough, the extrapolation can be done by linear fitting (blue line) [83].

where $\sigma^2(r)$ is the variance of the data point when the noise amplification factor is r.

4.2 Two-qubit VQE Experiment

In this section, we introduce the methodology of the VQE and quantum error mitigation experiment on always-on coupled superconducting quantum processors.

First, we briefly summarise the device characteristics of the superconducting qubit device used in the VQE experiment. We then introduce the spin-echo pulse sequence for generating the two-qubit trial wave function and how to modify the pulse sequence to implement the quantum error mitigation. Finally, we show the state tomography result of the trial wave function and the simulated ground state energy of the H_2 molecule.

4.2.1 Experimental configuration

The superconducting quantum processor for the VQE experiment consists of two transmon qubits are directly coupled by a capacitance arm. We have used the device 2Q1 (see Appendix A.1 for device details) for this experiment, and since the detuning between qubits are much larger than their coupling strength, $\Delta_{12} = \omega_{q_1} - \omega_{q_2} \gg J$, we assumed that the qubits are dispersively coupled and the system Hamiltonian can be described as follows,

$$\hat{\mathcal{H}}_{disp}/\hbar = -\frac{\omega_{q_1} + J^2/\Delta_{12} + \zeta/2}{2}\hat{Z}\hat{I} - \frac{\omega_{q_2} - J^2/\Delta_{12} + \zeta/2}{2}\hat{I}\hat{Z} + \frac{\zeta}{4}\hat{Z}\hat{Z}, \tag{4.8}$$

where $\zeta = -\frac{2J^2(\alpha_1+\alpha_2)}{(\Delta_{12}+\alpha_1)(\alpha_2-\Delta_{12})}$ is the strength of the residual ZZ coupling and α_1, α_2 are anharmonicities of the two qubits. The prefactor of each term in Eq. (4.8) is obtained by the two-qubit Ramsey experiment introduced in Sec. 3.1.5. This Hamiltonian is crucial for our experiments because we use the residual ZZ interaction to generate two-qubit entanglement in the trial wave function.

To implement spin-echo, qubit basis rotation and quantum state tomography, we generated single-qubit gates by sending microwave pulses to each qubit from individual control line. Pulse shaping is important for tuning the single-qubit gate at a specific rotation angle such as π or $\frac{\pi}{2}$, and we chose Blackman envelope for shaping single-qubit gate pulses. The qubit drive frequencies were set to minimise the single qubit terms in Eq. (4.8). Amplitude and DRAG coefficients of the pulses are calibrated by pulse train tune-up and cross-AllXY tune-up. For single-qubit gates in this

	$\omega_r/2\pi$	$\omega_q/2\pi$	α	T_1	T_2	$\zeta/2\pi$
Qubit 1	10.54 GHz	6.58 GHz	-299 MHz	26.2 μs	21.9 μs	-0.94 MHz
Qubit 2	9.50 GHz	6.05 GHz	-310 MHz	19.1 μs	25.6 μs	

Table 4.1: Physical parameters of device 2Q1 used for the main VQE experiment.

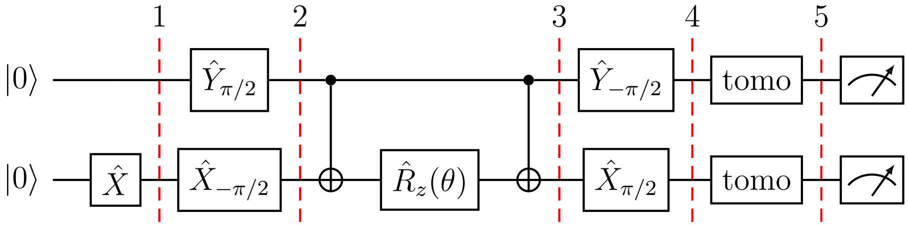

Figure 4.2: A step-by-step break down of generating the trial wave function for the VQE estimating the ground state energy of the H_2 molecule. (1) Initialising the trial wave function to $|01\rangle$, (2) transforming the basis of the quantum state to x-basis and y-basis, (3) gate-based compilation of $ZZ(\theta)$, (4) restoring the state to the computational basis and (5) pulse for quantum state tomography.

experiment, we chose a relatively long time duration of 110 ns to minimise the effect of the leakage.

4.2.2 Spin-echo sequence for preparing the trial wave function

In the H_2 molecule simulation, the trial wave function (4.1) is prepared by applying a unitary operation $\hat{U}(\theta) = \exp\left(-i\theta\hat{X}\hat{Y}\right)$ to the initial state $|01\rangle$. For example, in the gate-based approach, the unitary transformation can be compiled to one and two qubit gates. The conventional 2-qubit VQE algorithm is shown in Fig. 4.2 [30, 84]. The basis state $|01\rangle$ is first prepared at slice 1. Then the unitary evolution $\hat{U}(\theta) = \exp\left(-i\theta\hat{X}\hat{Y}\right)$ is completed at slice 4 and tomography pulses are applied in the end. The unitary operation between slice 2 and 3 can be any physical implementation as long as arbitrary $ZZ(\theta)$ rotation can be realised. One way, as described above, is to compile the $ZZ(\theta)$ rotation to two CNOT gates and single-qubit $Z(\theta)$ rotation. For example, a CNOT gate can be realised by the cross-resonant interaction [25], which has been implemented to run VQE algorithms on superconducting circuits [84].

In our approach, we replace the $ZZ(\theta)$ operation between slice 2 and 3 by free-

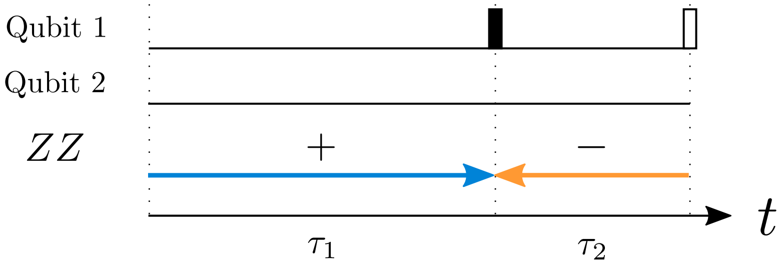

Figure 4.3: Schematic of the spin-echo sequence of generating arbitrary $ZZ(\theta)$ rotation by $\hat{\mathcal{H}}/\hbar = \frac{\zeta}{4}\hat{Z}\hat{Z}$. Spin-echo pulses are described as rectangles (black: $\hat{X}_\pi$ and white: $\hat{X}_\pi^\dagger$) and the sign of the phase accumulated by ZZ interaction is depicted as arrows (blue: positive, orange: negative). The timing of the black spin-echo pulse determines τ_1 and τ_2, which controls the total phase accumulation $ZZ(\frac{\zeta(\tau_1-\tau_2)}{4})$.

evolution of the native Hamiltonian and spin-echo pulses. For example, suppose we have the native Hamiltonian of $\hat{\mathcal{H}}/\hbar = \frac{\zeta}{4}\ \hat{Z}\hat{Z}$, we construct the pulse sequence as Fig. 4.3 to parameterise the $ZZ(\theta)$ rotation. In this pulse sequence, the whole time-evolution is separated by two time periods τ_1 and τ_2. The first time period is just a free-evolution accumulating the positive phase $ZZ(\frac{\zeta\tau_1}{4})$. In the second period, the negative phase is accumulated by applying spin-echo pulses [33],

$$(\hat{X}_\pi^\dagger\hat{X}_\pi^\dagger)\hat{U}(\frac{\tau_2}{2})(\hat{X}_\pi\hat{X}_\pi) \quad = \quad \exp\left(-\frac{i\tau_2}{2\hbar}(\frac{\zeta}{4}\hat{Z}\hat{Z})\right). \tag{4.9}$$

The arbitrary ZZ rotation is realised by choosing the timing of the first pulse, which determines the angle $\theta = \frac{\zeta(\tau_1-\tau_2)}{4}$. Here, we set the total dutation $T = \tau_1 + \tau_2$ to be constant such that the incoherent error during the time-evolution becomes the same for different $ZZ(\theta)$. Although the most obvious way to generate $ZZ(\theta)$ is to let the system evolve for time t and define the angle as $\theta = \zeta t$, it is better to fix the total time duration when we need to fix the amount of incoherent error for different rotation angle, which is crucial in error mitigation experiments.

In the real device, we need to assume single-qubit detuning terms in the native Hamiltonian since we observe finite detunings due to non-idealities of the microwave drive. In the drive frame of both qubits, we model our native Hamiltonian as,

$$\hat{\mathcal{H}}/\hbar = -\frac{\omega_{q_1'} - \omega_{d_1}}{2}\hat{Z}\hat{I} - \frac{\omega_{q_2'} - \omega_{d_2}}{2}\hat{I}\hat{Z} + \frac{\zeta}{4}\hat{Z}\hat{Z} \tag{4.10}$$

$$= -\frac{\delta_1}{2}\hat{Z}\hat{I} - \frac{\delta_2}{2}\hat{I}\hat{Z} + \frac{\zeta}{4}\hat{Z}\hat{Z}, \tag{4.11}$$

where $\omega_{q_1'}, \omega_{q_2'}$ are resonant frequencies of both qubits in the computational bases (4.8), $\omega_{d_1}, \omega_{d_2}$ are drive frequencies of the qubit controls and ζ is the coupling strength of the residual ZZ coupling. Typically, the residual ZZ coupling is regarded as a source of coherent error, but we make use of this interaction as a computational resource for the VQE algorithm.

To generate arbitrary $ZZ(\theta)$ from the native Hamiltonian with three terms, we add more spin-echo pulses to control the phases of all terms as shown in Fig. 4.4.

Here, we introduce four time periods separated by spin-echo pulses. Sign of each term in a particular time period is determined by the commutation relation between

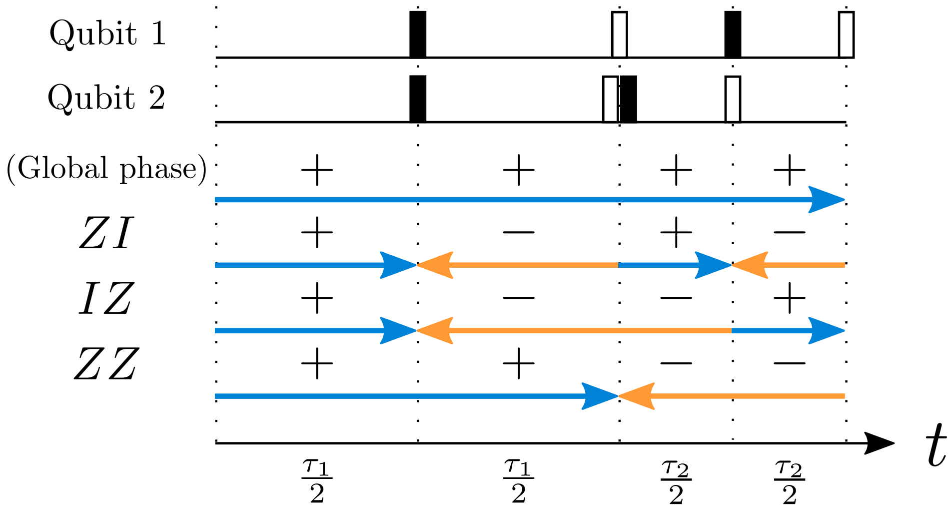

Figure 4.4: Schematic of the spin-echo sequence of generating arbitrary $ZZ(\theta)$ rotation on a realistic system Hamiltonian $\hat{\mathcal{H}}/\hbar = -\frac{\delta_1}{2}\hat{Z}\hat{I} - \frac{\delta_2}{2}\hat{I}\hat{Z} + \frac{\zeta}{4}\hat{Z}\hat{Z}$. Single-qubit terms have negative signs during the time period sandwiched by $\hat{X}_\pi$ (black) and $\hat{X}_\pi^\dagger$ (white). Two adjacent $\hat{X}_\pi$ and $\hat{X}_\pi^\dagger$ pulses on the second qubit in the middle are effectively an Identity operator, so we omit them in the actual experiments.

the static term and the spin-echo pulses in the period. For example, in the second period, signs of $\hat{Z}\hat{I}$ and $\hat{I}\hat{Z}$ are negated by sandwiching the free evolution of time $\frac{\tau_1}{2}$ between two simultaneous $\hat{X}_\pi$ gates,

$$(\hat{X}_\pi^\dagger \hat{X}_\pi^\dagger)\hat{U}(\frac{\tau_1}{2})(\hat{X}_\pi \hat{X}_\pi) \quad = \quad \exp\Bigg(-\frac{i\tau_1}{2\hbar}(\frac{\delta_1}{2}\hat{Z}\hat{I} + \frac{\delta_2}{2}\hat{I}\hat{Z} + \frac{\zeta}{4}\hat{Z}\hat{Z})\Bigg). \tag{4.12}$$

Here, $\hat{X}_\pi \hat{X}_\pi$ means a simultaneous application of single-qubit $\hat{X}_\pi$ gates and doesn't indicate two-qubit operation. In general, sign flips of the free-evolution between spin-echo pulses are determined by the commutation relations $[\hat{Z}\hat{I}, \hat{X}_\pi \hat{X}_\pi] \neq 0$, $[\hat{I}\hat{Z}, \hat{X}_\pi \hat{X}_\pi] \neq 0$ and $[\hat{Z}\hat{Z}, \hat{X}_\pi \hat{X}_\pi] = 0$. As long as these commutation relations are guaranteed, the spin-echo pulses can be either $\hat{X}_\pi$ gate or $\hat{Y}_\pi$ gate.

The timings of the three sets of spin-echo pulses have different purposes. The first simultaneous $\hat{X}_\pi$ gates echo out one-body terms by making the first and the second time periods to be the same. The second simultaneous gates also cancel one-body terms in the third and the fourth time periods. With these simultaneous spin-echo pulses, one-body terms accumulate no phase during entire time duration even if there are unexpected detunings. Lastly, the phase of the ZZ interaction accumulates $\zeta\tau_1$ in the first and the second periods and $-\zeta\tau_2$ in the third and the fourth periods. The timing of the middle pulse acts as a tuning knob for determining the rotation angle $\theta = \frac{\zeta}{4}(\tau_1 - \tau_2)$ of the ZZ interaction.

4.2.3 Algorithm implementation and tomography results

In the real experiments, the actual pulse sequence sent to the two-qubit device is as follows and the always-on ZZ interaction is described as a purple shade instead of discrete single-qubit gates.

Some of the single-qubit gates in the original circuit (4.2.2) are joined together

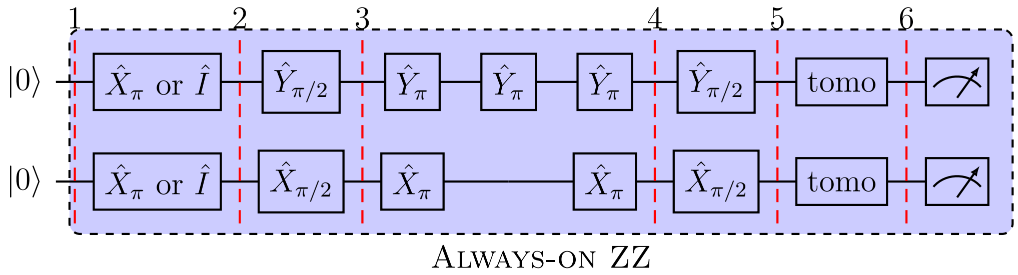

Figure 4.5: Pulse sequence of preparing the trial wave function for H_2 molecule simulation. Although there is no explicit connection between qubits in the circuit diagram, we assume that there is an always-on interaction throughout the algorithm implementation (purple shade). Timings of the pulses in this diagram are not representing the experiment, especially the timing of pulses between slice 3 and slice 4 vary significantly depending on the rotation angle of $ZZ(\theta)$.

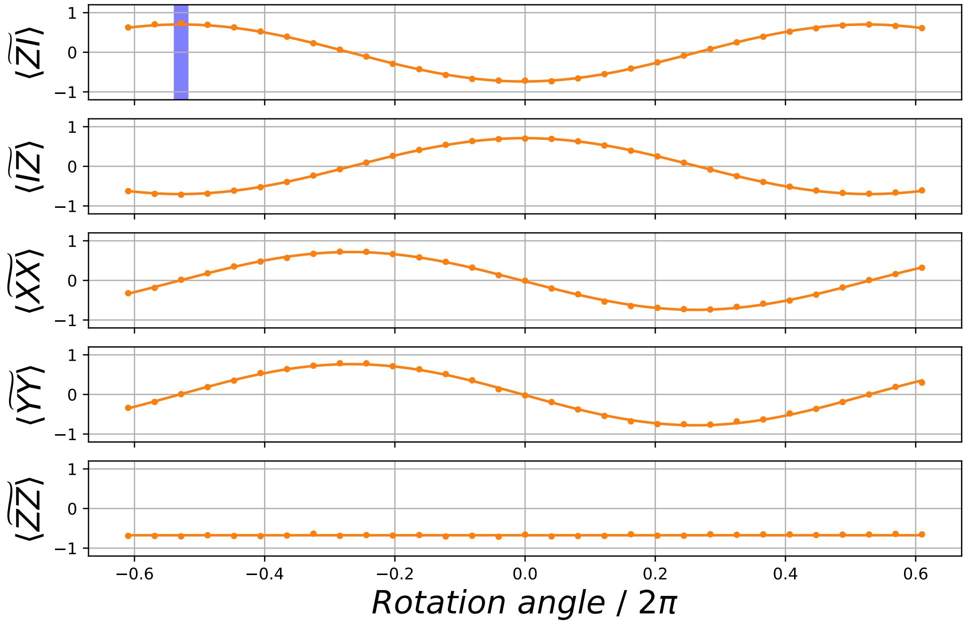

Figure 4.6: Partial quantum state tomography result of the trial wave function $|\psi(\theta)\rangle = \exp\left(-i\theta\hat{X}\hat{Y}\right)|01\rangle$ swept by the variational parameter $\theta = \frac{\zeta}{4}(\tau_1 - \tau_2)$. The data points are fitted by cosine and sine curves for $\langle\widetilde{ZI}\rangle$, $\langle\widetilde{IZ}\rangle$, $\langle\widetilde{XX}\rangle$, $\langle\widetilde{YY}\rangle$, and a horizontal line for $\langle\widetilde{ZZ}\rangle$.

to reduce the total pulse count. The timing of each gate is not indicated in the quantum circuit, but the timings of pulses between slice 3 and 4 are varied according to Fig. 4.4. The arbitrary $ZZ(\theta)$ rotation is parameterised by $\theta = \frac{\zeta}{4}(\tau_1 - \tau_2)$ and the total duration $T = \tau_1 + \tau_2$ is fixed so that the accumulated incoherent errors will be the same for all θ. To symmetrise the effect of the measurement bias depending on the initial state, we average four different algorithm runs initialised in $|00\rangle$, $|01\rangle$, $|10\rangle$ or $|11\rangle$ by applying $\hat{X}_\pi$ or $\hat{I}$ gate between slice 1 and 2.

Fig. 4.6 shows the partial state tomography result of the trial wave function swept by θ. Each point in the graph is averaged by 2.8 million shots and the error bar on each point corresponds to the standard deviation. We used this data set to estimate how well this protocol finds the ground state energy of H_2 molecule.

4.2.4 Spin-echo sequence for the quantum error mitigation

To mitigate the error on the experimental result caused by decoherence, we applied the error mitigation technique [83] for always-on two-qubit interaction. In the previous study [84], the error mitigation was applied to two-qubit gates that were generated by cross-resonance interaction, which was shaped by microwave pulses. The error mitigation for cross resonance gates was implemented by stretching the pulse duration to simulate different noise accumulation due to decoherence. However, the time rescaling approach for the pulsed two-qubit gates required the gate to be re-calibrated for different pulse duration, which is resource intensive [88].

In our study, we introduced a novel time rescaling technique that doesn't require additional calibration for two-qubit interaction. The time rescaling method is implemented by simply extending the total duration using the same spin-echo sequence. Sign patterns of four time periods remain the same, but the time duration of each period is modified such that (1) $ZZ(\theta)$ accumulate the same phase as the original

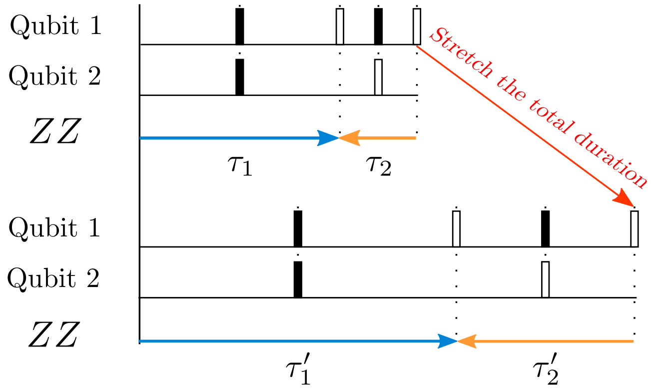

Figure 4.7: Schematic of the spin-echo sequence for implementing the error mitigation. The total time duration $T = \tau_1 + \tau_2$ is stretched to $T' = \tau_1' + \tau_2'$, but the difference is fixed by setting $\tau_1 - \tau_2 = \tau_1' - \tau_2'$. By doing so, the trial wave function undergoes the same unitary evolution, but accumulates different incoherent errors. In the following, we define the error amplification factor as the ratio between T and T'.

pulse sequence and (2) single qubit terms are echoed out. This way, since the always-on interaction is constant, we can prepare the same trial wave function with different noise amplification factor without extra calibration for the two-qubit operation.

We ran the VQE algorithm with two different total durations, $T'_{(1,2)} = 2850(4930)$ ns. Here, we focused on rescaling the duration of the always-on entangling operation and did not rescale duration of single-qubit gates, so coherent errors during single-qubit gates were not corrected by the error mitigation technique. The noise amplification factors, $r = 1$ and 1.76, are calculated by dividing each total duration $T'_{(1,2)} = 2850(4930)$ ns by $T = 2850$ ns which is the duration of the original pulse sequence without extension. Fig. 4.8 shows the expectation value of ZI with respect to the noise amplification factor, when the trial wave function was set to $\theta = -1.056\ \pi$.

Fig. 4.9 shows the tomography result over the parameter space of $-1.22\ \pi \leq \theta \leq 1.22\ \pi$ with different noise amplification factors $r = 1$ and 1.76. As we see from the plot, the amplitude of the oscillation gets smaller as the noise amplification factor increases.

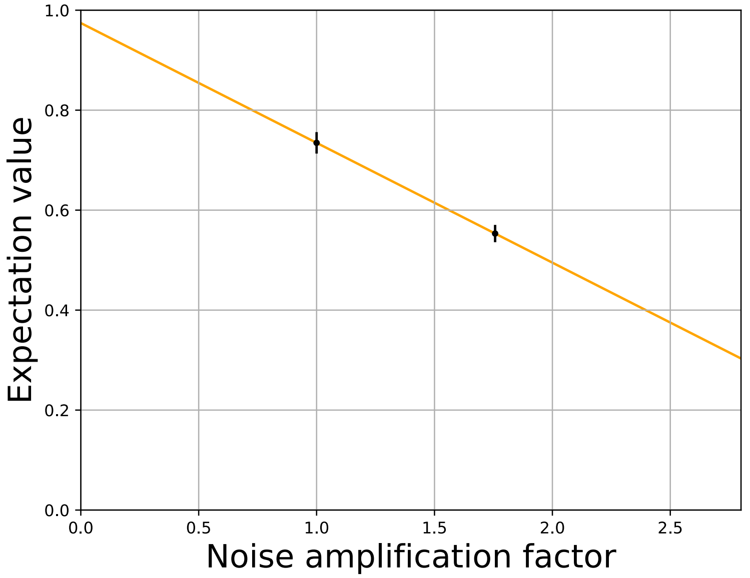

Figure 4.8: Demonstration of the error mitigation protocol by spin-echo sequences. This figure is the experimental realisation of Fig. 4.7 in the theory section. The noise amplification factor is defined as the ratio between the time duration of the original algorithm time-evolution T and the stretched time duration T'. Data points in the graph describe the expectation value $\langle \widetilde{ZI} \rangle$ of the trial wave function prepared at $\theta = -1.056\,\pi$ (points in the shaded area of Fig. 4.9) with different noise amplification factors. The error mitigation is applied by fitting the smallest two points with a linear line and extrapolating the expectation value to the point where the noise amplification factor is 0.

4.2.5 Finding the minimum energy of H_2 molecule

To estimate the minimum bond energy of the H_2 molecule, we first calculate the total energy $E(\theta, d)$ according to equation (4.3) using the tomography results. Here, instead of implementing the quantum-classical optimisation loop, we searched the minimum from the available data sets. This allowed us to estimate the performance our protocol with less experimental runs when we had limited signal to noise ratio.

Since the coefficients $g_i (i = 1, 2, 3, 4, 5)$ depend on the bond distance d, for each distance d, we optimised θ to get the minimum energy $\tilde{E}(d) = \min_{\theta} E(\theta, d)$. We then plot the minimum $\tilde{E}(d)$ for each d on a bond distance vs. total energy curve.

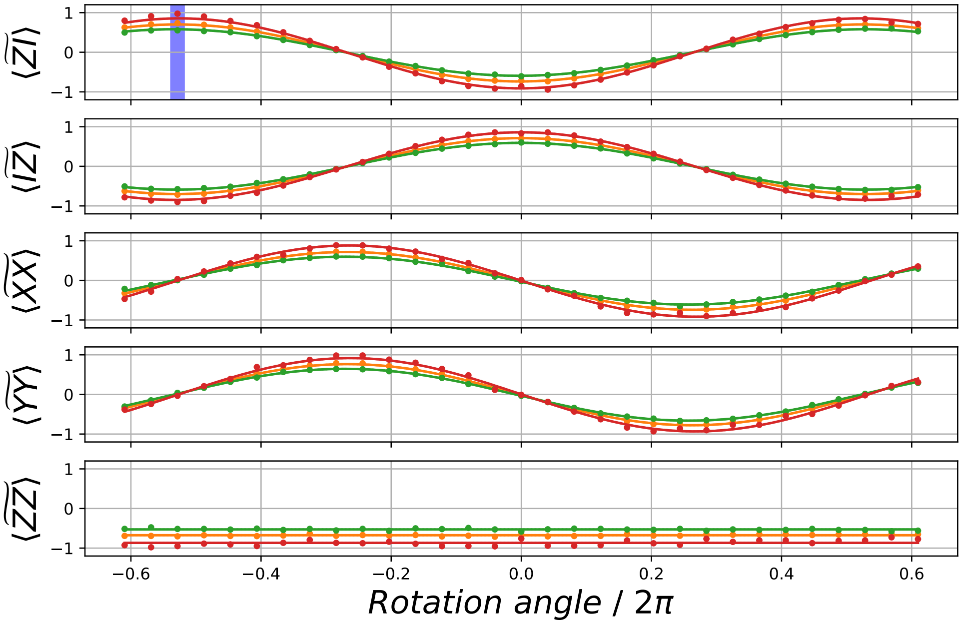

Figure 4.9: Measured Pauli operators for the VQE experiment with error mitigation. Different colours correspond to different error amplification factors $r = 1$ (orange), 1.76 (green) and the extrapolated points (red). Points in the shaded area ($\theta = -1.056\ \pi$) are plotted in Fig. 4.8.

The optimised total energy of the trial wave function prepared by the original pulse sequence (orange points) and extended pulse sequence (green points) are far above the theory prediction and we don't see a clear dip to find the minimum energy as shown in Fig. 4.10. However, the error mitigated result could find the energy curve much closer to the theory curve which has a clear dip.

The difference between the extrapolated points and the theory curve can be explained by the following reasons. First, our error mitigation technique doesn't remove coherent errors on the single-qubit gate. Although we calibrate single-qubit gates carefully, there are finite control errors such as over or under rotation and leakage errors. To decrease the effect of the leakage error, we have chosen a relatively long pulse which is 110 ns long. However, such a long pulse was prone to coherent errors

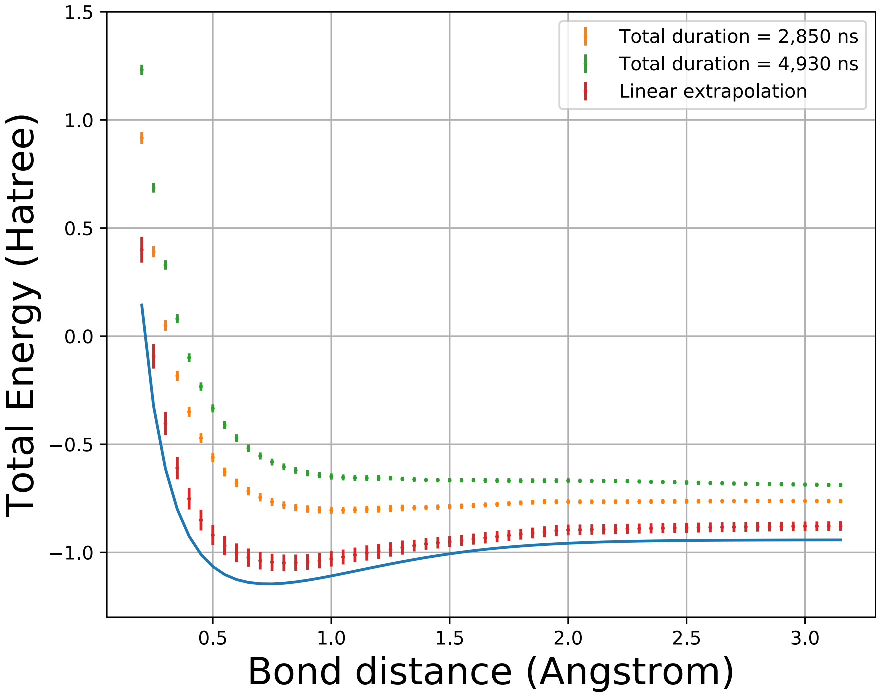

Figure 4.10: Experimental results and error mitigated results of the ground state energy of the H_2 molecule. Yellow and green points are optimised total energies when error amplification factor was $r = 1, 1.76$. Error mitigated results (red) are calculated by Pauli operator expectation values that are linearly extrapolated by Pauli operator expectation values that produced yellow and green points.

due to the always-on ZZ interaction, and we weren't able to get rid of it in this study. This could be improved in the future by investigating single-qubit gates which are not susceptible to the always-on interaction, such as using numerically optimised gates [74, 89]. Second, the incoherent error was not removed completely by the error mitigation. The amount of errors that can be removed by the time rescaling method depends on how fast the algorithm is operated compared to the time scale of T_1 and T_2 time. In a different experimental run, we have measured the decay rate of the amplitude of the fitting curves for the expectation values of $\langle\widetilde{ZI}\rangle$, $\langle\widetilde{IZ}\rangle$, $\langle\widetilde{XX}\rangle$, $\langle\widetilde{YY}\rangle$ and $\langle\widetilde{ZZ}\rangle$. The decay rate was 10 μs where the total duration of the algorithm were $T = 2850$ and 4930 ns, and this relatively small ratio limits the amount of errors that the linear extrapolation can mitigate. To overcome this limit, we need to have faster always-on interaction and longer T_1 and T_2 in future devices, and we will discuss how much we can extend in this direction in Chapter 6.

Chapter 5

Hamiltonian rescaling using spin-echo sequence

In the previous chapter, we have utilised the native interaction to implement arbitrary ZZ rotation and parameterised the accumulated phase by timing of spin-echo pulses. This chapter generalises the spin-echo-based algorithm compilation to many qubits, formalising the Hamiltonian rescaling protocol using the always-on interaction and multi-qubit spin-echo sequences.

First, we begin with a small-scale example and overview the problem we encounter when we extend the spin-echo-based compilation to an arbitrary number of qubits. To tackle the complexity in many qubits, we formalise the multi-qubit spin-echo problem in general, giving a theoretical background for the Hamiltonian rescaling method in later sections. We then introduce the application of the multi-qubit spin-echo theory to generate pulse sequences for rescaling Hamiltonians of two different coupling patterns; the all-to-all coupling and the nearest-neighbour coupling. We have introduced two pulse sequence generation algorithms to produce concrete spin-echo sequences for each case, also estimating the total time duration and the pulse count needed for the general implementation. We show a favourable scaling of the resources to the number of qubits, which is crucial for showing the viability of our approach using the native interaction for quantum computing. These results are also important for one of our motivations in this thesis, which is to reduce the quantum operation's duty cycle. Lastly, we discuss the practicality of each method and give an outlook for future application.

The content of this chapter is an extended version of the published articles [35, 36]. The author of this thesis has contributed to these works in identifying the efficient spin-echo strategy for Hamiltonian rescaling, clarifying the problem of the protocol and formulating the research question, leading the collaborators to solve the problem.

5.1 Motivation and research question

In the previous chapter, we have introduced a novel hardware implementation strategy for quantum-classical hybrid algorithms using spin-echo sequences. In the two-qubit example, we have introduced a scheme to generate an arbitrary $ZZ(\theta)$ by tuning the timing of a spin-echo pulse to set the rotation angle θ. From a different perspective, this is equivalent to rescaling the native Hamiltonian to a desired effective Hamiltonian by choosing the timing of a spin-echo pulse. Having the ability to cover the full parameter space of a two-qubit operation by timing a spin-echo pulse, a natural question arises: can we extend the scheme to rescale any native many-qubit Hamiltonian to a desired effective Hamiltonian by timing multiple spin-echo pulses? This is the main topic of this chapter and the question led to opening a new paradigm of compiling quantum algorithms on a hardware.

In the following, we begin with introducing the conventional approach taken in the NMR community to tackle this problem, and discuss the limitation and rooms for the improvement. We then introduce our strategy to tackling this problem and clarify my contribution to the works presented in [35, 36]. We then introduce concrete algorithms of finding pulse sequences for Hamiltonian rescaling in Sec. 5.4 and 5.5, which are condensed versions of [35, 36]. Lastly, we review the advantages of our approach compared to previous works and discuss the implication to a wider context of quantum computing.

5.2 Hamiltonian rescaling by conventional NMR techniques

The hardware compilation of quantum algorithms on an always-on Ising coupling has been investigated intensively in the NMR community [63, 64]. To cancel unwanted always-on couplings and retain desired interaction, spin-echo techniques were developed to decouple and recouple specific interactions in the Ising coupled system. Spin-echo sequences were used to implement various quantum algorithms in NMR systems [90, 91, 92] and our schemes are built on top of their development. Here we review the basic concept of spin-echoes and how it was applied to compile quantum algorithms.

5.2.1 Spin-echoes

The background Hamiltonian of an NMR spin system consists of one-qubit interactions (resonance offsets) and two-qubit interactions (J-couplings). Consider a system of q qubits where the i^{th} qubit has a resonance offset Ω_i and the pair of qubits i and j have a J-coupling frequency ω_{ij}. The Hamiltonian for this system in the weak coupling limit is,

$$\hat{\mathcal{H}}/\hbar = \sum_i \frac{\Omega_i}{2}\hat{Z}_i + \sum_{i<j}\frac{\omega_{ij}}{4}\hat{Z}_i\hat{Z}_j. \tag{5.1}$$

In practice some of these interactions could either be zero or set to zero, allowing them to be dropped. For example, working in a suitable rotating frame allows some of the one-qubit interactions to be set to zero, while many two-qubit interactions can be negligible in partially coupled qubit systems. However, for generality and completeness, we shall initially consider fully coupled systems with q non-zero one-qubit interactions and $p = q(q-1)/2$ non-zero two-qubit interactions between the p pairs of qubits.

During a period τ of free evolution each qubit evolves under all the $q+p$ interactions, given by the propagator $\hat{U}(t) = \exp\left(-\frac{\mathrm{i}\hat{\mathcal{H}}\tau}{\hbar}\right)$. Since this Hamiltonian is diagonal in the chosen z-basis, all terms in the Hamiltonian commute, and the one-qubit and two-qubit evolutions can be summarised by the acquired phases

$$\Phi_i = \Omega_i\tau, \quad \phi_{ij} = \omega_{ij}\tau. \tag{5.2}$$

To sculpt the effective Hamiltonian into the desired form it is necessary to isolate the qubit interactions which we want while suppressing the unwanted interactions. This essentially requires controlling the evolution of the qubits such that the unwanted interactions finally acquire a phase of zero while letting the required interactions evolve to reach the desired values.

A spin-echo is a period of free evolution interrupted by π rotations in the middle of the evolution period. The notation π^i is used to denote a pulse which causes a 180 degree rotation on qubit i, about the x-axis unless otherwise stated. The effect of a pair of π^i rotations is to negate the effective frequency Ω_i of the qubit for the time period between the two pulses. Thus, the sequence $\tau\,\pi^i\,\tau\,\pi^i$, where time periods indicate free evolution under the internal Hamiltonian, will refocus the offset Ω_i as the phase Φ_i acquired during the first period of evolution gets nullified by the phase $-\Phi_i$ acquired in the second half.

Clearly, the one-qubit interaction of any given qubit i is only affected by π rotations applied to qubit i, and so individual interactions can be controlled independently. However, for two-qubit interactions, a π rotation applied to either qubit i or j reverses the frequency ω_{ij} while a simultaneous π rotation applied on both qubit i and j leaves ω_{ij} unchanged. A sequence $\tau\,\pi^i\,\tau\,\pi^i$ will thus refocus Ω_i and ω_{ij}, whereas a sequence $\tau\,\pi^{i,j}\,\tau\,\pi^{i,j}$ will refocus both Ω_i and Ω_j but not ω_{ij}. In this manner, the two-qubit interactions can be controlled, but this control cannot be achieved independently from one-qubit interactions.

A general spin-echo sequence comprises a series of free evolution time periods τ_m, sometimes called delays, separated by π pulses applied to one or more qubit. As long as the total number of π pulses applied to a given qubit is even the overall evolution can still be summarised by a set of phases, but now

$$\Phi_i = \Omega_i \sum_m S^i_m \tau_m, \quad \phi_{ij} = \omega_{ij} \sum_m S^i_m S^j_m \tau_m, \tag{5.3}$$

where S is a sign matrix, containing only the elements ± 1, with a sign change whenever a π pulse is applied to qubit i. For convenience we will also refer to the two-qubit sign matrix $S^{ij}_m = S^i_m S^j_m$, although this is obviously not independent from the one-qubit matrix. The complete sign matrix can be obtained by combining the one- and two-qubit matrices.

5.2.2 Refocusing

Methods for removing all the interactions (sometimes called decoupling), or for isolating one single interaction while refocusing everything else, have been widely studied. The most effective methods to achieve this rely on choosing sign matrices whose rows are taken from Walsh–Hadamard matrices [63, 64], so that each row is a Walsh function [93]. These matrices differ from other Hadamard matrices in that they are only defined for dimensions equal to a power of 2, the rows are not normalised, and the ordering of the rows is different.

A Walsh function W_n is defined by a vector with length equal to a power of 2 and with all the entries equal to ± 1. For W_0 all the entries are $+1$, while for every other W_n half the entries are $+1$ and half are -1, with the entries arranged such that there are n regularly spaced sign changes along the vector. For example the 4 by 4 Walsh–Hadamard matrix contains the four rows

$$\begin{pmatrix} W_0 \\ W_1 \\ W_2 \\ W_3 \end{pmatrix} = \begin{pmatrix} +1 & +1 & +1 & +1 \\ +1 & +1 & -1 & -1 \\ +1 & -1 & -1 & +1 \\ +1 & -1 & +1 & -1 \end{pmatrix}. \tag{5.4}$$

Strictly the name of the Walsh function must specify the number of columns as well as the number of sign changes, but this is left implicit here: the number of columns is equal to the smallest power of 2 larger than the highest Walsh number considered.

In a system of three qubit it is possible to remove all three one-qubit and all three two-qubit interactions by using four equal time periods τ and a sign matrix obtained by choosing $S^i = W_i$, avoiding W_0. This relies on two key properties of Walsh functions. Firstly all Walsh functions except W_0 contain an equal number of ± 1 values, and so all one-qubit interactions will be refocused when equal length time periods are used. Secondly the product of two Walsh functions is itself a Walsh function [93], defined by

$$W_p \circ W_q = W_{p \oplus q} \tag{5.5}$$

where $\circ$ indicates element wise multiplication, sometimes called the Schur product [94], and $\oplus$ indicates bitwise addition modulo two. Thus all two-qubit interactions will also be refocused.

A decoupling network is easily modified [63, 64] to retain a single interaction: to retain a one-qubit interaction Ω_i use $S_i = W_0$ for this qubit, while to retain a coupling ω_{ij} set $S_i = S_j$ so that $S_{ij} = W_0$ (see Fig. 5.1). To take a concrete example the coupling ω_{12} can be isolated in a three qubit system by choosing $S_1 = S_2 = W_1$ and $S_3 = W_2$. The π pulses required can be deduced by applying a pulse to a qubit whenever the corresponding row of S changes sign, including a final π pulse if the S row ends in -1, giving the sequence

$$\tau\, \pi^3\, \tau\, \pi^{1,2}\, \tau\, \pi^3\, \tau\, \pi^{1,2}. \tag{5.6}$$

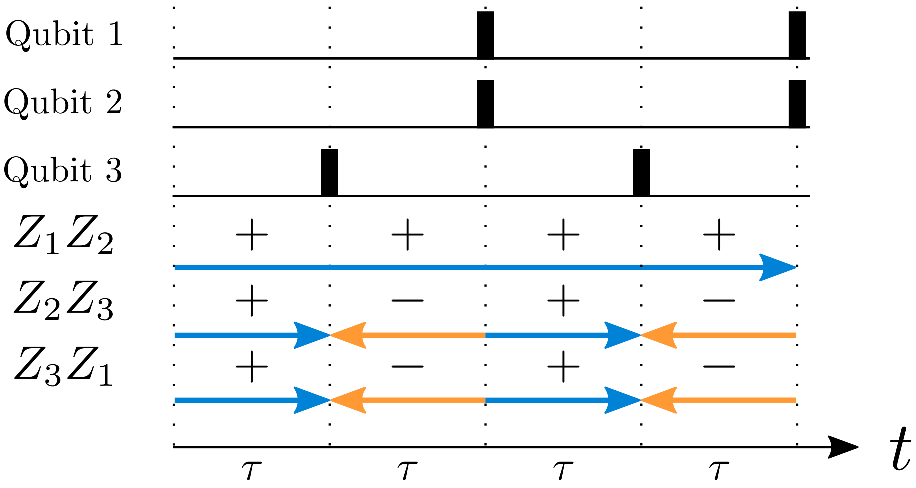

Figure 5.1: A pulse sequence that retains a single interaction in all-to-all coupled three qubits.

Note that ω_{12} evolves with sign $+1$ at every stage, and so is retained at full strength. The total evolution time required is given by $4\tau = \phi_{12}/\omega_{12}$. If this expression gives a negative time then this can be resolved by applying additional π pulses to one qubit at the beginning and end of the sequence to negate the evolution frequency.

Now consider how this approach scales to a system of q qubits. Retaining a single interaction can be done efficiently: the number of time periods required is given by the smallest power of 2 larger than q, which is upper bounded by $2q$, while the number of individual π pulses required is clearly less than $2q^2$, which corresponds to applying a pulse to every qubit after every time period. A more careful analysis (see Appendix A.4) shows that only around $q^2/2$ pulses are required, which is still $O(q^2)$ but with a smaller pre-factor. As the single interaction is retained at full strength this is also a minimum time solution.

5.2.3 Resources for Hamiltonian rescaling

So far, we have only considered retaining a single one-qubit or two-qubit interaction while refocusing the remainder. However, a more general problem is to *rescale* the size of interactions in the Hamiltonian. In other words, we desire to achieve a certain set of non-zero target phases for *all* the qubit interactions. The obvious approach is just to place spin-echo sequences which isolate the individual interactions back to back [63, 64]. As there are a total of $r = q+p = q(q+1)/2$ single-qubit and two-qubit interactions to be considered it is clear that the number of time periods is $O(q^3)$, and the number of pulses is $O(q^4)$. The total time required is given by the sum of the times required to evolve under each individual interaction,

$$T = \sum_i \left|\frac{\Phi_i}{\Omega_i}\right| + \sum_{i<j} \left|\frac{\phi_{ij}}{\omega_{ij}}\right| . \tag{5.7}$$

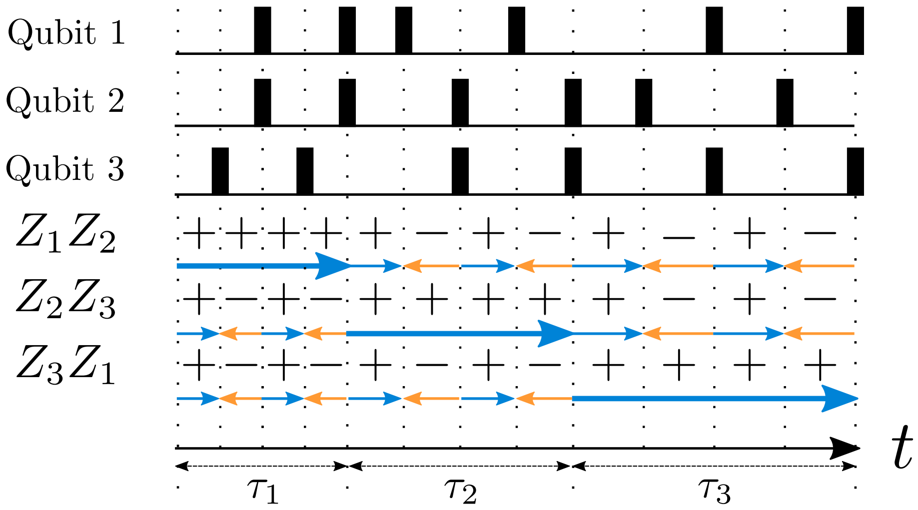

Figure 5.2: A pulse sequence that rescales all interactions in all-to-all coupled three qubits.

For example, if we want to rescale a three-qubit Hamiltonian, we prepare a pulse sequence shown in Fig. 5.2 which has 12 time periods and 18 pulses to obtain some target phases $\phi_{12} = \tau_1\omega_{12}$, $\phi_{23} = \tau_2\omega_{23}$ and $\phi_{31} = \tau_3\omega_{31}$.

This naive approach is expensive, both in time and the number of π pulses. We thus want to find a more efficient sequence, by carrying out as many evolutions in parallel as far as possible. Although this might sound challenging, we propose here a straightforward way to achieve this using partial refocusing pulse sequences. This approach also greatly reduces the number of pulses and time periods required.

5.3 Hardware-efficient Hamiltonian rescaling using spin-echo sequence

In the conventional NMR, most couplings were decoupled to retain one of the two-qubit interactions. This approach is inefficient since it consumes many spin-echo pulses while wasting most of the two-qubit evolution in each step. Also, the number of pulses per time period and total duration increases as the system size gets larger, making it much harder to implement in many qubits. To minimise the resource needed for the Hamiltonian rescaling, we have proposed a protocol to design pulse sequences that utilise as many couplings as possible without completely decoupling them in each step.

5.3.1 Considering the degrees of freedom in the Hamiltonian rescaling

To design a hardware-efficient pulse sequence, we have focused on the number of degrees of freedom needed to specify target angles independently. For example, when we want to specify $q(q-1)/2$ target phases, we should only need $q(q-1)/2$ time periods separated by spin-echo pulses to rescale two-qubit interactions. Let us consider this problem by a three-qubit example. Suppose all qubits are coupled to each other with coupling strengths ω_{12}, ω_{23} and ω_{31},

$$\hat{\mathcal{H}}/\hbar = \frac{\omega_{12}}{4}\hat{Z}_1\hat{Z}_2 + \frac{\omega_{23}}{4}\hat{Z}_2\hat{Z}_3 + \frac{\omega_{31}}{4}\hat{Z}_3\hat{Z}_1, \tag{5.8}$$

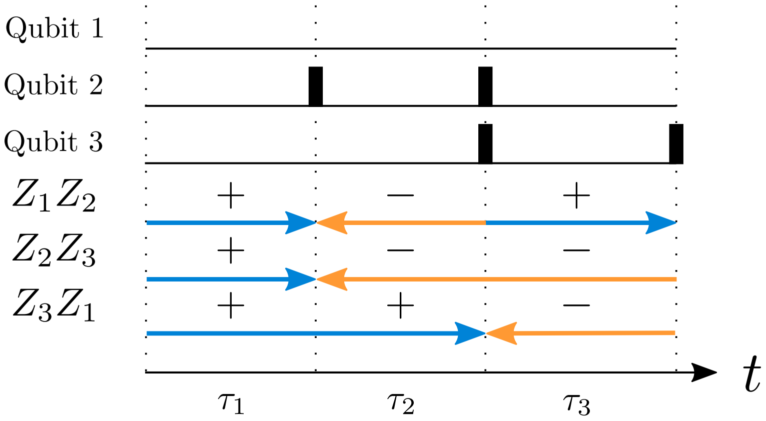

Figure 5.3: Pulse sequence of three qubit hamiltonian rescaling with minimum number of time periods.

where we assumed that the Hamiltonian is on the drive frame of each qubits' resonant frequencies, ignoring single-qubit terms. The aim is to generate arbitrary phases ϕ_{12}, ϕ_{23} and ϕ_{31} by a 3-qubit spin-echo sequence. Since there are three target phases, in principle, we only need three tuneable degrees of freedom to specify each phase individually, so we prepare three time periods, τ_1, τ_2 and τ_3, shown in Fig. 5.3. Due to sign flips of two-qubit interactions by spin-echo pulses, the phase accumulation of each coupling can be described as a set of linear equations as follows,

$$\begin{aligned}\begin{pmatrix}\phi_{12}\\ \phi_{23}\\ \phi_{31}\end{pmatrix} &= \begin{pmatrix}\omega_{12}(\tau_1-\tau_2+\tau_3)\\ \omega_{23}(\tau_1-\tau_2-\tau_3)\\ \omega_{31}(\tau_1+\tau_2-\tau_3)\end{pmatrix} = \begin{pmatrix}\omega_{12} & 0 & 0\\ 0 & \omega_{23} & 0\\ 0 & 0 & \omega_{31}\end{pmatrix}\cdot\begin{pmatrix}+1 & -1 & +1\\ +1 & -1 & -1\\ +1 & +1 & -1\end{pmatrix}\cdot\begin{pmatrix}\tau_1\\ \tau_2\\ \tau_3\end{pmatrix}\\ &= \mathrm{diag}(\boldsymbol{\omega})\cdot S\cdot\boldsymbol{t}, \end{aligned} \tag{5.9}$$

where $\boldsymbol{\omega} = (\omega_{12}, \omega_{23}, \omega_{31})^t$. The set of time periods $\boldsymbol{t} = (\tau_1, \tau_2, \tau_3)^t$ can be obtained by inverting $\mathrm{diag}(\boldsymbol{\omega})$ and the sign matrix S,

$$\boldsymbol{t} = S^{-1}\cdot\mathrm{diag}^{-1}(\boldsymbol{\omega})\cdot\boldsymbol{\phi}, \tag{5.10}$$

where $\boldsymbol{\phi} = (\phi_{12}, \phi_{23}, \phi_{31})^t$.

This method can be interpreted as Hamiltonian rescaling because the effective Hamiltonian of each time period is,

$$\hat{\mathcal{H}}_1 = \frac{1}{4}(\omega_{12}\hat{Z}_1\hat{Z}_2 + \omega_{23}\hat{Z}_2\hat{Z}_3 + \omega_{31}\hat{Z}_3\hat{Z}_1), \tag{5.11}$$

$$\hat{\mathcal{H}}_2 = \frac{1}{4}(-\omega_{12}\hat{Z}_1\hat{Z}_2 - \omega_{23}\hat{Z}_2\hat{Z}_3 + \omega_{31}\hat{Z}_3\hat{Z}_1), \tag{5.12}$$

$$\hat{\mathcal{H}}_3 = \frac{1}{4}(\omega_{12}\hat{Z}_1\hat{Z}_2 - \omega_{23}\hat{Z}_2\hat{Z}_3 - \omega_{31}\hat{Z}_3\hat{Z}_1), \tag{5.13}$$

and the entire time evolution of the quantum system can be described as,

$$\hat{U}(\boldsymbol{\phi}) = \exp\Big(-i\hat{\mathcal{H}}_3\tau_3\Big)\exp\Big(-i\hat{\mathcal{H}}_2\tau_2\Big)\exp\Big(-i\hat{\mathcal{H}}_1\tau_1\Big) \tag{5.14}$$

$$= \exp\Big(-i\hat{\mathcal{H}}_{eff}T\Big), \tag{5.15}$$

where $T = \tau_1 + \tau_2 + \tau_3$ is the total duration of the pulse sequence and the multiplication of the matrix exponentiation holds because the Hamiltonian is diagonal. By interspersing spin-echo pulses during the free evolution under Hamiltonian $\hat{\mathcal{H}}$, we are effectively simulating another Hamiltonian $\hat{\mathcal{H}}_{eff}$, whose coupling strengths are determined by choosing the time periods $\boldsymbol{t}$ specified by the linear equation (5.9).

If we could design pulse sequences that make S matrices invertible, the above-mentioned scheme only requires $O(q^2)$ time periods which is q times less than the conventional approach. The massive reduction in the number of time periods leads to fewer pulse counts, and simultaneous evolution of multiple couplings should allow shorter time duration. However, the simple argument of reducing the number of time periods does not guarantee the advantage unless we assess it quantitatively and show the resource scaling to the number of qubits. Moreover, the inversion of the S matrix in Eq. (5.10) does not give positive solutions $\boldsymbol{t}$ every time, and it was not trivial to find a systematic protocol that generates pulse sequences obtaining arbitrary target phases with positive solutions.

5.3.2 Contribution

In the following sections, we will introduce systematic pulse sequence generation algorithms to solve the issues mentioned in the previous section. Most of the contents in the next two sections are taken from published articles [35, 36], which are results of collaboration with the NMR group led by Prof. Jonathan Jones at the University of Oxford. My contributions to this work can be summarised as follows.

First, I identified the possibility of reducing the number of time periods in the Hamiltonian rescaling pulse sequences to the number of degrees of freedom in the target Hamiltonian (as explained in Subsec. 5.3.1), which is a reduction by a factor of q significantly better than the conventional NMR approach. However, the protocol I proposed was not able to produce the positive solution all the time, and the resource scaling was unknown. This was the same for the similar work independently done by [34].

I then formulated research questions, clarifying the following objectives, (1) find systematic protocols to obtain positive solutions in practical hardware settings, (2) give a resource estimate of the protocols so that they can be compared with other hardware compilation schemes and discuss the application in a wider context. The research questions attracted the NMR group led by Prof. Jonathan Jones at University of Oxford, which resulted in collaborating on the topic and finding the solution that we will explain in the following sections. The actual implementation of the simulation results in Sec. 5.4 are done by Dr. Gaurav Bhole and the essential idea of the Sec. 5.5 has been worked out by Prof. Jonathan Jones and Mr. Stephen Jones, and I have directed the development of these schemes to fit with the wider concept of hardware-efficient quantum computing and superconducting qubit implementation.

5.4 Hamiltonian rescaling by linear programming

In the previous studies, conventional NMR approaches have largely concentrated on methods for refocusing all the interactions, or for isolating one single interaction while refocusing everything else [63, 64, 95, 96]. However, a more general problem is to *rescale* the size of interactions in the Hamiltonian, to produce a desired effective

Hamiltonian. Here we describe a method for finding a rescaling sequence with the shortest possible total time, and with a fairly small number of echo pulses. In its simplest form this is practical for systems of up to about 20 qubits, but for larger systems we have developed a pragmatic method for finding short, although not perfectly optimal, rescaling sequences, which works with more than 100 qubits, meaning that the method could be of use for practically useful quantum computation in scalable platforms. Related ideas have been explored in systems with other similar Hamiltonians [34, 97, 98].

Here we outline an algorithm based on linear programming for achieving time-optimal rescaling solutions (see Fig. 5.4 for the overview).

Step 1: Setting up the problem

We consider a system of q coupled qubits described by $r = q(q+1)/2$ one- and two-qubit interactions. Our aim is to rescale all r interactions simultaneously such that they reach the desired target phases, which for generality we assume to be all different. We begin by constructing an overcomplete Walsh basis by building a one-qubit sign matrix with the rows given by Walsh functions numbered 2^j, where $j = 0, 1, \ldots (q-1)$. Next, we use this matrix to construct the two-qubit sign matrix by taking products of corresponding rows in the one-qubit matrix.

Combining these by stacking the two matrices together gives the complete sign matrix S of r rows and $s = 2^q$ columns. The single-qubit functions correspond to binary numbers with precisely one bit set, while the two-qubit functions correspond to binary numbers with precisely two bits set. As these numbers are all distinct it is guaranteed that the complete sign matrix has enough flexibility to permit every interaction to be controlled separately. This is quite different from refocusing sequences, where many functions are repeated.

Step 1: Setting up the problem

System parameters

$$(\Omega_1, \quad \Omega_2, \quad \Omega_3, \quad \omega_{12}, \quad \omega_{23}, \quad \omega_{31}) = (17495, \quad 3294, \quad -17495, \quad 69.9, \quad -128.1, \quad 47.6)$$

Target phases

$$(\Phi_1, \quad \Phi_2, \quad \Phi_3, \quad \phi_{12}, \quad \phi_{23}, \quad \phi_{31}) = (0, \quad 0, \quad 0, \quad \pi, \quad \pi, \quad \pi)$$

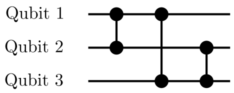

Sign matrix S

$$\begin{pmatrix} W_1 \\ W_2 \\ W_4 \\ W_3 \\ W_5 \\ W_6 \end{pmatrix} = \begin{pmatrix} +1 & +1 & +1 & +1 & -1 & -1 & -1 & -1 \\ +1 & +1 & -1 & -1 & -1 & -1 & +1 & +1 \\ +1 & -1 & -1 & +1 & +1 & -1 & -1 & +1 \\ +1 & +1 & -1 & -1 & +1 & +1 & -1 & -1 \\ +1 & -1 & -1 & +1 & -1 & +1 & +1 & -1 \\ +1 & -1 & +1 & -1 & -1 & +1 & -1 & +1 \end{pmatrix}$$

Step 2: Linear programming

$$\underbrace{(\Omega_1, \quad \Omega_2, \quad \Omega_3, \quad \omega_{12}, \quad \omega_{23}, \quad \omega_{31})}_{1 \times r} \cdot \underbrace{\begin{pmatrix} \\ S \\ \\ \end{pmatrix}}_{r \times 2^q} \cdot \underbrace{\begin{pmatrix} \\ \tau_m \\ \\ \end{pmatrix}}_{2^q \times 1} = \begin{pmatrix} \Phi_1 \\ \Phi_2 \\ \Phi_3 \\ \phi_{12} \\ \phi_{23} \\ \phi_{31} \end{pmatrix}$$

Step 3: Extracting solutions

$$\begin{pmatrix} W_1 \\ W_2 \\ W_4 \\ \tau_m \end{pmatrix} = \begin{pmatrix} +1 & +1 & +1 & +1 & -1 & -1 & -1 & -1 \\ +1 & +1 & -1 & -1 & -1 & -1 & +1 & +1 \\ +1 & -1 & -1 & +1 & +1 & -1 & -1 & +1 \\ 4.4 & 2.8 & 0 & 3.6 & 2.8 & 4.4 & 3.6 & 0 \end{pmatrix}$$

Step 4: Optimising the solutions

$$\begin{pmatrix} R_1 \\ R_2 \\ R_3 \\ \tau_m \end{pmatrix} = \begin{pmatrix} +1 & +1 & -1 & -1 & -1 & +1 \\ +1 & +1 & +1 & -1 & -1 & -1 \\ +1 & -1 & -1 & -1 & +1 & +1 \\ 4.4 & 2.8 & 3.6 & 4.4 & 2.8 & 3.6 \end{pmatrix}$$

Step 5: Building the pulse sequence

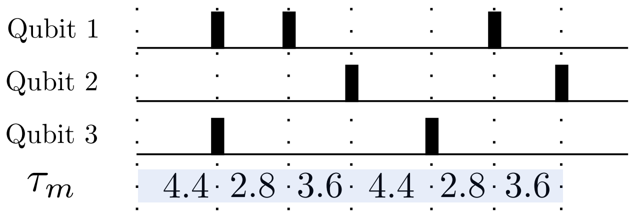

Figure 5.4: The overview of the pulse sequence generation algorithm using linear programming. As an example, we illustrate a concrete application of our algorithm using the three ^{19}F nuclei in iodotrifluoroethene, forming a three-qubit full coupled homonuclear NMR system. All interactions are written in Hz and times in ms. The stages of the implementation are described in the main text.

Step 2: Linear Programming

This overcomplete Walsh basis guarantees that solutions to Eq. (5.3) can be found for any target values of $\{\Phi_i\}$ and $\{\phi_{ij}\}$ by choosing 2^q appropriate values of $\{\tau_m\}$, but it is not obvious how these can be found. As the basis is overcomplete, multiple solutions will exist but these can be distinguished by requiring that all the times $\{\tau_m\}$ must be non-negative and by preferring the solutions with the shortest value of total time $T = \sum_m \tau_m$. These criteria for desirable solutions suggest a powerful method, namely linear programming [99].

The general linear programming problem varies some inputs (here the times $\{\tau_m\}$) seeking to minimise some linear function of these inputs (here the total time T) subject to a number of equality constraints (here Eq. (5.3)) and inequality constraints (here, that each $\tau_m \geq 0$). We adopted a simple approach, using the inbuilt Matlab function `linprog`.

It is important to consider the computational complexity of linear programming, as this determines how the time required to find a solution scales with the number of qubits q. The precise computational complexity of linear programming is known to be poorly defined, depending on both the algorithm used and the details of the problem, and with the worst case behaviour being very different from the typical case [99]. The Matlab function `linprog` has a choice of two algorithms: the original simplex algorithm developed by Dantzig [100], and a more modern interior point algorithm [101]. Both algorithms typically have computational complexity between $O(n^2)$ and $O(n^3)$, where n, the dimension of the problem, can be taken as the sum of the number of rows and columns in the constraint matrix, so that here $n = r + s \approx 2^q$. We investigated this question experimentally by simply timing the program. All results are for the simplex algorithm unless otherwise stated.

Step 3: Extracting solutions

As the linear programming algorithm is fundamentally trying to minimise T, subject to the positivity constraint and the target phases, the algorithm prefers solutions where many of the $\{\tau_m\}$ are zero. (This is not specific to this problem, but is a general feature of linear programming solutions [102].) The linear programming solution has at most only as many non-zero times as the number of constraints r in the problem. If the problem involves extensive refocusing rather than rescaling then solutions with an even smaller number of non-zero times can be found.

It is obviously not necessary to explicitly implement the time periods of length 0, and so the overcomplete sign matrix, S, can be replaced by a reduced matrix, R, by selecting only r or fewer columns from S which correspond to non-zero evolution times.

Step 4: Optimising the solutions

One subtlety is that the order of columns in the R matrix does not affect the phases produced, but different orderings of these columns can lead to pulse sequences with different numbers of pulses. As minimising the number of pulses is desirable it is useful to explore different permutations of the R matrix, seeking for the arrangement which gives the smallest number of sign changes.

If the matrix is not too large then exhaustive permutation can be practical, but in larger cases it is more sensible to select a number of random permutations and keep the best one found. Experience so far suggests that different permutations can require numbers of pulses that differ by a factor of around two. We also find that the pulse pattern corresponding to the original R matrix is typically relatively good, although rarely the absolute best.

Step 5: Building the pulse sequence

From this optimal reduced matrix R, a pattern of pulses can be generated by applying a π pulse to every qubit whose sign changes. It is important to remember that all interactions start at $+1$ and must end at $+1$, which can be modelled by adding initial and final columns to R containing entirely $+1$. These additional columns have evolution times set to zero, and so are not actually implemented, but the resulting sign changes make it necessary to apply pulses to some qubits at the start and end of the sequence. This also ensures that the number of π pulses applied to each qubit is even, which is required to create true spin echoes.

As the reduced matrix has $r \approx q^2/2$ times the final pulse sequence will have $O(q^2)$ time periods and $O(q^3)$ individual π pulses, which is a very significant improvement on naive methods.

5.4.1 General solutions

We have repeated calculations of this kind in a large variety of fictitious spin systems with increasing numbers of qubits, up to $q = 18$, and solutions have always been found. For larger values of q these solutions are always more time-efficient than the sequential approach, and are usually far quicker. The greatest savings are found in cases where a moderate number of gates need to be implemented in parallel, and particularly when unused long-range couplings are significantly weaker than the couplings being controlled.

Until now we have described the problem as if there was a unique optimal solution which the linear programming locates. In fact there are multiple equivalent solutions, from among which the linear programming chooses one. These alternative solutions can be easily generated by permuting the columns of the S matrix before running the algorithm, but as they all have the same number of individual time periods and take the same total time there is no good reason to do this.

We note in passing that these optimal solutions are only optimal for implementations containing only delays and π pulses. If it is desired to implement an evolution corresponding to a weak long-range coupling then it may be quicker to use SWAP gates and related methods to implement long-range interactions through a chain of stronger short-range interactions [103, 104]. Even in such cases, however, the ideas described here can be used to assist in the design of such indirect gates.

Computation time complexity

The principal downside of this approach is that the computational time needed to run linear programming increases with the size of the basis set, and this grows as $s = 2^q$ for the current method. As discussed above a computation time scaling proportional to $(s + r)^2$ or $(s + r)^3$, where r is the number of equality constraints, is likely, which for large q is dominated by the exponential growth in s. This is confirmed by a plot of time required on a desktop computer (Intel Core i7-9700, 3.0–4.7 GHz, with 12 MB cache and 40 GB RAM), shown in Fig. 5.5. The linear behaviour at large q on this semi-log plot indicates exponential computational time complexity, and the gradient is consistent with the time required scaling as about 4^q.

Although attempts have been made to parallelise linear programming algorithms, progress so far has been limited [105]. Thus, this method seems to be practical only up to a small number of qubits, perhaps $q = 20$. Indeed much above 20 qubits it becomes difficult even to hold the S matrix in memory on a desktop computer, although this could be sidestepped with a customised algorithm. While it is true that 20 is quite a large number of qubits in the context of conventional NMR or even NMR QIP, we do not want to restrict ourselves to NMR spin systems but to extend to more general quantum systems which have the potential for a scalable quantum computing

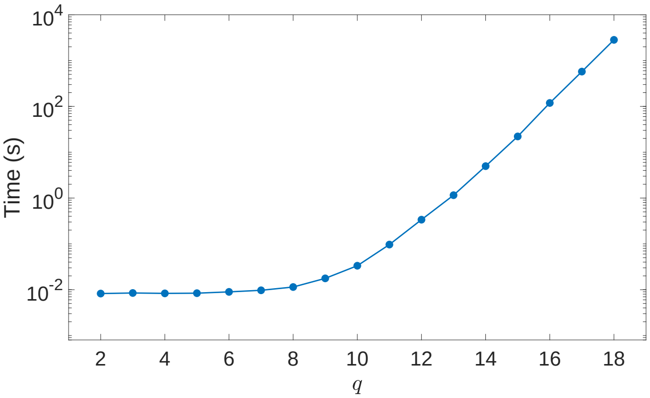

Figure 5.5: The computation time required to find a linear programming solution on a desktop computer as a function of q. For small values of q this time is almost constant, but rises exponentially for larger q, rendering this method impractical beyond around 20 qubits. Timings are shown for the interior point algorithm, but results were very similar for the simplex algorithm. Error bars (estimated by repetition) are comparable to the size of the symbols, and the line simply joins the individual points.

architecture. Fortunately, a more sophisticated approach is available which takes time only polynomial in q, albeit with a high power.

5.4.2 Rescaling in larger systems

The fundamental problem which slows down the rescaling algorithm is the exponentially large size of the overcomplete basis. This basis contains $s = 2^q$ columns, from which the linear programming selects at most $r = q(q + 1)/2$, equal to the number of interactions, and in many cases fewer. For moderate values of q, these numbers r and s are quite similar, but the difference grows rapidly with q, leading one to wonder whether there is some way to cut down the size of S before starting the linear programming step. Is it really necessary to include a very large number of columns, the great majority of which will eventually be discarded? In this regard we note that once one has identified the appropriate reduced sign matrix then the times required can be found by direct inversion of this r by r square matrix. However it is clear that most of the hard work is done in locating the appropriate columns used to construct the reduced sign matrix.

Starting from the other extreme, one could just select r random columns from the full sign matrix and try to invert this. However, this process can fail in a number of ways. Firstly, the reduced matrix might not be of full rank (although this is unlikely when $s \gg r$) and so may not have an inverse. Even for a reduced matrix with full rank, the set of times obtained from the inversion process is very likely to include some negative times which are not physically implementable. Lastly, even if all the times are non-negative, the total time will not normally be the desired minimum, and so the sequence will not be time-optimal.

Between these extremes there is a middle way: using linear programming on a reduced, but still overcomplete, basis set. The current linear programming approach starts from the largest conceivable basis set, containing all of the $s = 2^q$ possible sign patterns, which guarantees finding an optimal solution but also makes the process slow. One might imagine choosing some subset of columns at random, and attempting linear programming on this subset. For large values of q the gap between the full size $s = 2^q$ and the minimum size r becomes very significant. It is thus worth exploring how many columns need to be picked so that linear programming generally finds a solution. There is no guarantee that such solutions will be time optimal, but as long as the random choice contains all the components of at least one optimal solution, then linear programming will find this. Given the very large number of equivalent solutions identified for moderate values of q it seems plausible that this could be achieved with quite a small subset.

The RROS method

In the random reduced overcomplete set (RROS) method, instead of using all s columns of the sign matrix S as in the exhaustive approach, we choose just kr columns

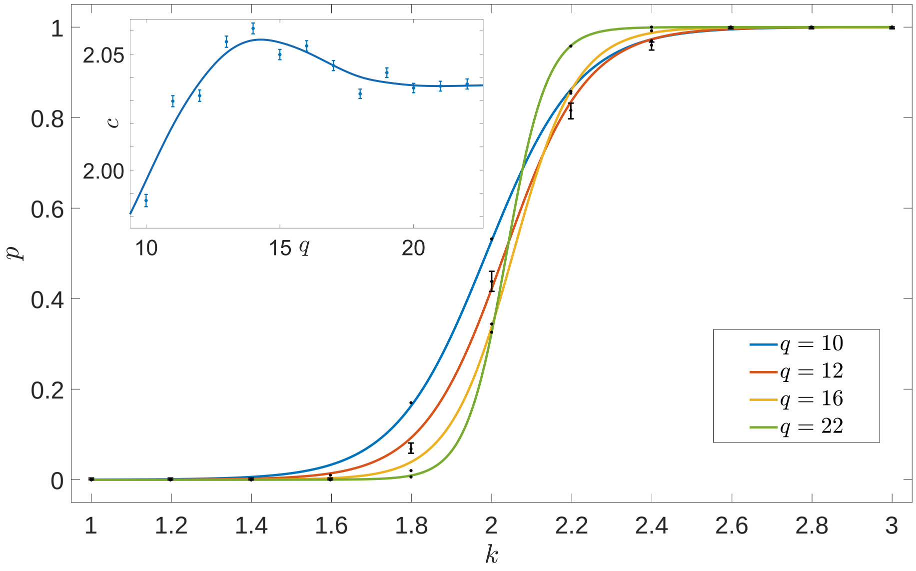

Figure 5.6: The effectiveness of the RROS method selecting kr columns at random, showing how the probability of the algorithm finding a solution depends on q and k. Calculations were performed for q ranging from 10 to 22 but only four selected values are shown. Error bars on the $q = 12$ points were estimated using Bayesian credible intervals; error bars for other curves are very similar. Fitted sigmoidal curves were used to estimate the value of k at which this success probability reached 50%. The inset shows the location of this transition point as a function of q. Error bars are estimated using error propagation from the sigmoidal fit results; the smooth curve has no significance and is plotted simply to guide the eye.

from S, for some $k > 1$, and run linear programming. Of course, one does not have to explicitly construct the entire S matrix and then choose the kr columns as these kr columns correspond to the binary representations of kr distinct decimal numbers chosen randomly from 0 to $s - 1$. Our experience so far suggests that the probability of finding a possible solution, which achieves the desired phases using only positive evolution times, increases as k increases, with a transition point around $k = 2$, at which the probability of a random set giving a solution reaches 50%.

This observation is substantiated by the empirical evidence in Fig. 5.6. RROS was run 500 times for values of q ranging from 10 to 22 with k varied between 1 and 3, and the fraction of occasions f when linear programming found a suitable solution was calculated. Error bars on these estimates were calculated using Bayesian credible intervals [106], corresponding to the region of the probability density function within ±34% of the median, equivalent to 1 standard deviation for a Normal distribution. It is clear that the probability of success rises sharply as k passes some critical value, with this transition becoming sharper as q is increased. To help locate this transition point a sigmoidal logistic function [106],

$$f(k) = \frac{1}{1 + \exp[-b(x - c)]}, \tag{5.16}$$

was fitted for each value of q, with c being the transition point at which the success probability passes 50%, and b indicating the sharpness of the transition. Although this function was chosen for convenience it clearly fits fairly well. A plot of the value of c as a function of q shown as an inset to Fig. 5.6 suggests that the transition lies just above $k = 2$. For large values of q this transition becomes sharp, so that for $k \geq 2.5$ it is almost certain that a solution will be found.

If a solution is found then this solution will be time-optimal for the subset of columns chosen, but there is no guarantee that this will be the overall optimum, taking the shortest possible time. Unsurprisingly the probability of finding a solution reaching the shortest possible time increases as k increases, but investigating this question in detail is challenging, as for large values of q the overall time-optimal solution cannot be located in a reasonable time. Nevertheless our preliminary studies suggest that for large q the quality of solutions plateaus around $k \approx 4$, and so there is little point going beyond this in practice. For small values of q it seems to be necessary to use a slightly larger value of k, but in these cases it is more sensible just to use direct solution of the full S matrix anyway.

Results for large numbers of qubits

The use of a smaller basis set permits RROS to be extended to much larger values of q. This was investigated by running the algorithm for q between 10 and 60, as shown in Fig. 5.7. For RROS the time required to perform linear programming depends not only on the randomly chosen Hamiltonian and target phases but also on the precise choice of columns, and so timings were repeated 10 times using different choices. As expected for $k = 4$ a solution was located in every case.

The simplex algorithm was found to be slightly faster than the interior point algorithm for $q \leq 31$, but the interior point algorithm was faster for $q \geq 32$, and became much faster at high q. The discontinuity in the interior point timings between $q = 31$ and $q = 32$ may indicate a change in the precise algorithm used by Matlab.

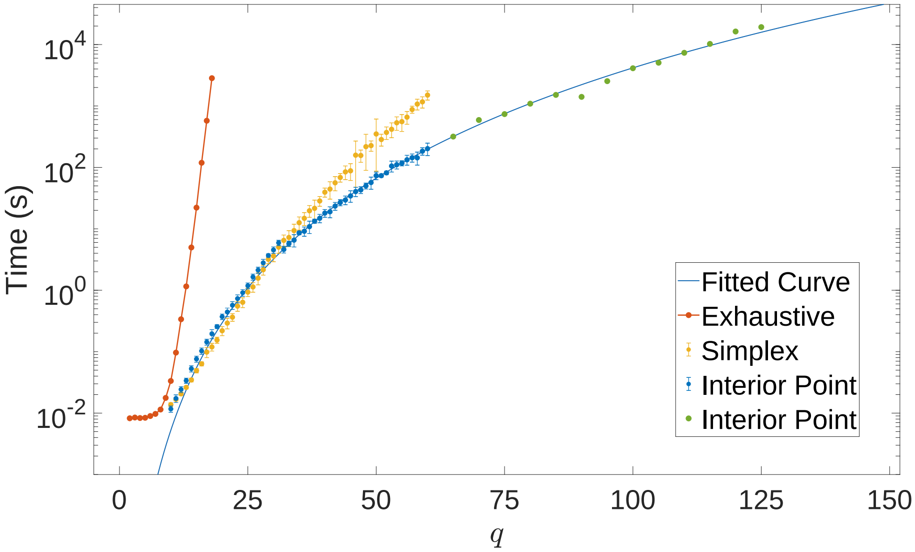

Figure 5.7: The computation time required to perform linear prediction using RROS with $k = 4$. The simplex method was found to be fastest for $q \leq 31$, with the interior point method faster for $q \geq 32$. Error bars for $q \leq 60$ indicated the mean and SD over 10 repetitions. The smooth curve with the form Ar^3 is fitted to interior point timings in the range $32 \leq q \leq 60$. Data points for $q > 60$ are single repetitions and were not included in the fit. The fact that these points lie very close to the extrapolated fit suggests that our fitted curve is a good model. The red points on the left show timings for exhaustive calculations, demonstrating the huge time gains possible with RROS.

For RROS the dimension of the problem is $n = r + kr$ and so we expect a computational complexity between $O(r^2)$ and $O(r^3)$. The smooth curve in the figure was fitted to the timings from the interior point algorithm for the range $32 \leq q \leq 60$ using a power function, and takes the form Ar^3, consistent with our expectations (including the power as an additional fitting parameter gave a value indistinguishable from 3). The timings for the simplex algorithm appear to lie between $O(r^4)$ and $O(r^5)$, which is much slower than the interior point.

With the simplex algorithm the number of time periods required was always approximately equal to r (in some cases a small number of time periods were negligibly short and so could be dropped). The number of pulses required was determined for the R matrix as originally found, without further optimisation, and was typically around $qr/2 \approx q^3/4$, confirming our previous expectations. With the interior point algorithm the solutions always use all kr time periods, with a large number of very short times rather than a clear division into zero and non-zero times. These initial solutions can then be simplified by choosing a smaller subset of $k'r$ columns, with $k' \approx 1.2$, corresponding to the columns with the largest time values in the original solution. Surprisingly the computational time for these recalculations appears to be linear in k, while a quadratic or cubic dependence might have been expected.

The calculation was then extended to higher values of q, using only a single repetition, and these data points were found to lie very close to the extrapolated curve. As $r \approx q^2/2$ this gives a pragmatic computational time scaling of $O(q^6)$, which is polynomial in the number of qubits. Extrapolating this curve still further suggests that calculations with up to about 150 qubits could be practical, but the Matlab implementation `linprog` runs out of memory above $q = 125$. This limit should be solvable by a custom implementation of linear programming.

5.4.3 Summary of the linear programming method

We have presented a practical algorithm which is guaranteed to find the minimum time solution to rescaling $\hat{Z}$ and $\hat{ZZ}$ terms in the internal Hamiltonian of a quantum computer with up to about 20 qubits. Above 20 qubits the direct approach becomes intractable, but random sampling will extend this (although the solution might not be quite time optimal) to more than 100 qubits. Beyond about 150 qubits the q^6 scaling of the computational time for a fully coupled system renders any known approach impractical. It is, however, very unlikely that any system of that size would still be fully coupled, as couplings are usually only substantial between nearby qubits. In partially coupled systems r is linear in q rather than quadratic, and allowing for this should permit the process to be extended to hundreds or even thousands of qubits.

Although described in the language of NMR the techniques used are applicable to any equivalent system, where an always-on two-qubit interaction commutes with the single-qubit background terms. It may be of particular value in solid state platforms, such as superconducting circuits, in which 2D lattices of qubits are developed with a sparse coupling network (generally nearest-neighbour). In such very large systems it is likely that the underlying structure in the pattern of interactions will allow symmetries to be exploited, potentially simplifying the problem greatly.

5.5 Hamiltonian rescaling in qubit arrays with nearest-neighbour couplings

In the previous section, we have described methods for finding time-optimal rescaling sequences in systems of up to around 20 qubits, and near-optimal sequences for around 100 qubits. However, these methods do not scale to larger systems, as the computational time required to find such solutions grows rapidly with the number of qubits. The most general form of the Hamiltonian,

$$\hat{\mathcal{H}}/\hbar = \sum_i \frac{\Omega_i}{2}\hat{Z}_i + \sum_{i<j} \frac{\omega_{ij}}{4}\hat{Z}_i\hat{Z}_j. \tag{5.17}$$

will have all offsets and all possible couplings present, but couplings are generally only significant between nearby qubits. For example, superconducting qubits are often engineered in a square-lattice [22] and can have couplings limited to only nearest or next-nearest neighbour qubits if circuits are well microwave engineered [107]. Here we describe a method based on graph colouring for rapidly finding near-optimal sequences in these highly practical locally coupled systems. Remarkably we find that in this partially-coupled scenario, which is very realistic for large-scale superconducting circuits, the refocusing and rescaling of always-on couplings can be *efficiently* programmed, requiring only linear time to design control sequences and linear number of control pulses.

We start by applying the refocusing scheme to the smallest possible case of a nearest-neighbour square lattice, and then generalise to arbitrary lattice sizes. Initially we will assume the square lattice to be engineered with identical couplings between nearest neighbours and no long range couplings at all, but both of these restrictions will subsequently be partly relaxed.

We assume throughout this section that it is possible to apply ideal single qubit gates to any combination of qubits, despite the presence of the background Hamiltonian, finding the simplest set of control pulses rather than considering how these pulses might themselves be implemented. Experimental implementations will need to use either general approaches such as gradient-ascent pulse engineering (GRAPE) pulses [74], or specific methods tailored to this precise situation [108, 109, 110], but we will leave these pulse engineering improvement in future studies.

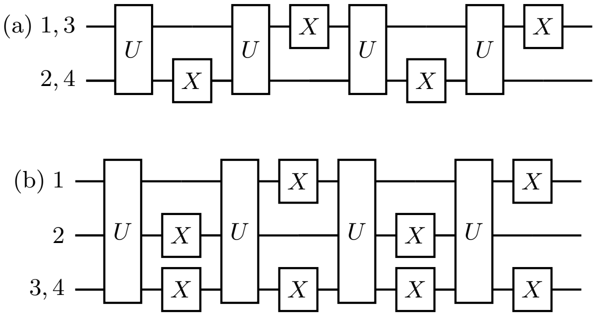

Figure 5.8: Networks to (a) refocus all offsets and couplings in a square of four qubits with only nearest-neighbour couplings, and (b) keep only the coupling between qubits 3 and 4. Here X indicates a gate while U indicates evolution under the background Hamiltonian. Labels on the left indicate which qubits the gates are applied to.

5.5.1 Square lattices

We begin with the smallest possible square lattice, containing four qubits with identical nearest neighbour couplings $\omega_{j,j+1}$ and ω_{14} only. Non nearest-neighbour pairs have no coupling, so $\omega_{13} = \omega_{24} = 0$. We can refocus all the couplings in the system, as well as any offsets present, using the circuit of spin-echoes shown in Fig. 5.8(a). Here, the unitary U describes the evolution of the system under the background Hamiltonian $\hat{\mathcal{H}}$ given by the propagator $U = \exp\left(-\frac{\mathrm{i}\hat{\mathcal{H}}t}{\hbar}\right)$, while the gates are represented by X. As there is no coupling to be refocused between qubits 1 and 3 it is possible to apply the same pattern of gates to them both, and similarly for qubits 2 and 4, so only two distinct patterns of gates are required.

This network can also be extended to retain a single coupling, as shown in Fig. 5.8(b). In this network the same pattern of gates is applied to qubits 3 and 4, and the corresponding coupling is retained, while the remaining couplings are refocused [63]. These networks can be extended to retain *any* pattern of couplings in a square lattice system.

This extension works by colouring the square lattice, as described in [63]. The system can be described as a noncomplete graph, with vertices corresponding to

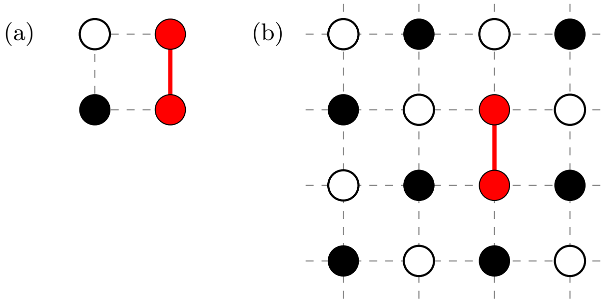

Figure 5.9: (a) Retaining a nearest neighbour coupling in a square requires three colours: decoupled qubits are coloured black and white, while the coupled qubits are coloured red. Grey dashed lines show couplings which have been refocused. (b) The same result can be achieved in a larger array by colouring surrounding qubits alternately black and white.

qubits and edges to couplings, with only some of the possible edges present. The graph can be coloured by assigning a colour to each vertex, and is said to be properly coloured, corresponding to complete refocusing, if no two connected vertices are the same colour. Thus in the fully-decoupled square of four qubits we can colour qubits 1 and 3 black and qubits 2 and 4 white, while to retain a single coupling the pair of qubits involved must be assigned the same third colour, say red, as shown in Fig. 5.9(a). To implement a colouring, we use patterns of gates corresponding to distinct Walsh functions [35, 63] for each colour.

This colouring pattern can be tessellated across a lattice, as shown in Fig. 5.9(b), by colouring surrounding qubits alternately black and white. Here we show a four-by-four patch containing sixteen qubits, which can be embedded in a larger lattice, retaining a single coupling while refocusing all the other interactions. The required pulse sequence can be obtained by assigning black qubits B to the first Walsh pattern, white qubits W to the second, and the two red qubits R to the third, to obtain the sequence

$$U\,X_{\mathrm{WR}}\,U\,X_{\mathrm{BR}}\,U\,X_{\mathrm{WR}}\,U\,X_{\mathrm{BR}}, \tag{5.18}$$

where X_{WR} indicates that NOT gates are applied to the white and red qubits, and so on. Just like the sequence for the four-qubit system, this sequence requires only 4 time periods, but now requires $2q+4$ pulses for a system of q qubits. The total time required to implement the network for a π evolution, corresponding to a CNOT gate [35], is $T = 1/2J$, where the nearest-neighbour couplings are of size $\omega = 2\pi J$. This is the same time as is needed for an isolated coupling, as the retained coupling evolves at full strength.

The approach above will refocus all single-qubit interactions, but it is simple to modify the X gates in the network to implement single-qubit rotations directly. This relies on the identity [111]

$$\pi_{\phi_2}\pi_{\phi_1} = 2(\phi_2 - \phi_1)_z, \tag{5.19}$$

so that applying two π rotations around axes in the xy-plane separated by an angle δ is equivalent to performing a z-rotation through an angle 2δ. These rotations can be performed by modifying any pair of X gates in any refocusing network, and as each qubit is controlled separately different rotations can be applied to different qubits at no cost in time or pulse count.

5.5.2 Parallel gates

If it is desired to retain several different coupling interactions then this can be achieved most simply by applying such patterns back to back, changing the colouring at each stage, but it is more efficient to as far as possible perform evolutions in parallel. For simple cases this can be achieved as shown in Fig. 5.10. Qubits which are part of the same coupling island, that is qubits which are connected either directly or indirectly by retained couplings, have been coloured the same colour. (Note that the single yellow qubit forms an island on its own.)

This simple approach will only be successful when, as here, all the couplings which could appear in an island are retained. In such cases this simple colouring strategy

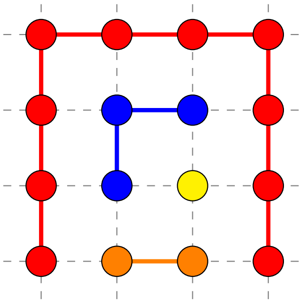

Figure 5.10: Retaining a more complex pattern of couplings in a square lattice: this pattern requires four colours.

will retain all the desired couplings while refocusing all the couplings between islands, reproducing the desired pattern in one go. As before, the total time required is just $T = 1/2J$, the same as for an isolated coupling.

It might appear that this approach would require the number of colours to equal the number of islands, but in fact it is never necessary to use more than four, since islands which are completely disconnected (that is, islands which are not connected by couplings in the underlying Hamiltonian) can be safely coloured the same. By the four-colour-map theorem this will never require more than four colours [112]. These four colours can be assigned to four Walsh functions [35], requiring T to be divided up into eight equal time periods. Assigning the most common colours to W_1 and W_2, which both require two pulses, and the two rarer colours to W_3 and W_4, which require four pulses, means that the total number of pulses required in a system of q qubits lies between $2q$ and $3q$.

Although this method will work for some simple target patterns, it will not work in general, since many target patterns have one or more missing couplings. Consider, for example, the pattern shown in Fig. 5.11, where the black couplings must be retained, and the dashed red couplings must not be retained although they connect qubits within the main island. Any colouring which implements all the black couplings that must be retained will also implement the unwanted red couplings, and so this target

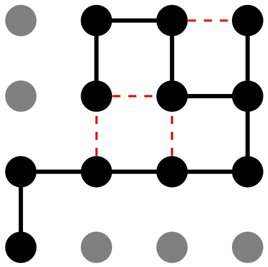

Figure 5.11: A target pattern of couplings which cannot be implemented with a single colouring pattern. Although the grey qubits are easily decoupled from each other and from the black island, it is impossible to retain all the desired black couplings without also retaining the undesired couplings shown as dashed red lines.

pattern cannot be implemented with any single colouring pattern.

5.5.3 Multiple colourings

There is, however, a simple method for achieving *any* target pattern with two sequential colourings, each using four colours. As an example a pair of colourings which implements the target couplings in Fig. 5.11 is shown in Fig. 5.12. Pattern (a) assigns two colours to the odd-numbered rows and two more to the even numbered rows, thus ensuring horizontal couplings can be controlled while all vertical couplings will be refocused. Along a row, the colour of the first qubit is arbitrary, but the following qubit must be the same colour if the corresponding coupling is to be retained, and the other colour if it is to be refocused. Pattern (b) assigns colours to columns instead of rows to control vertical couplings in an analogous way.

As any subset of horizontal couplings can be selected by the first colouring, and any subset of vertical couplings can be selected by the second, any target pattern at all can be implemented in this way, in a total time $2T$. This total time will be divided into 16 equal time periods, separated by no more than $6q$ individual pulses.

It is useful to compare this result with timings found by our previous algorithm based on linear programming with an exhaustive basis set, which is guaranteed to find

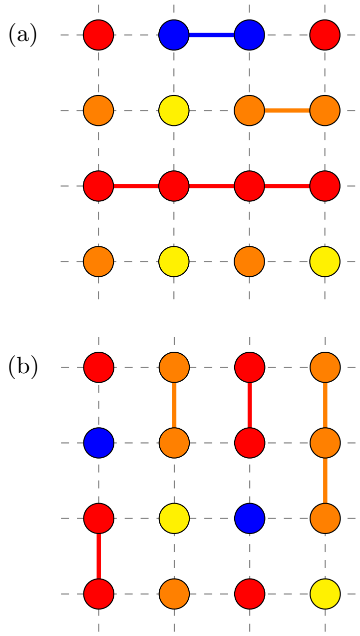

Figure 5.12: A solution implementing the target couplings in Fig. 5.11 using two sequential colouring patterns, (a) and (b).

a true minimum-time solution. The computational complexity of this algorithm renders it impractical for large arrays, but for four-by-four arrays with nearest-neighbour couplings it is perfectly practical. We have analysed a very large number of randomly chosen targets in four-by-four arrays, and in every case the optimal solution required a total time of either T (in cases with no missing couplings, so a single colouring is possible) or $1.5\,T$ (in cases where this is not possible).

The implementation time required for our colouring based networks, $2T$, is slightly longer than the absolute minimum required, but these colourings are far easier to design, with a computation time scaling only *linearly* with the total number of qubits, and so can be applied to systems any number of qubits. The number of gates required is also greatly reduced, from $O(q^2)$ for linear programming based solutions to $O(q)$.

5.5.4 Next-nearest neighbours

Until now we have assumed that only nearest-neighbour interactions are important, with all others being too small to matter. In practice, real physical systems are likely to also have non-zero couplings at longer range. It is reasonable to expect such couplings to drop with distance in well-engineered devices, making the next-nearest neighbour interactions, across the diagonals of the square array, the most significant. In the original two-colour refocusing scheme qubits connected by next-nearest neighbour interactions will be the same colour, both black or both white, and so these interactions will be retained rather than refocused, leading to a significant error in the final gate implementation.

This is not a problem with the general four-colour scheme, as the use of different colours for alternate rows and columns guarantees that diagonally connected qubits will be of different colours. Thus these networks automatically suppress any unwanted diagonal couplings, which can therefore simply be ignored. Suppressing even longer range couplings is more complicated, but can be achieved using larger numbers of colouring patterns with more colours used in each pattern, as described in the Appendix A.5.

5.5.5 Different evolution times

The parallel gates approach, however, hides a further important assumption: it is not sufficient to retain two different couplings if they are required to evolve for different times, either because different couplings must evolve through different angles, or because apparently equivalent couplings will have different strengths, and so will need different evolution times to achieve the same angle.

It might seem necessary to apply such gates using different echo sequences, but in fact they can be partly combined. Consider two couplings in the same group, where one requires evolution for a total time T_A and the second for a time T_B, with $T_B > T_A$. The naive approach is to use two different colouring patterns, one implementing the first coupling for time T_A, and another implementing the second coupling for T_B. In fact these periods can be carried out partly in parallel: during the first period, which lasts for time T_A, *both* couplings are retained, while for the second period, which lasts for time $T_B - T_A$, only the second coupling is retained. Thus both couplings can be carried out in a total time T_B, and the method generalises for any number of distinct couplings strengths.

It follows that *any* pattern of couplings can be achieved in an evolution time equal to the sum of the longest evolution times required for horizontal and vertical couplings, which itself is no more than $2T_{\max}$, where $T_{\max} = 1/2J_{\min}$ is the evolution time required for the slowest gate. However the resulting sequences will contain $O(q)$ evolution times and $O(q^2)$ pulses, while designing such sequences requires sorting the evolution times into ascending order, with computational time complexity $O(q \log q)$. They will also be impractical to implement experimentally, as the differences between very similar times may be smaller than the clock resolution.

Rather than implementing a very large number of distinct evolution times precisely, it makes more sense to use a much smaller number of evolutions to approximate all the desired times. This is most easily achieved by dividing the range of evolution times by successive powers of two, in effect encoding each evolution time as a binary number. Using k different evolution times results in k-bit precision, with an exponential increase in precision with a linear increase in the number of evolution times used. By accepting a degree of approximation one can reduce the time complexity from $O(q \log q)$ to $O(kq)$, and reduce the pulse count from $O(q^2)$ to $O(kq)$, where the constant k depends on the accuracy required. For example, using 20 distinct delays will allow angles to be approximated to a precision better than 10^{-6}.

5.5.6 Summary of the colouring method

The colouring technique described here allows the efficient control of interactions in qubit arrays of arbitrary size, provided the couplings are constrained to be local. While the resulting pulse sequences take slightly longer to implement than the absolute minimum time required, the computational time is vastly reduced, from $O(4^q)$ for exhaustive linear programming, or $O(q^6)$ for RROS [35], right down to $O(q)$, rendering them practical in systems with thousands or even millions of qubits. The number of control pulses is also greatly reduced, from $O(q^2)$ to $O(q)$, thus reducing implementation errors. The method can handle unwanted next-nearest neighbour couplings, and is easily extended in a scalable way to systems with variable coupling strengths or evolution angles.

5.6 Conclusion

To conclude, we compare the physical and computational resource for each method and discuss the improvement from the same algorithm compilation using the conventional NMR approach ("Naive" in Table 5.1).

	Naive	LP	RROS	Colouring	Colouring*
Total duration	$\sum_{i<j} \frac{\theta_{i,j}}{2J_{i,j}}$	$\max\{\frac{\theta_{i,j}}{2J_{i,j}}\}$	$\max\{\frac{\theta_{i,j}}{J_{i,j}}\}$	$\max\{\frac{\theta_{i,j}}{J_{i,j}}\}$	$\max\{\frac{\theta_{i,j}}{J_{i,j}}\}$
No. of time periods	$\mathcal{O}(q^3)$	$\mathcal{O}(q^2)$	$\mathcal{O}(q^2)$	$\mathcal{O}(q)$	$\mathcal{O}(k)$
Pulse counts	$\mathrm{O}(q^4)$	$\mathcal{O}(q^3)$	$\mathcal{O}(q^3)$	$\mathcal{O}(q^2)$	$\mathcal{O}(kq)$
Complexity	$\mathcal{O}(1)$	$\mathcal{O}(4^q)$	$\mathrm{O}(q^6)$	$\mathcal{O}(q \log q)$	$\mathcal{O}(q)$
Number of qubits	no limit	20	150	millions	billions
Connectivity	A-to-A	A-to-A	A-to-A	NN	NN

Table 5.1: Resource comparison of Hamiltonian simulation

In Subsec. 5.2.3, we have reviewed the naive approach using an efficient decoupling pulse sequence [63, 64], and estimated the total duration and the pulse count of the Hamiltonian simulation. The benefit of the conventional approach is its simplicity in designing the decoupling sequence, which allows the compilation of the Hamiltonian simulation possible regardless of the number of qubits and the coupling pattern. By carving out a single two-qubit interaction while decoupling all other couplings, we can compile a Hamiltonian simulation using the gate-based approach straightforwardly. However, the simplicity in the algorithm compiling complexity comes at a price of unfavourable scaling in physical resources such as total duration and the pulse count of the pulse sequence. Since nearly all couplings are turned off in each two-qubit gate application, most of the entangling resource in the coupled qubits has been wasted each step. Also, the number of pulses required for the decoupling sequence scales with the number of qubits q, so the pulse sequence will get crowded as we increase the number of qubits. This introduces more single-qubit gate errors and does not reduce the duty cycle of active quantum operation in a large number of qubits, which makes the conventional NMR approach infeasible for our motivation to implement a large-scale quantum computation using native interactions.

To overcome the limitation of the conventional NMR approach, we avoid turning off most of the couplings. We utilise the couplings present in the system as much as possible by simultaneously evolving them and controlling individual phase accumulation using a tailored spin-echo sequence. The generation of the pulse sequence and its efficiency are not trivial in a large system, so we use a computer to find and optimise the pulse sequence. In a sense, this is a quantum-classical hybrid approach where we use a classical computer to efficiently compile the Hamiltonian simulation algorithm to make the most of the quantum hardware, reducing the cost of the spin-echo pulse sequence both in time and pulse counts. Since it relies on classical computers to find the pulse sequence, the extensibility of the protocol ("Number of qubits" in Table 5.1) depends on the trade-off between the computational complexity required for the algorithm to find the optimal pulse sequence ("Complexity" in Table 5.1) and physical resource needed in the quantum hardware ("Total duration" and "Pulse counts" in Table 5.1). The computational complexity of finding the hardware-efficient Hamiltonian rescaling pulse sequence can be saved by using the prior knowledge of the system ("Connectivity" in Table 5.1), which results different compilation strategies (top row of Table 5.1).

In the linear programming approach ("LP" in Table 5.1), we could significantly reduce the total duration $\sum_{i<j} \frac{\theta_{i,j}}{2J_{i,j}}$ of the naive approach to $\max\{\frac{\theta_{i,j}}{2J_{i,j}}\}$, which at most reduces the total duration by a factor of q^2, where q is the number of qubits. This was made possible by allowing simultaneous time-evolution of many two-qubit interactions and by reformulating the pulse sequence design problem to a linear programming problem. Since it uses a classical computer to find the optimal pulse sequence, the maximum size of the multi-qubit spin-echo sequence is limited to 20 qubits. The maximum size available in this method can be increased to 150 qubits by the randomised method, which is reasonable for all-to-all coupled systems such as trapped-ions [9]. Still, the computer-based approach is ultimately limited by the inability of simulating a quantum system using classical computers.

Further improvement in the extensibility could be achieved by customising the decoupling strategy for sparsely-coupled qubits, giving up the general strategy for the all-to-all coupling network. In particular, we have considered the nearest-neighbour coupling network, which is common in superconducting circuits, and showed its scalability to billions of qubits. The most crucial result is its scaling of the pulse counts to the number of qubits. In the error-bounded case ("Colouring*" in Table 5.1), the number of pulses does not scale with the number of qubits, which means pulses will not be crowded even as we increase the number of qubits indefinitely. This gives us the benefit of having the duty cycle constant even we increase the number of qubits, which is also critical for alleviating the heating problem in quantum computers.

Chapter 6

Strongly coupled transmon qubits

The previous chapter described how spin-echo techniques could be potentially combined with single-qubit control to compile quantum algorithms hardware efficiently in quantum systems with always-on interactions. This chapter investigates the issues that arise when we attempt to implement such techniques in real superconducting circuits. Specifically, we will look at systematic errors due to reduced readout addressability and dressed qubit evolution.

In the first half of this chapter, we introduce the practical issues in operating always-on coupled qubits and the experimental protocols we have developed to control and characterise strongly coupled qubits. Using measurement and controlling techniques that take the strong coupling effect into account, we have discovered a unique problem in strongly-coupled qubits, which was crucial for discussing the future scaling of the quantum computing architecture using always-on coupling in superconducting qubits. In the latter half of this chapter, we show our analysis of the potential problem and show a theoretical prediction of the future development of quantum computing using native interaction.

6.1 Experimental techniques for strongly coupled transmon qubits

To investigate the strong residual interaction for quantum computing, we tested a pair of qubits in device 4Q3 that had a strong residual coupling strength of $\zeta/2\pi =$ 3.9 MHz. Since the standard dispersive readout and the single-qubit gate tune-up introduced in Chapter 3 do not take the strong coupling into account, we have developed specialised measurement techniques that overcome the unusual systematic errors due to the strong coupling.

6.1.1 Joint dispersive readout

In a typical quantum processor based on circuit QED, a qubit is coupled to a dedicated resonator to read out the qubit's state independently. Each resonator is designed to couple one qubit and is supposed to read out the qubit's state isolated from other qubits. This is the same for the coaxmon architecture, where we assume each resonator coupling to a qubit in the same unit cell, being well isolated from nearby qubits. As the qubit-qubit coupling increases, the indirect coupling of a resonator to nearby qubit increases, and the resonator's response reflects multiple qubits' state. In order to correctly interpret the response of the readout resonators, we must take into account the fact that they jointly measure two qubits simultaneously [113, 114]. In this section, we introduce the joint readout method to investigate the systematic readout error in a strongly coupled two-coaxmon system and show the process of correcting the measurement error by post processing the experimental results.

6.1.2 Analysing joint readout in the IQ plane

As we introduced in Sec. 3.1.3, a qubit's state can be determined by the in-phase and the quadrature-phase voltage of the readout resonator's response, and the ground and the excited states of the qubit correspond to two different points on the IQ plane. However, when a resonator is coupled to two qubits, the dispersive shifts by both qubits affect the resonator response, and we can distinguish four two-qubit basis states $|00\rangle$, $|01\rangle$, $|10\rangle$ and $|11\rangle$ on the IQ plane (see Fig. 6.1).

Similar to the standard averaged measurement protocol, we set a reference axis by fitting a line to the four basis points in each IQ plane as indicated by black dashed lines in Fig. 6.1. Measured points in each IQ plane are projected to the reference axes, and the ensemble average and their correlation can be described as weighted

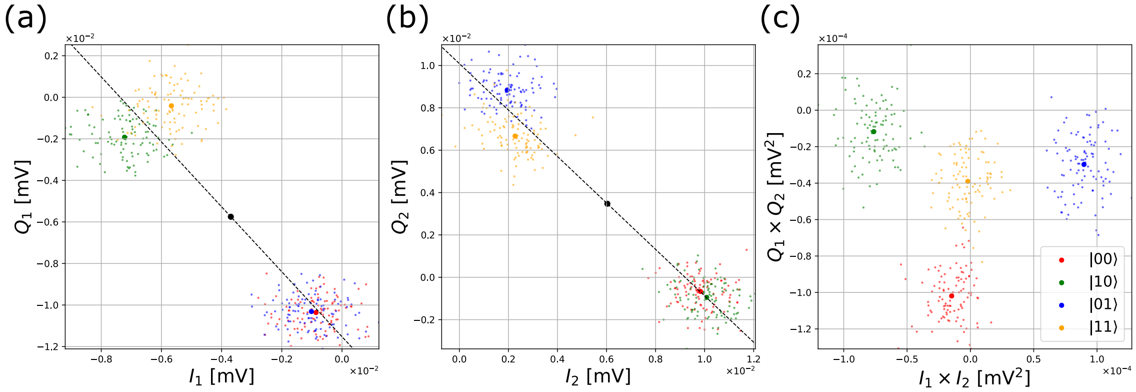

Figure 6.1: Experimental result of jointly reading out four basis states $|00\rangle$, $|01\rangle$, $|10\rangle$ and $|11\rangle$ on the IQ plane. Each state was prepared for 10000 times and we measured them by two resonators coupled to (a) the first qubit and (b) the second qubit. Small points represent the average of 100 shots and large points represent the average of all shots. (c) shows the correlation of the measurement results defined by the product of the in-phase and the quadrature-phase results of the first and the second resonator.

sums of the two qubit population and their correlation as follows,

$$\begin{aligned}
\langle \hat{V}^{(1)} \rangle = \langle \psi | \hat{V}^{(1)} | \psi \rangle &= \beta^{(1)}_{II} + \beta^{(1)}_{ZI} \langle \widetilde{ZI} \rangle + \beta^{(1)}_{IZ} \langle \widetilde{IZ} \rangle + \beta^{(1)}_{ZZ} \langle \widetilde{ZZ} \rangle , & (6.1) \\
\langle \hat{V}^{(2)} \rangle = \langle \psi | \hat{V}^{(2)} | \psi \rangle &= \beta^{(2)}_{II} + \beta^{(2)}_{ZI} \langle \widetilde{ZI} \rangle + \beta^{(2)}_{IZ} \langle \widetilde{IZ} \rangle + \beta^{(2)}_{ZZ} \langle \widetilde{ZZ} \rangle , & (6.2) \\
\langle \hat{V}^{(c)} \rangle = \langle \psi | \hat{V}^{(1)} \cdot \hat{V}^{(2)} | \psi \rangle &= \beta^{(c)}_{II} + \beta^{(c)}_{ZI} \langle \widetilde{ZI} \rangle + \beta^{(c)}_{IZ} \langle \widetilde{IZ} \rangle + \beta^{(c)}_{ZZ} \langle \widetilde{ZZ} \rangle , & (6.3)
\end{aligned}$$

where $\beta^{(i)}_{II}$, $\beta^{(i)}_{ZI}$, $\beta^{(i)}_{IZ}$ and $\beta^{(i)}_{ZZ}$ $(i = 1, 2, c)$ are coefficients obtained from calibration experiments implemented as follows.

First, we prepare four basis states $|00\rangle$, $|01\rangle$, $|10\rangle$ and $|11\rangle$, and record the averaged voltage projected to the reference axis (blacked dashed line), which are described as $\langle \hat{V}^{(i)}_{00} \rangle$, $\langle \hat{V}^{(i)}_{01} \rangle$, $\langle \hat{V}^{(i)}_{10} \rangle$ and $\langle \hat{V}^{(i)}_{11} \rangle$. Assuming that we prepared the basis states perfectly, the measured voltages satisfy the following linear equations,

$$\begin{aligned}
\langle \hat{V}^{(i)}_{00} \rangle &= \langle 00 | \hat{V}^{(i)} | 00 \rangle = \beta^{(i)}_{II} + \beta^{(i)}_{ZI} + \beta^{(i)}_{IZ} + \beta^{(i)}_{ZZ}, & (6.4) \\
\langle \hat{V}^{(i)}_{01} \rangle &= \langle 01 | \hat{V}^{(i)} | 01 \rangle = \beta^{(i)}_{II} + \beta^{(i)}_{ZI} - \beta^{(i)}_{IZ} - \beta^{(i)}_{ZZ}, & (6.5) \\
\langle \hat{V}^{(i)}_{10} \rangle &= \langle 10 | \hat{V}^{(i)} | 10 \rangle = \beta^{(i)}_{II} - \beta^{(i)}_{ZI} + \beta^{(i)}_{IZ} - \beta^{(i)}_{ZZ}, & (6.6) \\
\langle \hat{V}^{(i)}_{11} \rangle &= \langle 11 | \hat{V}^{(i)} | 11 \rangle = \beta^{(i)}_{II} - \beta^{(i)}_{ZI} - \beta^{(i)}_{IZ} + \beta^{(i)}_{ZZ}. & (6.7)
\end{aligned}$$

where $\beta^{(i)}_{II}$, $\beta^{(i)}_{ZI}$, $\beta^{(i)}_{IZ}$ and $\beta^{(i)}_{ZZ}$ $(i = 1, 2, c)$ can be obtained by solving the linear equation.

In the previous studies [113, 114], only one resonator was used to measure the two-qubit state, meaning only resonator response, $\langle \hat{V}^{(1)} \rangle$ or $\langle \hat{V}^{(2)} \rangle$ of Eq. (6.1) $\sim$ (6.3) was available in one experimental run. Therefore, to estimate $\langle \widetilde{ZI} \rangle$, $\langle \widetilde{IZ} \rangle$ and $\langle \widetilde{ZZ} \rangle$, it was necessary to implement three measurements of the same state, each applying pre-rotations of $\hat{I} \otimes \hat{I}$, $\hat{X} \otimes \hat{I}$ and $\hat{I} \otimes \hat{X}$ as follows,

$$\langle \hat{V} \rangle_{II} = \langle \psi | \, (\hat{I} \otimes \hat{I}) \hat{V} (\hat{I} \otimes \hat{I}) \, | \psi \rangle = \beta_{II} + \beta_{ZI} \langle \widetilde{ZI} \rangle + \beta_{IZ} \langle \widetilde{IZ} \rangle + \beta_{ZZ} \langle \widetilde{ZZ} \rangle \, , \tag{6.8}$$

$$\langle \hat{V} \rangle_{XI} = \langle \psi | \, (\hat{X} \otimes \hat{I}) \hat{V} (\hat{X} \otimes \hat{I}) \, | \psi \rangle = \beta_{II} - \beta_{ZI} \langle \widetilde{ZI} \rangle + \beta_{IZ} \langle \widetilde{IZ} \rangle - \beta_{ZZ} \langle \widetilde{ZZ} \rangle \, , \tag{6.9}$$

$$\langle \hat{V} \rangle_{IX} = \langle \psi | \, (\hat{I} \otimes \hat{X}) \hat{V} (\hat{I} \otimes \hat{X}) \, | \psi \rangle = \beta_{II} + \beta_{ZI} \langle \widetilde{ZI} \rangle - \beta_{IZ} \langle \widetilde{IZ} \rangle - \beta_{ZZ} \langle \widetilde{ZZ} \rangle \, , \tag{6.10}$$

and solve the linear equation using the measured voltages $\langle \hat{V} \rangle_{II}$, $\langle \hat{V} \rangle_{XI}$ and $\langle \hat{V} \rangle_{IX}$.

However, by having two resonator responses $\langle \hat{V}^{(1)} \rangle$ and $\langle \hat{V}^{(2)} \rangle$ and the expectation value of their correlation $\langle \hat{V}^{(c)} \rangle$, we can reconstruct $\langle \widetilde{ZI} \rangle$, $\langle \widetilde{IZ} \rangle$ and $\langle \widetilde{ZZ} \rangle$ using results of a single experimental run and solving the linear equation of Eq. (6.1) $\sim$ (6.3).

6.1.3 Readout pulse calibration

With the ability to quantify the jointness of the readout by β coefficients, we aim to minimise the jointness by tuning the readout pulse parameters. Since β coefficients are experimentally determined by resonator responses, they depend on the physical readout pulse parameters such as the drive frequency, pulse amplitude and duration. Fig. 6.2 shows the measured β coefficients swept by various readout pulse parameters. We can see that $\beta_{ZI}(\beta_{IZ})$ is the dominant factor in the response of the resonator 1 (2) and magnitudes of other coefficients indicate the effect from the other qubit. Therefore, ratios β_{IZ}/β_{ZI} (β_{ZI}/β_{IZ}) and $\beta_{IZ}/\beta_{ZI}(\beta_{ZZ}/\beta_{IZ})$ indicate the readout errors of resonator 1 (2) affected by the nearby qubit and we choose the readout pulse parameters that minimise these ratios while maximising the signal-to-noise ratio. For example, in the case of the first qubit of device 4Q3 (left side of Fig. 6.3), we choose the readout drive frequency of 10.834GHz, which has maximal SNR while having small β_{IZ}/β_{ZI} and β_{ZZ}/β_{ZI} (dashed gray line in Fig. 6.3). As for the readout pulse amplitude, the SNR and the jointness increases monotonically in the weak

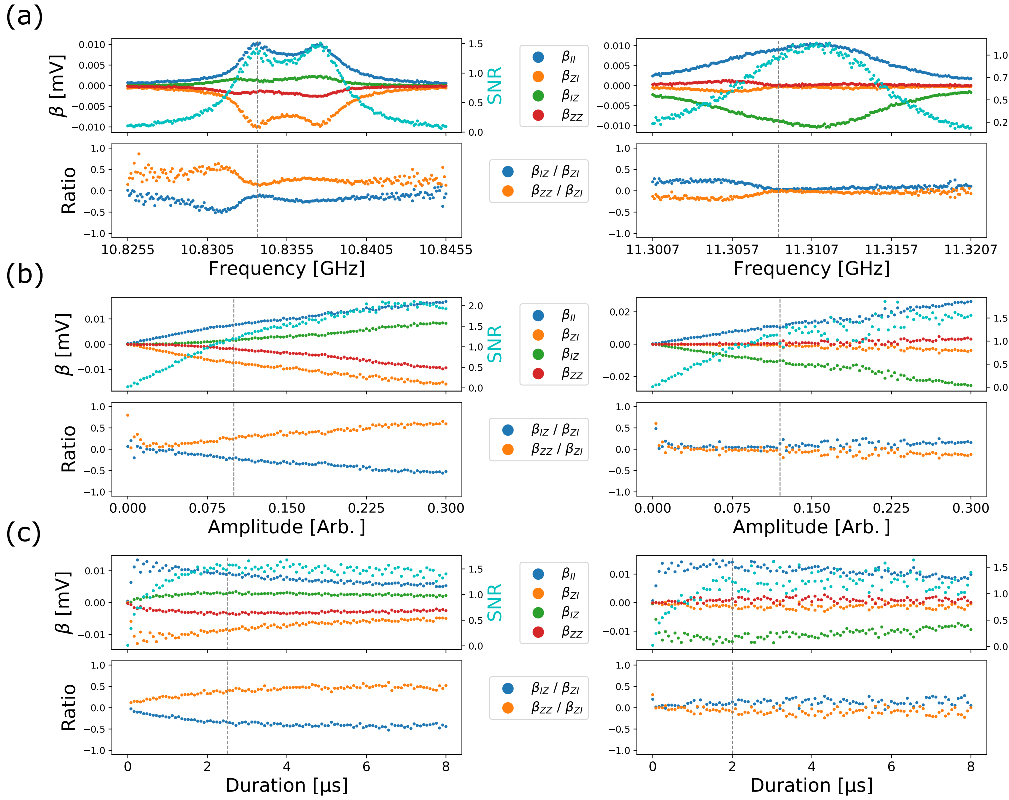

Figure 6.2: Readout pulse calibration taking the jointness of the readout into account. Drive frequency (a), pulse amplitude (b) and pulse duration (c) are swept to find the optimal readout pulse parameters. Left (right) column shows the result from the resonator coupled to the first (second) qubit of device 4Q3. The upper graph of each parameter shows the actual values of the β parameters and the second graph shows the ratio of the residual readout errors to the desired signal.

drive regime, and we choose the pulse amplitude in this regime because the resonator response gets complicated if we put too much power. Typically, we choose the drive amplitude where the increase of the SNR with the pulse amplitude gets gentler than the increase of β_{IZ}/β_{ZI} and β_{ZZ}/β_{ZI}. Regarding the readout pulse duration, the SNR decreases after it reaches its peak around $1 \sim 2$ μs, so we set the duration at the peak.

6.1.4 Joint state tomography

Having all coefficients $\beta_{II}^{(i)}$, $\beta_{ZI}^{(i)}$, $\beta_{IZ}^{(i)}$ and $\beta_{ZZ}^{(i)}$ $(i = 1, 2, c)$, we can estimate the two-qubit pseudo-population $\langle \tilde{ZI} \rangle$, $\langle \widetilde{IZ} \rangle$ and the correlation $\langle \widetilde{ZZ} \rangle$ of an unknown quantum state using Eq. (6.1),(6.2) and (6.3). For example, measured IQ voltages in Fig. 6.1 can be transformed to $\langle \widetilde{ZI} \rangle$ and $\langle \widetilde{IZ} \rangle$ using $\beta^{(1)}$ and $\beta^{(2)}$, which are shown in Fig. 6.3. Here we normalise the results assuming perfect preparation of the basis states, and in future when single-shot readout works, this would no longer be needed.

To fully understand the behaviour of the two-qubit state, the expectation values of two-qubit Pauli operators required for the full two-qubit state tomography can be obtained by applying basis transformation ($\hat{X}_{-\frac{\pi}{2}}$ and $\hat{Y}_{\frac{\pi}{2}}$) before the readout. Fig. 6.4 shows the quantum state tomography of the two-qubit state during a Ramsey

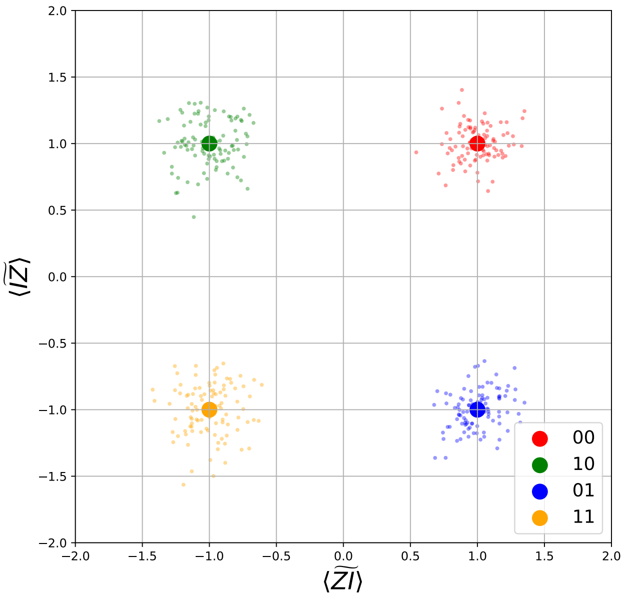

Figure 6.3: Measurement results of single-qubit Pauli operators $\langle \widetilde{ZI} \rangle$ and $\langle \widetilde{IZ} \rangle$ after the joint-readout correction. Red, green, blue and yellow points indicate experimental runs prepared in $|00\rangle$, $|01\rangle$, $|10\rangle$ and $|11\rangle$. Data points used in this figure are transformed from the In-phase and Quadrature-phase voltages displayed in Fig. 6.1.

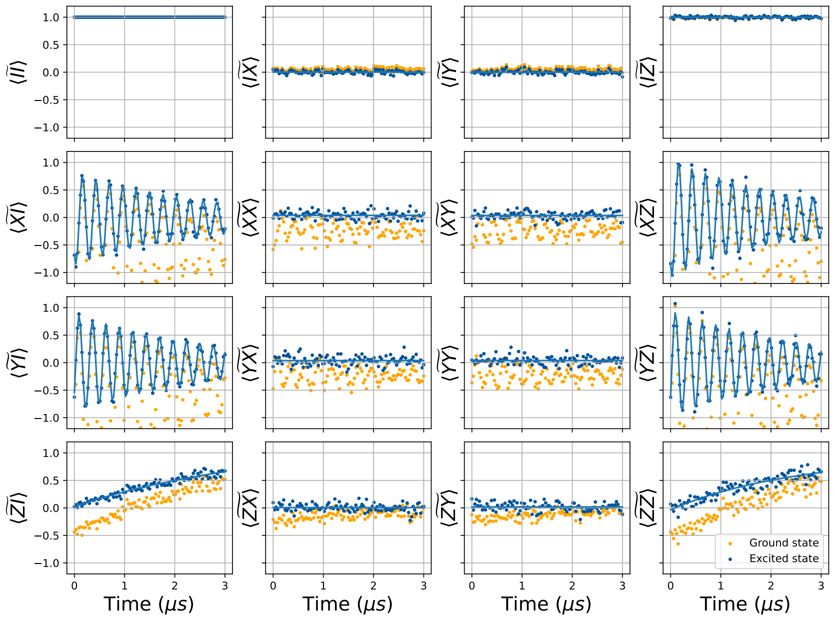

Figure 6.4: Joint quantum state tomography of a Ramsey interferometry experiment on the first qubit. Without the joint-readout correction (orange), some data points go outside the computational subspace, which are unphysical. Blue points are post-processed data after the joint-readout correction.

interferometry experiment on the first qubit. The quantum state tomography without the joint readout correction, indicated by orange points, have large deviation from the expected Ramsey oscillation, where data points in $\langle \widetilde{XI} \rangle$, $\langle \widetilde{YI} \rangle$, $\langle \widetilde{XZ} \rangle$ and $\langle \widetilde{YZ} \rangle$ oscillate outside the computational subspace (see Fig. 6.5). Moreover, the length of the two-qubit Bloch vector defined by the square sum of each Pauli expectation values, $|\vec{B}_v| = \frac{1}{4}\sum_{i,j} |\langle \widetilde{P_i \otimes P_j} \rangle|$, $(P_i, P_j = I, X, Y, Z)$ exceeds $|\vec{B}_v| = 1$, which indicates that the joint-readout correction is necessary for avoiding unphysical results. With the help from post-processing, these nonidiealities in measurements could be suppressed (blue points in Fig. 6.4 and 6.5), so we have applied the joint-readout correction protocol for all remaining measurements on device 4Q3 displayed in this chapter

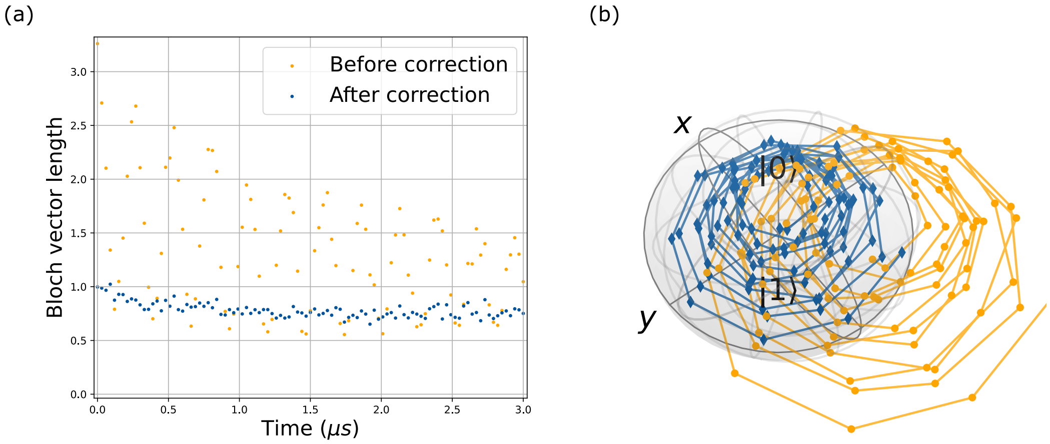

Figure 6.5: Different representations of the Ramsey interferometry experiment on the first qubit of device 4Q3. (a) The Bloch vector of the two qubit state and (b) a trace of the Ramsey oscillation on the first qubit's Bloch sphere. Both the one-qubit and the two-qubit Bloch vector representation show the overshoot of the measurement result without the joint-readout correction (orange points) and the post-processing mitigates the readout error.

6.2 Single-qubit gate calibration

In the previous section, we have seen how the strong always-on qubit-qubit coupling affected the qubit readout and introduced the post-processing technique to correct the systematic error. In this section, we discuss how the qubit control is influenced by the always-on coupling and introduce our tune-up strategy to calibrate single-qubit gates in the presence of a strong static coupling.

When the qubit-qubit coupling is not negligible, the dynamics of a qubit depends on the coupled qubit's state. Crucially, the optimal pulse parameters depend on the neighbouring qubit's state since the qubit's resonant frequency changes due to the ZZ coupling. In the following subsections, we discuss the effect of the always-on coupling when we optimise control pulse parameters.

6.2.1 State-dependent optimal pulse parameters

As we have dicussed in Chapter 3, the half-DRAG pulse is responsible for minimising leakage and detuning errors. In the always-on Ising coupled system, the resonant frequency of a qubit depends on the coupled qubit's state, so the detuning of the microwave drive from the qubit's frequency is dependent on the state of the other qubit. This makes the optimal DRAG coefficient different depending on the coupled qubit's state and we need to take this effect into account when we calibrate single-qubit gates.

Fig. 6.6 shows the experimental result of the DRAG coefficient tune-up conditioned on the state of the neighbouring qubit. The upper figure shows the result of the DRAG coefficient calibration when the coupled qubit was in the ground state, and the lower figure shows the result when the other qubit was in the excited state. The optimal DRAG coefficient were 0.0024 (0.0103) when the coupled qubit was in the ground (excited) state, and we can see that the optimal DRAG coefficient of each case is far from the optimum in the other case.

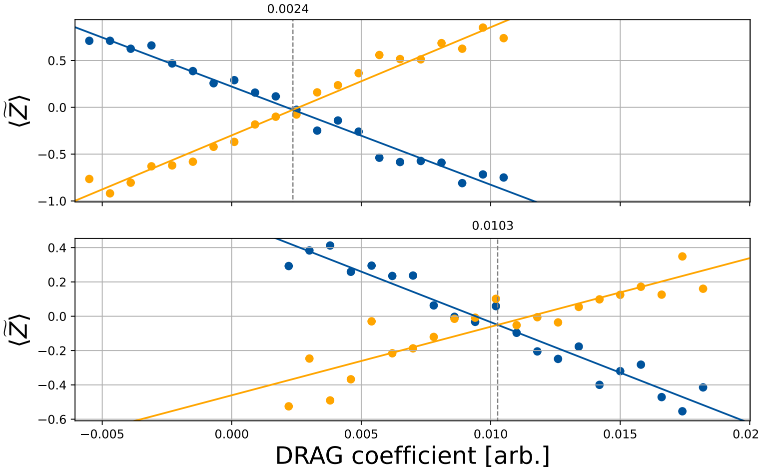

Figure 6.6: DRAG coefficient calibration when the neighbouring qubit is in the ground (upper plot) or the excited (lower plot) state. The colour of the data points and the fitting function for the DRAG coefficient calibration are introduced in Sec. 3.2.4.

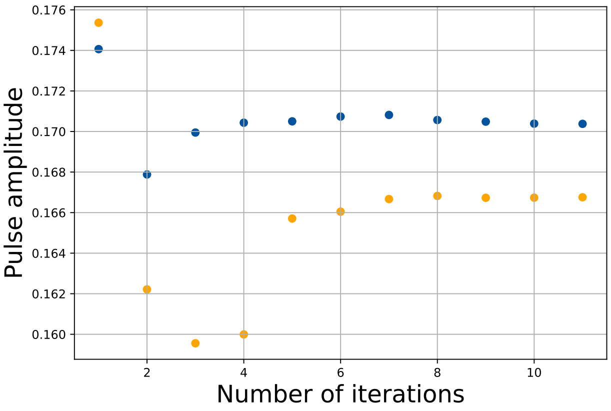

Figure 6.7: The optimal pulse amplitude obtained by iterating the ping-pong tune-up when the neighbouring qubit was in the ground (blue) or the excited states (orange).

Similarly, the pulse amplitude converges to different optimal value depending on the state of the neighbouring qubit. For example, in one instance of the ping-pong calibration, the pulse amplitude converged to 0.167 (0.170) when the other qubit was in the ground (excited) state as shown in Fig. 6.7.

6.2.2 State-dependent tune-up

The fact that the optimal pulse parameters depend on the neighbouring qubit's state gives us another complexity in our calibration routine and it limits the average single-qubit gate fidelity in general quantum algorithms.

However, if we know the state of the qubits before we apply the pulse, we can choose the calibrated pulse parameters depending on the qubits' state. For example, when we implement the state-dependent Ramsey experiment, we apply the gate sequence as follows,

$$\begin{array}{lcl}
\text{Initialise in } |00\rangle & - & \hat{I}\otimes\hat{X}^{(g)}_{\pi} - \hat{X}^{(e)}_{\frac{\pi}{2}}\otimes\hat{I} - \text{wait} - \hat{X}^{(e)}_{-\frac{\pi}{2}}\otimes\hat{I} - \text{measure} \\
\text{Initialise in } |00\rangle & - & \quad \hat{I}\otimes\hat{I} \quad - \hat{X}^{(g)}_{\frac{\pi}{2}}\otimes\hat{I} - \text{wait} - \hat{X}^{(g)}_{-\frac{\pi}{2}}\otimes\hat{I} - \text{measure}
\end{array}$$

In this case, we assume that the second qubit is in the ground or the excited state while we are implementing the Ramsey interferometry experiment on the first qubit. $\hat{X}_{\pi}^{(g)}$ ($\hat{X}_{\pi}^{(e)}$) is a $\hat{X}_{\pi}$ pulse using pulse parameters that are calibrated when the other qubit was in the ground (excited) state. Experiments with a small number of gates or first few gates in quantum algorithms are fine with this approach, so we have used this calibration method when we implemented a careful analysis of a Ramsey experiment in the next section.

Nevertheless, we usually do not know the qubits' state during general quantum algorithms run, so the biased calibration might lead to additional error. Therefore, when the qubit state is arbitrary, we set the pulse parameters to the average value of the calibrated result in each configuration to minimise the gate error on average. Although single-qubit gates produced by the above-mentioned calibration protocol have non-negligible rotation errors, to the best of our knowledge, this is the best approach of tuning up single-qubit gates with a simple waveform under always-on coupling.

In future, we could improve the average single-qubit gate fidelity using advanced pulse shaping techniques such as numerically optimised pulses [74] and analytical dynamically corrected gates [89], which can take the effect of the always-on coupling into account during single-qubit gates.

6.3 Deviation from pure Ising interaction

With specialised measurement and control techniques, we have investigated the evolution of a strongly-coupled two-transmon system in detail.

Initially, we expected that the residual interactions in the capacitively coupled transmon qubits generate pure Ising interactions. However, in the case of device

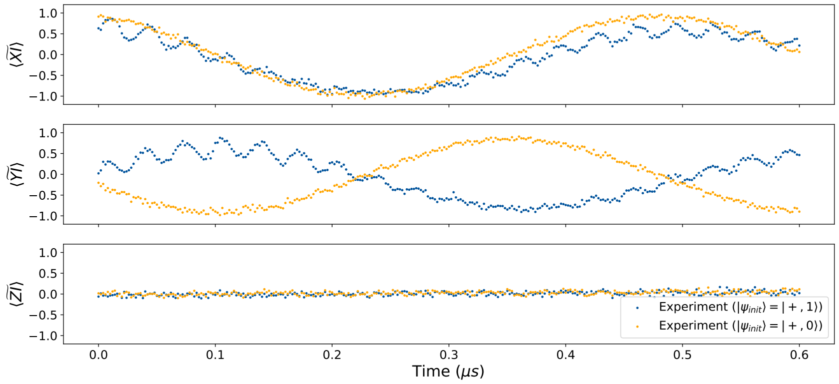

Figure 6.8: Fast oscillation in the strongly-coupled two-qubit dynamics. The graph shows the quantum state tomography of the Ramsey interferometry experiment on the first qubit. Orange (blue) points is the result when the second qubit was in the ground (excited) state and they are post-processed taking the effect of the jointness of the readout into account.

4Q3, we have observed two-qubit dynamics that could not be explained solely by the Ising interaction. Fig. 6.8 shows the result of the Ramsey interferometry experiment on the first qubit when the second qubit was in the ground state (orange points) or the excited state (blue points). As we can see from the plot, there is a high frequency component in addition to the oscillation caused by the Ising interaction.

To understand the origin of the extra oscillation, we have simulated the same Ramsey experiment on a computer. In the simulation, we modelled the system by the following Hamiltonian and simulated the time evolution after preparing the two-qubit state to $|+,0\rangle$ (orange) and $|+,1\rangle$ (blue),

$$\hat{\mathcal{H}}/\hbar = \sum_{i=1,2} (\omega_i \hat{a}_i^\dagger \hat{a}_i + \frac{\alpha_i}{2} \hat{a}_i^\dagger \hat{a}_i^\dagger \hat{a}_i \hat{a}_i) + J(\hat{a}_1^\dagger \hat{a}_2 + \hat{a}_1 \hat{a}_2^\dagger), \tag{6.11}$$

where annihilation operator $\hat{a}_i$ is truncated to three levels. We have used the physical parameters of device 4Q3 for ω_i, α_i (i=1,2) in the Hamiltonian to model the exact dynamics in the experiment (see Appendix A.1 for the device parameters). The coupling strength J in the simulation was adjusted to be the value that makes the simulated Ising evolution (slower oscillation frequency) close to the experimental result.

In the aim of characterising the fast oscillation by available device parameters, we have derived the time evolution analytically using perturbation theory. The time evolution of the two-qubit state under Eq. (6.11) can be described as follows,

$$\begin{aligned} |\psi(t)\rangle &= \exp\left(-\frac{i\hat{\mathcal{H}}t}{\hbar}\right)|\psi(0)\rangle = \hat{P}^{\dagger}\exp\left(-\frac{i\hat{\mathcal{H}}_D t}{\hbar}\right)\hat{P}\,|\psi(0)\rangle \\ &\approx \hat{P}^{(2)\dagger}\exp\left(-\frac{i\hat{\mathcal{H}}_D^{(2)}t}{\hbar}\right)\hat{P}^{(2)}\,|\psi(0)\rangle = \hat{U}^{(2)}(t)\,|\psi(0)\rangle = |\psi^{(2)}(t)\rangle\,, \quad (6.12) \end{aligned}$$

where $\hat{\mathcal{H}_D}$ is the diagonalised Hamiltonian of $\hat{\mathcal{H}}$, and $\hat{P}$ is an invertible matrix that is made up of eigenvectors of $\hat{\mathcal{H}}$. To give the analytical expression of the time evolution, we have derived the diagonalised Hamiltonian using the perturbation theory to the second order instead of numerically diagonalising the Hamiltonian (see Appendix A.6 for the detailed derivation and the analytical expression of $\hat{\mathcal{H}}_D^{(2)}$ and $\hat{P}^{(2)}$).

The quantum state tomography of a time evolution of the first qubit can be reproduced by solving the Schrödinger equation for the two-qubit system and calculating the expectation values of measurement operators $\hat{\sigma}\otimes\hat{I}$ ($\hat{\sigma}=\hat{X},\hat{Y},\hat{Z}$) in the rotating frame of both qubits,

$$\begin{aligned} \langle\hat{\sigma}\otimes\hat{I}\rangle^{(2)}(t) &= \langle\psi^{(2)}(t)|\,\hat{U}_{rot}^{(2)}(t)(\hat{\sigma}\otimes\hat{I})\hat{U}_{rot}^{(2)\dagger}(t)\,|\psi^{(2)}(t)\rangle & (6.13) \\ &= \langle\psi(0)|\,\hat{U}^{(2)'\dagger}(t)(\hat{\sigma}\otimes\hat{I})\hat{U}^{(2)'}(t)\,|\psi(0)\rangle\,, & (6.14) \\ \hat{U}_{rot}^{(2)}(t) &= \exp\left(-i\frac{\omega_{10}^{(2)}t}{2}\hat{Z}\hat{I}-i\frac{\omega_{01}^{(2)}t}{2}\hat{I}\hat{Z}\right), & (6.15) \end{aligned}$$

where $\hat{U}^{(2)'}(t)=\hat{U}_{rot}^{(2)\dagger}(t)\hat{U}^{(2)}(t)$, $\hbar\omega_{mn}^{(2)}=\langle m,n|\,\hat{\mathcal{H}}_D^{(2)}\,|m,n\rangle$. To reproduce the state dependent Ramsey oscillation experiment on the first qubit, we set the initial state as $|\psi(0)\rangle = |+,0\rangle$ or $|+,1\rangle$ and calculated the following for $\hat{\sigma} = \hat{X}, \hat{Y}, \hat{Z}$,

$$\begin{aligned} \langle \hat{\sigma} \otimes \hat{I} \rangle_g^{(2)}(t) &= \langle +,0| \hat{U}^{(2)'\dagger}(t)(\hat{\sigma} \otimes \hat{I})\hat{U}^{(2)'}(t) |+,0\rangle, & (6.16) \\ \langle \hat{\sigma} \otimes \hat{I} \rangle_e^{(2)}(t) &= \langle +,1| \hat{U}^{(2)'\dagger}(t)(\hat{\sigma} \otimes \hat{I})\hat{U}^{(2)'}(t) |+,1\rangle. & (6.17) \end{aligned}$$

The exact solution according to the second-order perturbation theory has many terms that are not relevant in the discussion, so we will only introduce the approximated form in this section (see Appendix A.6 for the full analytical expression). In the case where the detuning is close to the anharmonicity of the first qubit, we can approximate the time evolution as follows,

$$\begin{aligned} \langle \hat{X} \otimes \hat{I} \rangle_g^{(2)}(t) &\approx \cos^2\theta \cos\frac{\zeta t}{2}, & (6.18) \\ \langle \hat{Y} \otimes \hat{I} \rangle_g^{(2)}(t) &\approx \cos^2\theta \sin\frac{\zeta t}{2}, & (6.19) \\ \langle \hat{Z} \otimes \hat{I} \rangle_g^{(2)}(t) &\approx 0, & (6.20) \\ \langle \hat{X} \otimes \hat{I} \rangle_e^{(2)}(t) &\approx P_{55}^2 \cos^2\theta \cos\left(\frac{\zeta}{2}\right)t \\ &+ P_{75}^2 \cos^2\theta \cos\left(\frac{\zeta}{2} + \omega_{20}^{(2)} - \omega_{11}^{(k)}\right)t, & (6.21) \\ \langle \hat{Y} \otimes \hat{I} \rangle_e^{(2)}(t) &\approx -P_{55}^2 \cos^2\theta \sin\left(\frac{\zeta}{2}\right)t \\ &- P_{75}^2 \cos^2\theta \sin\left(\frac{\zeta}{2} + \omega_{20}^{(2)} - \omega_{11}^{(2)}\right)t, & (6.22) \\ \langle \hat{Z} \otimes \hat{I} \rangle_e^{(2)}(t) &\approx 2P_{55}^2 P_{75}^2 \sin^2\left(\frac{\omega_{20}^{(2)} - \omega_{11}^{(2)}}{2}\right)t, & (6.23) \end{aligned}$$

where $\theta = \arctan\left(\frac{J}{\Delta}\right)$, $\Delta = \omega_{10}^{(0)} - \omega_{01}^{(0)}$, $\zeta = (E_{11}^{(2)} - E_{10}^{(2)} - E_{01}^{(2)})/\hbar$, $\hbar\omega_{mn}^{(0)} = \langle m,n| \hat{\mathcal{H}} |m,n\rangle$ and P_{mn} is the (m,n)th element of the $\hat{P}^{(2)}$ matrix (see Appendix A.6 for the detail),

$$P_{55} = \frac{1}{\sqrt{1+(\frac{\sqrt{2}J}{\Delta-\alpha_2})^2+(\frac{\sqrt{2}J}{\Delta+\alpha_1})^2}}, \tag{6.24}$$

$$P_{75} = -\frac{\sqrt{2}J}{\Delta+\alpha_1}\cdot\frac{1}{\sqrt{1+(\frac{\sqrt{2}J}{\Delta-\alpha_2})^2+(\frac{\sqrt{2}J}{\Delta+\alpha_1})^2}}. \tag{6.25}$$

Using these analytical formulae, we could reproduce the fast oscillation in the Ramsey experiment by simulation, which are plotted in Fig. 6.9. Also, we have confirmed that the approximated result of Eq. (6.20)∼(6.23) are almost the same as the full analytical expression of the second order perturbation, so we will use these formulae for the following analysis.

Since the fast oscillation in the Ramsey experiment could be simulated by the second order perturbation theory, we have considered the origin of the unwanted fast oscillation and its amplitude. Mathematically, the deviation from the ideal Ising evolution originates from the transformation matrix $\hat{P}$ that diagonalises the original Hamiltonian. This can be interpreted as the tilt of the dressed qubit basis from the bare basis becoming non-negligible when the qubit-qubit coupling is strong and the native Hamiltonian evolution producing a fast oscillation around the tilted basis with

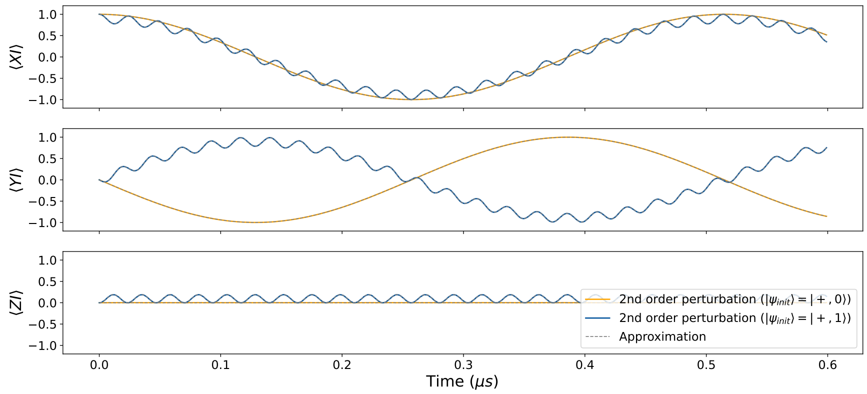

Figure 6.9: Simulation of the fast oscillation in the two-qubit of Eq. (6.20)∼(6.23) matched very well with the exact second-order perturbation result of Eq. (A.29)∼(A.39).

$\omega^{(2)}_{fast}/\hbar = \Delta + \alpha_1 = \frac{\zeta^{(2)}}{2} + \omega^{(2)}_{20} - \omega^{(2)}_{11}$. The amplitude of the faster oscillation is given by Eq. (6.21) and (6.22) which is,

$$\cos^2\theta P^2_{75} = \frac{\Delta}{\sqrt{J^2+\Delta^2}} \cdot \frac{2J^2}{(\Delta+\alpha_1)^2} \cdot \frac{1}{1+(\frac{\sqrt{2}J}{\Delta-\alpha_2})^2+(\frac{\sqrt{2}J}{\Delta+\alpha_1})^2}. \tag{6.26}$$

A factor of $\frac{2J^2}{(\Delta+\alpha_1)^2}$ in Eq. (6.26) explains that the amplitude of the unwanted oscillation becomes large when the detuning and the anharmonicity of the first qubit are close. Therefore, it is better to make $|\Delta + \alpha_1|$ large enough so that the excessive oscillation becomes small. However, the same applies for the second qubit when the detuning is close to the second qubit's anharmonicity, so we need to consider the tilt of the second qubit's dressed basis as well. In the case of $|\Delta - \alpha_2| < |\Delta + \alpha_1|$, the dominant error comes from the second qubit's fast oscillation which is described as the second term of the following,

$$\begin{aligned}
\langle \hat{I} \otimes \hat{X} \rangle^{(2)}_e (t) &\approx P^2_{55}\cos^2\theta\cos\left(\frac{\zeta^{(2)}}{2}\right)t + P^2_{35}\cos^2\theta\cos\left(\frac{\zeta^{(2)}}{2} + \omega^{(2)}_{02} - \omega^{(2)}_{11}\right)t, \\
\langle \hat{I} \otimes \hat{Y} \rangle^{(2)}_e (t) &\approx -P^2_{55}\cos^2\theta\sin\left(\frac{\zeta^{(2)}}{2}\right)t - P^2_{35}\cos^2\theta\sin\left(\frac{\zeta^{(2)}}{2} + \omega^{(2)}_{02} - \omega^{(2)}_{11}\right)t,
\end{aligned}$$

where,

$$\cos^2\theta P^2_{35} = \frac{\Delta}{\sqrt{J^2+\Delta^2}} \cdot \frac{2J^2}{(\Delta-\alpha_2)^2} \cdot \frac{1}{1+(\frac{\sqrt{2}J}{\Delta-\alpha_2})^2+(\frac{\sqrt{2}J}{\Delta+\alpha_1})^2}. \tag{6.27}$$

Ideally, we want to suppress (6.26) and (6.27) at the same rate while making the Ising interaction strong. Although it is possible to set the detuning very large to make $\frac{2J^2}{(\Delta+\alpha_1)^2}$ and $\frac{2J^2}{(\Delta-\alpha_2)^2}$ small, this modification will make the Ising coupling strength $\zeta = -\frac{2J^2(\alpha_1+\alpha_2)}{(\Delta+\alpha_1)(\Delta-\alpha_2)}$ small as well. This leaves us a question of how to choose device parameters such as Δ, α_1 and α_2 that minimise the unwanted fast oscillation while keeping Ising evolution strength. Thanks to formulae (6.26) and (6.27) derived in this section, we are now able to answer this question, and we will give design criteria for future devices in the next section.

6.4 Design criteria for future devices

In the previous section, we have discussed the unwanted two-qubit evolution depending on the device parameters such as Δ, α_1 and α_2. If the qubits' lifetime were infinite, we could design small coupling strength and large detuning to suppress the fast oscillation amplitude to the desired level. However, in reality, qubits' lifetime are finite and we need stronger Ising interaction to minimise incoherent errors. Therefore, it is vital to consider the trade-off between the incoherent errors and the errors due to the tilted bases. The aim of this section is to find the suitable device parameters J and Δ that minimise both incoherent and bases errors, given lifetime τ and qubit anharmonicities α_1 and α_2.

First, we would like to have errors due to the dressed bases of both qubits to be equal so that one of them does not dominate over the other. The condition for the detuning and anharmonicites can be derived by equating unwanted oscillation amplitudes of both qubits formulated by Eq. (6.26) and (6.27),

$$\begin{aligned} P_{35}^2 = P_{75}^2 \;\; &\Leftrightarrow \;\; \left(\frac{\Delta+\alpha_1}{\Delta-\alpha_2}\right)^2 = 1 \\ &\Leftrightarrow \;\; \alpha_1 = -\alpha_2 \text{ or } \Delta = \frac{\alpha_2-\alpha_1}{2}. \end{aligned} \tag{6.28}$$

The former solution makes $\zeta = -\frac{2J^2(\alpha_1+\alpha_2)}{(\Delta+\alpha_1)(\alpha_2-\Delta)} = 0$, so this is not suitable for obtaining the Ising interaction. The latter solution of Eq. (6.28) leads to,

$$\begin{aligned} P_{35}^2 = P_{75}^2 &= \frac{8J^2}{(\alpha_1+\alpha_2)^2+16J^2} && (6.29)\\ \zeta &= -2\pi\frac{8J^2}{\alpha_1+\alpha_2}, && (6.30) \end{aligned}$$

which can be used to estimate the errors for given device parameters.

Incoherent errors can be characterised by a ratio,

$$\epsilon_\tau = \frac{\tau_{ZZ}}{\tau} = \frac{|\alpha_1+\alpha_2|}{8J^2\tau}, \tag{6.31}$$

where τ is the lifetime of qubits and $\tau_{ZZ} = |\frac{2\pi}{\zeta}|$ is the time it takes for the Ising interaction to evolve full rotation. On the other hand, the errors due to the qubit-qubit dressing can be quantified as (see Appendix A.7 for the detail),

$$\epsilon_d = 1-\cos^2\theta P_{55} \approx \frac{J^2}{\Delta^2}+\frac{16J^2}{(\alpha_1+\alpha_2)^2}, \tag{6.32}$$

where $\theta = \arctan\left(\frac{J}{\Delta}\right)$ and P_{55} is taken from Eq (6.24). In the ideal scenario, we do not want to have either of ϵ_τ and ϵ_d dominate the other,

$$\begin{aligned} \epsilon_\tau = \epsilon_d \;\Leftrightarrow\; & -\frac{\alpha_1+\alpha_2}{8J^2\tau} \approx \frac{J^2}{\Delta^2}+\frac{16J^2}{(\alpha_1+\alpha_2)^2} && (6.33)\\ \therefore\;\; & J^2 \approx \frac{|\alpha_1^2-\alpha_2^2|}{16\sqrt{\tau}}\cdot\sqrt{\frac{|\alpha_1+\alpha_2|}{5\alpha_1^2-6\alpha_1\alpha_2+5\alpha_2^2}} && (6.34) \end{aligned}$$

therefore,

$$\zeta = -\frac{2\pi(\alpha_1-\alpha_2)}{2\sqrt{\tau}}\cdot\sqrt{\frac{|\alpha_1+\alpha_2|}{5\alpha_1^2-6\alpha_1\alpha_2+5\alpha_2^2}} \tag{6.35}$$

is the optimal Ising interaction for given lifetime τ and target anharmonicities. Importantly, the Ising coupling strength should be decreased quadratically as the lifetime gets longer to balance the incoherent error and the error from the qubit-qubit dressing. Using these formulae, we have plotted the expected errors given lifetime and realistic device parameters in Fig. 6.10.

This analysis can provide design criteria for optimal performance of always-on Ising-coupled transmon devices and predicts that we should be able to achieve error levels of $1.0 \times 10^{-2} \sim 5.0 \times 10^{-3}$ with current state-of-the art coherence of 100 μs $\sim$ 1000 μs. It remains to be seen whether this scheme can compete with conventional gate-based approach using cross resonance gates in a similar architecture using fixed-frequency and fixed-coupling circuits. Further work on error correction with always-on coupling will be necessary in order to realise the fault-tolerance [41, 109, 110]. The surface code error correction would be the suitable candidate for this architecture because it only requires nearest-neighbour interactions and local operations in the error correcting syndrome [115, 116, 117].

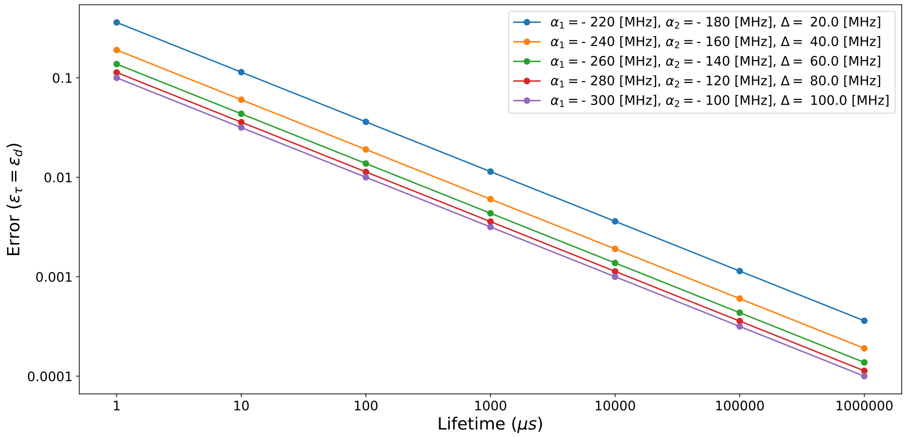

Figure 6.10: Expected errors given lifetime and device parameters such as anharmonicities and qubit-qubit detuning. Here, we plotted the result of the ideal scenario, where the incoherent error and the qubit-qubit dressing error are equall.

Chapter 7

Conclusion and outlook

7.1 Conclusion

This thesis introduced a novel spin-echo-based quantum computing strategy using always-on coupling and presented a detailed analysis for future scaling. Remarkably, the Hamiltonian rescaling protocol enabled the hardware-efficient native interactions to be programmable in an efficient time. This result inspired a pragmatic approach to utilise residual couplings in superconducting circuits as computational resources instead of treating them as error sources.

Chapter 4 showed the proof-of-principle experiment of the variational quantum eigensolver (VQE) and the error mitigation using the always-on coupled transmons. The trial wave function of the VQE was encoded straightforwardly by timings of spin-echo pulses in a hardware-efficient manner. Moreover, the magnitude of the artificial noise in the zero-noise extrapolation could be selected continuously without extra calibration of two-qubit interaction, which reduced the error mitigation experimental costs. Lastly, the idea of the hardware compilation of variational quantum algorithms inspired the discovery of the general hardware-efficient compilation scheme based on spin-echo sequences.

In Chapter 5, we have introduced the general Hamiltonian rescaling protocol using novel spin-echo techniques. In this paradigm, we encode quantum algorithms by timings of spin-echo pulses, and we have developed two distinct methods to rescale Hamiltonians. The first algorithm optimises a pulse sequence to rescale all-to-all coupled Hamiltonian using linear programming, which minimises the total duration of the pulse sequence. Although the optimisation by linear programming only allows pulse sequences for up to 20 qubits, randomised protocol extends the limit to hundreds of qubits, giving a near time-optimal pulse sequence. We have estimated the physical resource needed for this protocol and have seen dramatic reductions in the total duration, time periods and pulse counts compared to the conventional naive approach adopted in NMR [63, 64]. For future applications, the linear programming approach can be applied to various hardware platforms with all-to-all Ising couplings such as NMR and trapped-ions. The second algorithm focused on the extensibility of the Hamiltonian rescaling protocol and we have shown that the pulse generation algorithm based on graph colouring could also find near time-optimal pulse sequences for billions of nearest-neighbour coupled qubits. Notably, the pulse count scales linear to the number of qubits, meaning the number of pulses per qubit stays constant for arbitrary Hamiltonian rescaling. This allows the duty cycle to be constant and low even if we increase the number of qubits.

Chapter 6 investigated the potential limitation of spin-echo based quantum computing to superconducting circuits. By repeating trial-and-error in actual experiments using strongly-coupled transmons, we have addressed potential problems in this architecture such as readout, control and excessive qubit-qubit dressing. The jointness of a two-qubit readout could explain the systematic readout errors in the strongly-coupled transmons, and we could minimise the jointness by optimising measurement pulse parameters. The jointness of the readout could further be calibrated by post-processing, which helped to characterise the two-qubit dynamics in detail. The detailed analysis of the two-qubit dynamics uncovered a potential issue that could be encountered in dispersively coupled qubits. A strong qubit-qubit dressing in the dispersively coupled transmons added unwanted evolution that deviates the free evolution from the ideal Ising Hamiltonian. This was a potential problem for our quantum computing strategy because we have assumed pure Ising Hamiltonian to be rescaled by spin-echoes. Nevertheless, we could explain the origin of the unwanted oscillation and gave analytical formulae that quantify the error. The formulae allowed us to predict qubit-qubit dressing errors given realistic device parameters, and we have laid out the circuit design principles to mitigate the nonidealities for future devices.

7.2 Outlook

In general, quantum computing is aiming to achieve two counteracting objectives. On the one hand, we want to isolate a quantum system from the environment as much as possible to preserve quantum coherence. On the other hand, we desire maximum accessibility to process and read out qubits' state quickly. Simply put, the more control on the qubits we ask, the more disturbance we make in the system. Unlike conventional superconducting quantum computing architectures, our strategy does not rely on externally generated two-qubit gates. Since we use the two-qubit interaction already present in the circuit, potential noise channels from the environment and the total heat flow to the system can be reduced significantly. As discussed in Chapter 5, the duty cycle of the quantum operation can be hugely reduced because we replaced two-qubit gate pulses with the native interaction. In one possible scenario where the limitation of the cooling power inhibits the extension of quantum computers, our approach might become a powerful candidate for future scaling. Already, the current cooling system is known to hold up to only several hundreds of qubits, and the heating problem will be more significant if the qubit's lifetime gets longer. The longer lifetime requires more isolation from the environment, which demands a stronger drive if we mainly use external microwave fields to operate qubits. On the other hand, if we choose the native interaction for entangling operation, we do not need to send strong microwave pulses relentlessly, so the heating problem can be alleviated when we have more qubits with longer qubit lifetime in the future.

Although this thesis aimed to implement spin-echo-based hardware compilation on dispersively coupled transmons lattice, it can be applied to various hardware platforms. The linear programming approach might be useful for the all-to-all Ising couplings in trapped ions, and our algorithms can generate hardware-efficient pulse sequences for a system of hundreds of all-to-all coupled qubits, which are suitable for the near term trapped-ion quantum computers. Another interesting direction is to explore the spin-echo based compilation on bosonic qubits realised by superconducting circuits. The bosonic qubits on superconducting circuits utilise the qubit-cavity dispersive coupling for quantum information processing [19, 118], which is, in a sense, the closest hardware platform to the system studied in this thesis.

As with other quantum computing architectures, we need to keep improving on reducing errors during computation. In addition to the errors discussed in Chapter 6, one of the dominant errors in this architecture is single-qubit errors. Although we have assumed perfect single-qubit operation in developing the spin-echo-based Hamiltonian rescaling, the single-qubit control under the always-on coupled qubits has extra complexity in calibrating gates. Learning from the previous studies in other always-on coupled systems such as NMR and the bosonic qubits [74, 119], numerically optimised pulses might be useful to minimise the effect from the always-on coupling.

We have assumed the Ising interaction for the Hamiltonian rescaling protocol, but it is not confined to limited applications. Diagonal unitaries produced by the Ising Hamiltonian can be directly implemented to subroutines in many useful quantum algorithms such as the quantum Fourier transform [37], the quantum phase estimation, the surface code error syndrome [22, 41], the quantum approximate optimisation algorithm [42] and the variational quantum eigensolver [43]. It would be interesting to know how the Hamiltonian rescaling techniques reduce the computational resources to implement these algorithms. In fact, computer simulations of a similar spin-echo-based compilation scheme of the quantum simulation algorithm and the quantum Fourier transform algorithm have shown better performances than the traditional circuit model compilation [34, 37]. Although their pulse sequence generation protocol does not give general solutions to more than six qubits and does not guarantee the minimum time duration, their results suggest that the spin-echo-based approach might be a promising alternative to the gate-based compilation. As we developed algorithms that produce Hamiltonian rescaling pulse sequences for a large scale qubits network in near-optimal time, it would be worth testing their hardware efficiency in concrete quantum algorithms on larger scale experiments in the future.

Appendix A

Appendix

A.1 Device characteristics

In this section, we summarise the device parameters for qubits used in this thesis.

		2Q1		4Q3	
Parameter	Unit	Q1	Q2	Q1	Q2
$\omega_r/2\pi$	MHz	10503.2	9469.9	10810.7	11275.1
ω_q / 2π	MHz	6623.0	6079.1	6806.7	7118.2
χ / 2π	MHz	2.93	2.62	1.95	2.30
α / 2π	MHz	-299	-310	-322	-294
E_J/h	GHz	22.1	18.4	21.8	25.5
E_C/h	MHz	269.9	276	289	268
E_J/E_C	MHz	81.8	66.5	75.5	95.4
g / 2π	MHz	406.8	331.1	327.5	386.5
T_1	μs	26.19	19.07	6.87	9.38
T_{2E}	μs	21.87	25.59	7.01	8.92
ζ / 2π	MHz	-0.942		-3.908	
J / 2π	MHz	13.56		8.475	

A.2 Clifford gate decomposition

For the randomised benchmarking implemented in this thesis, we used the Clifford decomposition using the physical gates $\hat{X}_{\pi}, \hat{Y}_{\pi}, \hat{X}_{\frac{\pi}{2}}, \hat{Y}_{\frac{\pi}{2}}, \hat{X}_{-\frac{\pi}{2}}, \hat{Y}_{-\frac{\pi}{2}}$ as follows [120].

Clifford gate	Physical gate decomposition
$\hat{C}_1$	$\hat{I}$
$\hat{C}_2$	$\hat{Y}_{\frac{\pi}{2}} \cdot \hat{X}_{\frac{\pi}{2}}$
$\hat{C}_3$	$\hat{X}_{-\frac{\pi}{2}} \cdot \hat{Y}_{-\frac{\pi}{2}}$
$\hat{C}_4$	$\hat{X}_{\pi}$
$\hat{C}_5$	$\hat{Y}_{-\frac{\pi}{2}} \cdot \hat{X}_{-\frac{\pi}{2}}$
$\hat{C}_6$	$\hat{X}_{\frac{\pi}{2}} \cdot \hat{Y}_{-\frac{\pi}{2}}$
$\hat{C}_7$	$\hat{Y}_{\pi}$
$\hat{C}_8$	$\hat{Y}_{-\frac{\pi}{2}} \cdot \hat{X}_{\frac{\pi}{2}}$
$\hat{C}_9$	$\hat{X}_{\frac{\pi}{2}} \cdot \hat{Y}_{\frac{\pi}{2}}$
$\hat{C}_{10}$	$\hat{X}_{\pi} \cdot \hat{Y}_{\pi}$
$\hat{C}_{11}$	$\hat{Y}_{\frac{\pi}{2}} \cdot \hat{X}_{-\frac{\pi}{2}}$
$\hat{C}_{12}$	$\hat{X}_{-\frac{\pi}{2}} \cdot \hat{Y}_{\frac{\pi}{2}}$
$\hat{C}_{13}$	$\hat{Y}_{\frac{\pi}{2}} \cdot \hat{X}_{\pi}$
$\hat{C}_{14}$	$\hat{X}_{-\frac{\pi}{2}}$
$\hat{C}_{15}$	$\hat{X}_{\frac{\pi}{2}} \cdot \hat{Y}_{-\frac{\pi}{2}} \cdot \hat{X}_{-\frac{\pi}{2}}$
$\hat{C}_{16}$	$\hat{Y}_{-\frac{\pi}{2}}$
$\hat{C}_{17}$	$\hat{X}_{\frac{\pi}{2}}$
$\hat{C}_{18}$	$\hat{X}_{\frac{\pi}{2}} \cdot \hat{Y}_{\frac{\pi}{2}} \cdot \hat{X}_{\frac{\pi}{2}}$
$\hat{C}_{19}$	$\hat{Y}_{-\frac{\pi}{2}} \cdot \hat{X}_{\pi}$
$\hat{C}_{20}$	$\hat{X}_{\frac{\pi}{2}} \cdot \hat{Y}_{\pi}$
$\hat{C}_{21}$	$\hat{X}_{\frac{\pi}{2}} \cdot \hat{Y}_{-\frac{\pi}{2}} \cdot \hat{X}_{\frac{\pi}{2}}$
$\hat{C}_{22}$	$\hat{Y}_{\frac{\pi}{2}}$
$\hat{C}_{23}$	$\hat{X}_{-\frac{\pi}{2}} \cdot \hat{Y}_{\pi}$
$\hat{C}_{24}$	$\hat{X}_{\frac{\pi}{2}} \cdot \hat{Y}_{\frac{\pi}{2}} \cdot \hat{X}_{-\frac{\pi}{2}}$

A.3 Coefficients for the VQE

Here we list the Hamiltonian coefficients of Eq. (4.2) used for finding the ground state energy of a Hydrogen molecule by the variational quantum eigensolver (VQE) [30].

Bond distance	g_0	g_1	g_2	g_3	g_4	g_5
0.200000	2.848903	0.567814	-1.450770	0.679939	0.079069	0.079069
0.250000	2.186800	0.544944	-1.286955	0.671920	0.079790	0.079790
0.300000	1.725163	0.521502	-1.145829	0.663088	0.080603	0.080603
0.350000	1.382707	0.498174	-1.022598	0.653652	0.081498	0.081498
0.400000	1.118227	0.475398	-0.914468	0.643787	0.082469	0.082469
0.450000	0.908269	0.453443	-0.819396	0.633633	0.083511	0.083511
0.500000	0.738108	0.432466	-0.735525	0.623305	0.084619	0.084619
0.550000	0.597894	0.412548	-0.661192	0.612892	0.085789	0.085789
0.600000	0.480777	0.393715	-0.594994	0.602464	0.087019	0.087019
0.650000	0.381861	0.375961	-0.535782	0.592079	0.088305	0.088305
0.700000	0.297552	0.359251	-0.482619	0.581783	0.089643	0.089643
0.750000	0.225155	0.343537	-0.434736	0.571613	0.091030	0.091030
0.800000	0.162599	0.328763	-0.391490	0.561599	0.092463	0.092463
0.850000	0.108264	0.314866	-0.352336	0.551767	0.093936	0.093936
0.900000	0.060858	0.301788	-0.316805	0.542134	0.095447	0.095447
0.950000	0.019335	0.289470	-0.284493	0.532716	0.096990	0.096990
1.000000	-0.017158	0.277855	-0.255045	0.523525	0.098562	0.098562
1.050000	-0.049326	0.266891	-0.228156	0.514569	0.100158	0.100158
1.100000	-0.077757	0.256529	-0.203556	0.505854	0.101773	0.101773
1.150000	-0.102942	0.246724	-0.181014	0.497385	0.103403	0.103403
1.200000	-0.125294	0.237436	-0.160327	0.489165	0.105044	0.105044
1.250000	-0.145165	0.228629	-0.141317	0.481195	0.106692	0.106692
1.300000	-0.162856	0.220270	-0.123829	0.473475	0.108341	0.108341
1.350000	-0.178625	0.212331	-0.107726	0.466004	0.109988	0.109988
1.400000	-0.192695	0.204787	-0.092888	0.458780	0.111628	0.111628
1.450000	-0.205261	0.197616	-0.079205	0.451800	0.113259	0.113259
1.500000	-0.216494	0.190799	-0.066582	0.445062	0.114875	0.114875
1.550000	-0.226542	0.184318	-0.054931	0.438560	0.116475	0.116475
1.600000	-0.235538	0.178157	-0.044174	0.432291	0.118054	0.118054
1.650000	-0.243600	0.172304	-0.034240	0.426248	0.119611	0.119611
1.700000	-0.250829	0.166746	-0.025063	0.420427	0.121142	0.121142
1.750000	-0.257320	0.161470	-0.016586	0.414822	0.122646	0.122646
1.800000	-0.263152	0.156466	-0.008753	0.409425	0.124120	0.124120
1.850000	-0.268399	0.151724	-0.001515	0.404232	0.125564	0.125564
1.900000	-0.273126	0.147234	0.005172	0.399234	0.126975	0.126975
1.950000	-0.277390	0.142986	0.011352	0.394426	0.128354	0.128354
2.000000	-0.281244	0.138971	0.017061	0.389800	0.129698	0.129698
2.050000	-0.284731	0.135180	0.022336	0.385350	0.131008	0.131008
2.100000	-0.287894	0.131606	0.027209	0.381068	0.132283	0.132283
2.150000	-0.290768	0.128238	0.031709	0.376949	0.133523	0.133523
2.200000	-0.293385	0.125069	0.035865	0.372986	0.134728	0.134728
2.250000	-0.295774	0.122091	0.039702	0.369171	0.135899	0.135899
2.300000	-0.297960	0.119295	0.043243	0.365499	0.137035	0.137035
2.350000	-0.299966	0.116673	0.046511	0.361964	0.138137	0.138137
2.400000	-0.301812	0.114218	0.049525	0.358560	0.139206	0.139206
2.450000	-0.303514	0.111921	0.052304	0.355280	0.140243	0.140243
2.500000	-0.305090	0.109776	0.054866	0.352119	0.141247	0.141247
2.550000	-0.306552	0.107773	0.057227	0.349072	0.142221	0.142221
2.600000	-0.307912	0.105907	0.059401	0.346134	0.143164	0.143164
2.650000	-0.309182	0.104169	0.061403	0.343300	0.144077	0.144077
2.700000	-0.310371	0.102553	0.063246	0.340564	0.144963	0.144963
2.750000	-0.311487	0.101051	0.064941	0.337923	0.145820	0.145820
2.800000	-0.312537	0.099658	0.066500	0.335371	0.146651	0.146651
2.850000	-0.313529	0.098365	0.067934	0.332906	0.147456	0.147456
2.900000	-0.314467	0.097168	0.069251	0.330523	0.148236	0.148236
2.950000	-0.315358	0.096061	0.070461	0.328218	0.148993	0.148993
3.000000	-0.316204	0.095037	0.071572	0.325988	0.149726	0.149726
3.050000	-0.317011	0.094090	0.072592	0.323829	0.150436	0.150436
3.100000	-0.317782	0.093217	0.073529	0.321739	0.151126	0.151126
3.150000	-0.318519	0.092411	0.074387	0.319713	0.151795	0.151795

A.4 Pulses for refocusing

Consider a system of q fully-coupled qubits where we seek to refocus all the one-qubit interactions and retain one single two-qubit interaction. This is most efficiently achieved by assigning the two coupled qubits to the Walsh function W_1, with the remaining qubits assigned from W_2 up to W_{q-1} in sequence. As W_n contains n sign changes it requires n π pulses when n is even, and $n+1$ pulses when n is odd, with the additional pulse needed to restore the Hamiltonian to its original sign.

The overall number of pulse required is then obtained by summing these pulse counts from $n = 1$ to $q-1$, remembering to include W_1 twice, giving a total of

$$\frac{q(q-1)}{2} + \left\lceil \frac{q-1}{2} \right\rceil + 2 \leq \frac{q^2}{2} + 2.$$

Thus the total number of pulses required to retain a single two-qubit interaction is approximately $q^2/2$.

A.5 Longer range couplings

In the main text we describe a method for implementing a desired coupling pattern in an engineered system containing only nearest-neighbour couplings. While longer range couplings are likely to be significantly weaker than nearest neighbour couplings, they will not in general be zero, and so could lead to significant errors. Fortuitously our control scheme also refocuses next-nearest-neighbour couplings, across the diagonals of each square, which are likely to be the biggest error couplings. Here we consider the problem of refocussing longer range error couplings, which can be achieved using larger numbers of colouring patterns each of which contains more colours.

We begin by considering the case of error couplings between qubits separated by two edges horizontally or vertically (qubits separated by one horizontal and one vertical edge give rise to the diagonal error couplings considered previously). As before we will first colour the horizontal edges and then the vertical edges. When colouring horizontal edges we now have to divide the qubits into *three* groups of rows, rather than two, so that members of each group are at least three rows apart. Within each row a further problem arises, as we cannot directly retain couplings along two sequential horizontal edges without also retaining the error coupling between the two end qubits. Instead we have to use two separate colourings, retaining the two edges separately. This is most simply achieved by retaining odd and even numbered edges in separate steps. Within each row it is necessary to use three colours so that a colour is never repeated two qubits apart.

Putting this together we use two colouring patterns for the horizontal edges, and two for the vertical edges, making four patterns overall. Each pattern requires three separate colours for each of three sets of rows or columns, making nine colours in total. As before all diagonal error couplings will be automatically refocussed if the corresponding horizontal and vertical errors are refocussed.

This approach can be generalised to error couplings over any distance: to correctly handle all couplings between qubits n horizontal or vertical edges apart it is sufficient to use $2n$ colouring patterns, each of which has $(n+1)^2$ different colours. For the simplest case of nearest-neighbour couplings we have $n = 1$ and so two different four-colourings suffice, as described in the main text.

A.6 Second-order perturbation theory of coupled two transmons

Here we consider diagonalising the following coupled two-qubit Hamiltonian,

$$\begin{aligned}
\hat{\mathcal{H}} &= \hat{\mathcal{H}}_0 + \hat{V}, && \text{(A.1)}\\
\hat{\mathcal{H}}_0 &= \hbar \sum_{i=1,2} (\omega_i \hat{a}_i^\dagger \hat{a}_i + \frac{\alpha_i}{2} \hat{a}_i^\dagger \hat{a}_i^\dagger \hat{a}_i \hat{a}_i), && \text{(A.2)}\\
\hat{V} &= \hbar J (\hat{a}_1^\dagger \hat{a}_2 + \hat{a}_1 \hat{a}_2^\dagger). && \text{(A.3)}
\end{aligned}$$

The aim of this section is to give the analytical expression of the following diagonalisation using the second-order perturbation theory,

$$\hat{\mathcal{H}} = \hat{P}^\dagger \hat{\mathcal{H}}_D \hat{P} \approx \hat{P}^{(2)\dagger} \hat{\mathcal{H}}_D \hat{P}^{(2)}. \qquad \text{(A.4)}$$

where diagonalised matrix $\hat{\mathcal{H}}_D$ and the transformation matrix $\hat{P}$ are approximated to the second order by $\hat{\mathcal{H}}_D^{(2)}$ and $\hat{P}^{(2)}$.

According to the second-order perturbation theory, the eigenenergies and eigenvectors can be expressed as follows,

$$\begin{aligned}
E_n^{(2)} &= E_n^{(0)} + \sum_{m\neq n} \frac{|\langle m^{(0)}| \hat{V} |n^{(0)}\rangle|^2}{E_n^{(0)} - E_m^{(0)}}, && \text{(A.5)}\\
|n^{(2)}\rangle &= |n^{(0)}\rangle + \sum_{m\neq n} \frac{\langle m^{(0)}| \hat{V} |n^{(0)}\rangle}{E_n^{(0)} - E_m^{(0)}} |m\rangle \\
&+ \sum_{m\neq n} \sum_{k\neq n} \frac{\langle m^{(0)}| \hat{V} |k^{(0)}\rangle \langle k^{(0)}| \hat{V} |n^{(0)}\rangle}{(E_n^{(0)} - E_k^{(0)})(E_n^{(0)} - E_m^{(0)})} |m^{(0)}\rangle, && \text{(A.6)}
\end{aligned}$$

where $E_n^{(0)}$ and $|n^{(0)}\rangle$ are the eigenenergies and the eigenvectors of the unpurturbed Hamiltonian $\hat{\mathcal{H}}_0$.

The second-order diagonalised Hamiltonian $\hat{\mathcal{H}_D}^{(2)}$ and the transformation matrix $\hat{P}^{(2)}$ can be reconstructed by $E_n^{(2)}$ and $|n^{(2)}\rangle$,

$$\hat{\mathcal{H}}_D^{(2)} = \mathrm{diag}(E_{00}^{(2)}, E_{01}^{(2)}, E_{02}^{(2)}, E_{10}^{(2)}, E_{11}^{(2)}, E_{12}^{(2)}, E_{20}^{(2)}, E_{21}^{(2)}, E_{22}^{(2)}) \tag{A.7}$$

$$E_{00}^{(2)} = \hbar\omega_{00}^{(2)} = E_{00}^{(0)} \tag{A.8}$$

$$E_{01}^{(2)} = \hbar\omega_{01}^{(2)} = E_{01}^{(0)} - \frac{J^2}{\Delta} \tag{A.9}$$

$$E_{02}^{(2)} = \hbar\omega_{02}^{(2)} = E_{02}^{(0)} - \frac{J^2}{\Delta - \alpha_2} \tag{A.10}$$

$$E_{10}^{(2)} = \hbar\omega_{10}^{(2)} = E_{10}^{(0)} + \frac{J^2}{\Delta} \tag{A.11}$$

$$E_{11}^{(2)} = \hbar\omega_{11}^{(2)} = E_{11}^{(0)} - \frac{2J^2(\alpha_1 + \alpha_2)}{(\Delta + \alpha_1)(\alpha_2 - \Delta)} = E_{11}^{(0)} + \zeta \tag{A.12}$$

$$E_{12}^{(2)} = \hbar\omega_{12}^{(2)} = E_{12}^{(0)} + \Big(\frac{3J^2}{\Delta + 2\alpha_1} - \frac{4J^2}{\Delta + \alpha_1 - \alpha_2}\Big) \tag{A.13}$$

$$E_{20}^{(2)} = \hbar\omega_{20}^{(2)} = E_{20}^{(0)} + \frac{J^2}{\Delta + \alpha_1} \tag{A.14}$$

$$E_{21}^{(2)} = \hbar\omega_{21}^{(2)} = E_{21}^{(0)} + \Big(-\frac{3J^2}{\Delta + 2\alpha_1} + \frac{4J^2}{\Delta + \alpha_1 - \alpha_2}\Big) \tag{A.15}$$

$$E_{22}^{(2)} = \hbar\omega_{22}^{(2)} = E_{22}^{(0)} + \Big(\frac{6J^2}{\Delta + \alpha_1 - 2\alpha_2} - \frac{6J^2}{\Delta + 2\alpha_1 - \alpha_2}\Big) \tag{A.16}$$

where $\Delta = \omega_1 - \omega_2$,

$$P_{24} = -P_{42} = \sin\alpha,\ P_{22} = -P_{44} = \cos\alpha, \tag{A.17}$$

$$P_{68} = -P_{86} = \sin\beta,\ P_{66} = -P_{88} = \cos\beta, \tag{A.18}$$

$$P_{33} = \frac{1}{\Sigma_1},\ P_{53} = -\frac{1}{\Sigma_1}\cdot\frac{\sqrt{2}J}{\Delta - \alpha_2},\ P_{73} = \frac{1}{\Sigma_1}\cdot\frac{\zeta}{2\Delta + \alpha_1 - \alpha_2}, \tag{A.19}$$

$$P_{35} = \frac{1}{\Sigma_2}\cdot\frac{\sqrt{2}J}{\Delta - \alpha_2},\ P_{55} = \frac{1}{\Sigma_2},\ P_{75} = -\frac{1}{\Sigma_2}\cdot\frac{\sqrt{2}J}{\Delta + \alpha_1}, \tag{A.20}$$

$$P_{37} = -\frac{1}{\Sigma_3}\cdot\frac{\zeta}{2\Delta + \alpha_1 - \alpha_2}\ P_{57} = \frac{1}{\Sigma_3}\cdot\frac{\sqrt{2}J}{\Delta + \alpha_1},\ P_{77} = \frac{1}{\Sigma_3}, \tag{A.21}$$

where P_{mn} is the (m,n)th element of $\hat{P}^{(2)}$, $\alpha = \arctan\frac{J}{\Delta}$, $\beta = \arctan\frac{2J}{\Delta+\alpha_1-\alpha_2}$ and,

$$\Sigma_1 = \sqrt{1+\Big(\frac{\sqrt{2}J}{\Delta-\alpha_2}\Big)^2+\Big(\frac{\zeta}{2\Delta+\alpha_1-\alpha_2}\Big)^2}, \tag{A.22}$$

$$\Sigma_2 = \sqrt{1+\Big(\frac{\sqrt{2}J}{\Delta-\alpha_2}\Big)^2+\Big(\frac{\sqrt{2}J}{\Delta+\alpha_1}\Big)^2}, \tag{A.23}$$

$$\Sigma_3 = \sqrt{1+\Big(\frac{\sqrt{2}J}{\Delta+\alpha_1}\Big)^2+\Big(\frac{\zeta}{2\Delta+\alpha_1-\alpha_2}\Big)^2}. \tag{A.24}$$

Using the diagonalised Hamiltonian and its transformation matrix, the time evolution of a two-qubit wave function can be approximated by,

$$\begin{aligned} |\psi(t)\rangle &= \exp\left(-\frac{i\hat{\mathcal{H}}t}{\hbar}\right)|\psi(0)\rangle = \hat{P}^\dagger \exp\left(-\frac{i\hat{\mathcal{H}}_D t}{\hbar}\right)\hat{P}\,|\psi(0)\rangle \\ &\approx \hat{P}^{(2)\dagger}\exp\left(-\frac{i\hat{\mathcal{H}}_D^{(2)}t}{\hbar}\right)\hat{P}^{(2)}\,|\psi(0)\rangle = \hat{U}^{(2)}(t)\,|\psi(0)\rangle = |\psi^{(2)}(t)\rangle\,, \end{aligned} \tag{A.25}$$

and the expectation values of measurement operators $\hat{\sigma}\otimes\hat{I}$ ($\hat{\sigma} = \hat{X}, \hat{Y}, \hat{Z}$) in the rotating frame of both qubits can be described as,

$$\langle\hat{\sigma}\otimes\hat{I}\rangle^{(2)}(t) = \langle\psi^{(2)}(t)|\,\hat{U}_{rot}^{(2)}(t)(\hat{\sigma}\otimes\hat{I})\hat{U}_{rot}^{(2)\dagger}(t)\,|\psi^{(2)}(t)\rangle \tag{A.26}$$

$$= \langle\psi(0)|\,\hat{U}^{(2)\dagger}(t)(\hat{\sigma}\otimes\hat{I})\hat{U}^{(2)}(t)\,|\psi(0)\rangle\,, \tag{A.27}$$

$$\hat{U}_{rot}^{(2)}(t) = \exp\left(-i\frac{\omega_{10}^{(2)}t}{2}\hat{Z}\hat{I}-i\frac{\omega_{01}^{(2)}t}{2}\hat{I}\hat{Z}\right), \tag{A.28}$$

where $\hbar\omega_{mn}^{(2)} = \langle m,n|\,\hat{\mathcal{H}}_D^{(2)}\,|m,n\rangle$. In the case of the state-dependent Ramsey interferometry experiment, we set the initial state was set to $|\psi(0)\rangle = |+,0\rangle$ or $|+,1\rangle$,

$$\langle \hat{X}\otimes\hat{I}\rangle_g^{(2)}(t) = \langle +,0|\,\hat{U}^{(2)\dagger}(t)(\hat{X}\otimes\hat{I})\hat{U}^{(2)}(t)\,|+,0\rangle$$

$$= \cos^2\theta\cos\frac{\zeta t}{2} + \sin^2\theta\cos\left(\frac{\zeta}{2} - \omega_{01}^{(2)} + \omega_{10}^{(2)}\right)t \tag{A.29}$$

$$\approx \cos^2\theta\cos\frac{\zeta t}{2}$$

$$\langle \hat{X}\otimes\hat{I}\rangle_e^{(2)}(t) = \langle +,1|\,\hat{U}^{(2)\dagger}(t)(\hat{X}\otimes\hat{I})\hat{U}^{(2)}(t)\,|+,1\rangle$$

$$= P_{35}^2\Big[\cos^2\theta\cos\left(\frac{\zeta}{2} + \omega_{02}^{(2)} - \omega_{11}^{(2)}\right)t \tag{A.30}$$

$$+ \sin^2\theta\cos\left(\frac{\zeta}{2} + \omega_{01}^{(2)} + \omega_{02}^{(2)} - \omega_{10}^{(2)} - \omega_{11}^{(2)}\right)t\Big]$$

$$+ P_{55}^2\Big[\cos^2\theta\cos\left(\frac{\zeta}{2}\right)t + \sin^2\theta\cos\left(\frac{\zeta}{2} + \omega_{01}^{(2)} - \omega_{10}^{(2)}\right)t\Big] \tag{A.31}$$

$$+ P_{75}^2\Big[\cos^2\theta\cos\left(\frac{\zeta}{2} + \omega_{20}^{(2)} - \omega_{11}^{(2)}\right)t \tag{A.32}$$

$$+ \sin^2\theta\cos\left(\frac{\zeta}{2} + \omega_{01}^{(2)} + \omega_{20}^{(2)} - \omega_{10}^{(2)} - \omega_{11}^{(2)}\right)t\Big]$$

$$\approx P_{55}^2\cos^2\theta\cos\left(\frac{\zeta}{2}\right)t + P_{75}^2\cos^2\theta\cos\left(\frac{\zeta}{2} + \omega_{20}^{(2)} - \omega_{11}^{(2)}\right)t$$

$$\begin{aligned}
\langle \hat{Y}\otimes\hat{I}\rangle_g^{(2)}(t) &= \langle +,0|\,\hat{U}^{(2)\dagger}(t)(\hat{Y}\otimes\hat{I})\hat{U}^{(2)}(t)\,|+,0\rangle \\
&= \cos^2\theta\sin\frac{\zeta t}{2}+\sin^2\theta\sin\Big(\frac{\zeta}{2}-\omega_{01}^{(2)}+\omega_{10}^{(2)}\Big)t \qquad (A.33)\\
&\approx \cos^2\theta\sin\frac{\zeta t}{2}\\
\langle \hat{Y}\otimes\hat{I}\rangle_e^{(2)}(t) &= \langle +,1|\,\hat{U}^{(2)\dagger}(t)(\hat{Y}\otimes\hat{I})\hat{U}^{(2)}(t)\,|+,1\rangle \\
&= -P_{35}^2\Big[\cos^2\theta\sin\Big(\frac{\zeta}{2}+\omega_{02}^{(2)}-\omega_{11}^{(2)}\Big)t \qquad (A.34)\\
&+ \sin^2\theta\sin\Big(\frac{\zeta}{2}+\omega_{01}^{(2)}+\omega_{02}^{(2)}-\omega_{10}^{(2)}-\omega_{11}^{(2)}\Big)t\Big]\\
&- P_{55}^2\Big[\cos^2\theta\sin\Big(\frac{\zeta}{2}\Big)t+\sin^2\theta\sin\Big(\frac{\zeta}{2}+\omega_{01}^{(2)}-\omega_{10}^{(2)}\Big)t\Big] \qquad (A.35)\\
&- P_{75}^2\Big[\cos^2\theta\sin\Big(\frac{\zeta}{2}+\omega_{20}^{(2)}-\omega_{11}^{(2)}\Big)t \qquad (A.36)\\
&+ \sin^2\theta\sin\Big(\frac{\zeta}{2}+\omega_{01}^{(2)}+\omega_{20}^{(2)}-\omega_{10}^{(2)}-\omega_{11}^{(2)}\Big)t\Big]\\
&\approx -P_{55}^2\cos^2\theta\sin\Big(\frac{\zeta}{2}\Big)t-P_{75}^2\cos^2\theta\sin\Big(\frac{\zeta}{2}+\omega_{20}^{(2)}-\omega_{11}^{(2)}\Big)t\\
&\qquad (A.37)
\end{aligned}$$

$$\begin{aligned}
\langle \hat{Z}\otimes\hat{I}\rangle_g^{(2)}(t) &= \langle +,0|\,\hat{U}^{(2)\dagger}(t)(\hat{Z}\otimes\hat{I})\hat{U}^{(2)}(t)\,|+,0\rangle \\
&= \sin^2 2\theta\sin^2\Big(\frac{\omega_{01}^{(2)}-\omega_{10}^{(2)}}{2}\Big)t \qquad (A.38)\\
&\approx 0\\
\langle \hat{Z}\otimes\hat{I}\rangle_e^{(2)}(t) &= \langle +,1|\,\hat{U}^{(2)\dagger}(t)(\hat{Z}\otimes\hat{I})\hat{U}^{(2)}(t)\,|+,1\rangle \\
&= -\sin^2 2\theta\sin^2\Big(\frac{\omega_{01}^{(2)}-\omega_{10}^{(2)}}{2}\Big)t+2P_{55}^2P_{75}^2\sin^2\Big(\frac{\omega_{11}^{(2)}-\omega_{20}^{(2)}}{2}\Big)t\\
&+ 2P_{35}^2P_{55}^2\sin^2\Big(\frac{\omega_{02}^{(2)}-\omega_{11}^{(2)}}{2}\Big)t+2P_{75}^2P_{35}^2\sin^2\Big(\frac{\omega_{02}^{(2)}-\omega_{20}^{(2)}}{2}\Big)t \qquad (A.39)\\
&\approx 2P_{55}^2P_{75}^2\sin^2\Big(\frac{\omega_{11}^{(2)}-\omega_{20}^{(2)}}{2}\Big)t
\end{aligned}$$

where $\theta=\arctan\big(\frac{J}{\Delta}\big)$, and the last line for each operator is the approximated result when $\Delta\gg J$ and $P_{55},\ P_{75}\gg P_{35}$.

A.7 Error due to the qubit-qubit dresssing

Following the analytic experession of the Ramsey oscillation introduced in the previous section, the evolution on the first qubit's Bloch sphere can be described by the following three-dimensional vector when the second qubit is in the excited state,

$$\vec{v'} = \begin{pmatrix} x' \\ y' \\ z' \end{pmatrix} = \begin{pmatrix} \cos^2\theta\cos\left(\frac{\zeta t}{2}\right) + P_{75}^2\cos^2\theta\cos\left(\frac{\zeta}{2} + \omega_{20}^{(2)} - \omega_{11}^{(2)}\right)t \\ -P_{55}^2\cos^2\theta\sin\left(\frac{\zeta t}{2}\right) - P_{75}^2\cos^2\theta\sin\left(\frac{\zeta}{2} + \omega_{20}^{(2)} - \omega_{11}^{(2)}\right)t \\ 2P_{55}^2P_{75}^2\sin^2\left(\frac{\omega_{11}^{(2)} - \omega_{20}^{(2)}}{2}t\right) \end{pmatrix}. \tag{A.40}$$

However, in the ideal case, the evolution of the first qubit under the pure Ising interaction is as follows,

$$\vec{v} = \begin{pmatrix} x \\ y \\ z \end{pmatrix} = \begin{pmatrix} \cos\left(\frac{\zeta t}{2}\right) \\ -\sin\left(\frac{\zeta t}{2}\right) \\ 0 \end{pmatrix}. \tag{A.41}$$

The distance between two vectors is,

$$\begin{aligned} d(t) &= |\vec{v'} - \vec{v}| \\ &= \sqrt{(x'-x)^2 + (y'-y)^2 + (z'-z)^2} \\ &\approx \sqrt{[-1 + \cos^2\theta P_{55}^2 + \cos^2\theta P_{75}^2\cos^2(\omega_{11} - \omega_{20})t]^2 + \sin^4(\omega_{11} - \omega_{20})t\cos^4\theta P_{75}^2}, \end{aligned}$$

so the error due to the qubit-qubit dressing can be defined as the average of the deviation over time,

$$\epsilon_d = \overline{d(t)} \tag{A.42}$$

$$\approx 1 - \cos^2\theta P_{55}^2. \tag{A.43}$$

Bibliography

[1] Tyson Jones, Anna Brown, Ian Bush, and Simon C. Benjamin. QuEST and High Performance Simulation of Quantum Computers. *Scientific Reports 2019 9:1*, 9(1):1–11, 7 2019.

[2] Richard P. Feynman. Simulating physics with computers. *International Journal of Theoretical Physics*, 21(6-7):467–488, 6 1982.

[3] Quantum theory, Church-Turing principle and the universal quantum computer. *Royal Society of London A 400*, pages 97–117, 1985.

[4] Seth Lloyd. Universal quantum simulators. *Science*, 273(5278):1073–1078, 8 1996.

[5] Peter W. Shor. Polynomial-time algorithms for prime factorization and discrete logarithms on a quantum computer. *SIAM Review*, 41(2):303–332, 8 1999.

[6] Lov K. Grover. A fast quantum mechanical algorithm for database search. In *Proceedings of the Annual ACM Symposium on Theory of Computing*, volume Part F129452, pages 212–219. Association for Computing Machinery, 7 1996.

[7] J. I. Cirac and P. Zoller. Quantum computations with cold trapped ions. *Physical Review Letters*, 74(20):4091–4094, 5 1995.

[8] C. J. Ballance, T. P. Harty, N. M. Linke, M. A. Sepiol, and D. M. Lucas. High-Fidelity Quantum Logic Gates Using Trapped-Ion Hyperfine Qubits. *Physical Review Letters*, 117(6):060504, 8 2016.

[9] C Monroe, W C Campbell, L.-M Duan, Z.-X Gong, A V Gorshkov, P W Hess, R Islam, K Kim, N M Linke, G Pagano, P Richerme, C Senko, and N Y Yao. Programmable quantum simulations of spin systems with trapped ions. *Reviews of Modern Physics*, 93, 2021.

[10] Y. Nakamura, Yu A. Pashkin, and J. S. Tsai. Coherent control of macroscopic quantum states in a single-Cooper-pair box. *Nature*, 398(6730):786–788, 4 1999.

[11] A. Wallraff, D. I. Schuster, A. Blais, L. Frunzio, R. S. Huang, J. Majer, S. Kumar, S. M. Girvin, and R. J. Schoelkopf. Strong coupling of a single photon to a superconducting qubit using circuit quantum electrodynamics. *Nature*, 431(7005):162–167, 9 2004.

[12] J.A. Jones. NMR Quantum Computation: A Critical Evaluation. *Fortschritte der Physik*, 48(9-11):909–924, 9 2000.

[13] E. Knill, R. Laflamme, R. Martinez, and C. Negrevergne. Benchmarking quantum computers: The five-qubit error correcting code. *Physical Review Letters*, 86(25):5811–5814, 6 2001.

[14] E. Knill, R. Laflamme, and G. J. Milburn. A scheme for efficient quantum computation with linear optics. *Nature*, 409(6816):46–52, 1 2001.

[15] B E Kane. A silicon-based nuclear spin quantum computer. *Nature*, 393:133–137, 1998.

[16] D. Jaksch, H. J. Briegel, J. I. Cirac, C. W. Gardiner, and P. Zoller. Entanglement of atoms via cold controlled collisions. *Physical Review Letters*, 82(9):1975–1978, 3 1999.

[17] Frank Arute and others. Quantum supremacy using a programmable superconducting processor. *Nature*, 574:505–511, 2019.

[18] Han Sen Zhong, Hui Wang, Yu Hao Deng, Ming Cheng Chen, Li Chao Peng, Yi Han Luo, Jian Qin, Dian Wu, Xing Ding, Yi Hu, Peng Hu, Xiao Yan Yang, Wei Jun Zhang, Hao Li, Yuxuan Li, Xiao Jiang, Lin Gan, Guangwen Yang, Lixing You, Zhen Wang, Li Li, Nai Le Liu, Chao Yang Lu, and Jian Wei Pan. Quantum computational advantage using photons. *Science*, 370(6523):1460–1463, 12 2021.

[19] Nissim Ofek, Andrei Petrenko, Reinier Heeres, Philip Reinhold, Zaki Leghtas, Brian Vlastakis, Yehan Liu, Luigi Frunzio, S. M. Girvin, L. Jiang, Mazyar Mirrahimi, M. H. Devoret, and R. J. Schoelkopf. Extending the lifetime of a quantum bit with error correction in superconducting circuits. *Nature*, 536(7617):441–445, 7 2016.

[20] Zijun Chen, Kevin J. Satzinger, Juan Atalaya, Alexander N. Korotkov, Andrew Dunsworth, Daniel Sank, Chris Quintana, Matt McEwen, Rami Barends, Paul V. Klimov, Sabrina Hong, Cody Jones, Andre Petukhov, Dvir Kafri, Sean Demura, Brian Burkett, Craig Gidney, Austin G. Fowler, Alexandru Paler, Harald Putterman, Igor Aleiner, Frank Arute, Kunal Arya, Ryan Babbush, Joseph C. Bardin, Andreas Bengtsson, Alexandre Bourassa, Michael Broughton, Bob B. Buckley, David A. Buell, Nicholas Bushnell, Benjamin Chiaro, Roberto Collins, William Courtney, Alan R. Derk, Daniel Eppens, Catherine Erickson, Edward Farhi, Brooks Foxen, Marissa Giustina, Ami Greene, Jonathan A.

Gross, Matthew P. Harrigan, Sean D. Harrington, Jeremy Hilton, Alan Ho, Trent Huang, William J. Huggins, L. B. Ioffe, Sergei V. Isakov, Evan Jeffrey, Zhang Jiang, Kostyantyn Kechedzhi, Seon Kim, Alexei Kitaev, Fedor Kostritsa, David Landhuis, Pavel Laptev, Erik Lucero, Orion Martin, Jarrod R. McClean, Trevor McCourt, Xiao Mi, Kevin C. Miao, Masoud Mohseni, Shirin Montazeri, Wojciech Mruczkiewicz, Josh Mutus, Ofer Naaman, Matthew Neeley, Charles Neill, Michael Newman, Murphy Yuezhen Niu, Thomas E. O'Brien, Alex Opremcak, Eric Ostby, Bálint Pató, Nicholas Redd, Pedram Roushan, Nicholas C. Rubin, Vladimir Shvarts, Doug Strain, Marco Szalay, Matthew D. Trevithick, Benjamin Villalonga, Theodore White, Z. Jamie Yao, Ping Yeh, Juhwan Yoo, Adam Zalcman, Hartmut Neven, Sergio Boixo, Vadim Smelyanskiy, Yu Chen, Anthony Megrant, and Julian Kelly. Exponential suppression of bit or phase errors with cyclic error correction. *Nature 2021 595:7867*, 595(7867):383–387, 7 2021.

[21] John Preskill. Quantum Computing in the NISQ era and beyond. *Quantum*, 2:79, 2018.

[22] Austin G. Fowler, Matteo Mariantoni, John M. Martinis, and Andrew N. Cleland. Surface codes: Towards practical large-scale quantum computation. *Physical Review A*, 86(3):032324, 9 2012.

[23] L Dicarlo, J M Chow, J M Gambetta, Lev S Bishop, B R Johnson, D I Schuster, J Majer, A Blais, L Frunzio, S M Girvin, and R J Schoelkopf. Demonstration of two-qubit algorithms with a superconducting quantum processor. *Nature*, 460, 2009.

[24] Yu Chen, C Neill, P Roushan, N Leung, M Fang, R Barends, J Kelly, B Campbell, Z Chen, B Chiaro, A Dunsworth, E Jeffrey, A Megrant, J Y Mutus, P J J

O'Malley, C M Quintana, D Sank, A Vainsencher, J Wenner, T C White, Michael R Geller, A N Cleland, and John M Martinis. Qubit Architecture with High Coherence and Fast Tunable Coupling. *Phys. Rev. Lett.*, 113:220502, 2014.

[25] Chad Rigetti and Michel Devoret. Fully microwave-tunable universal gates in superconducting qubits with linear couplings and fixed transition frequencies. *Physical Review B - Condensed Matter and Materials Physics*, 81(13):134507, 4 2010.

[26] Hanhee Paik, A. Mezzacapo, Martin Sandberg, D. T. McClure, B. Abdo, A. D. Córcoles, O. Dial, D. F. Bogorin, B. L.T. Plourde, M. Steffen, A. W. Cross, J. M. Gambetta, and Jerry M. Chow. Experimental Demonstration of a Resonator-Induced Phase Gate in a Multiqubit Circuit-QED System. *Physical Review Letters*, 117(25):250502, 12 2016.

[27] Abhinav Kandala, Antonio Mezzacapo, Kristan Temme, Maika Takita, Markus Brink, Jerry M. Chow, and Jay M. Gambetta. Hardware-efficient variational quantum eigensolver for small molecules and quantum magnets. *Nature*, 549(7671):242–246, 9 2017.

[28] Sarah Sheldon, Easwar Magesan, Jerry M. Chow, and Jay M. Gambetta. Procedure for systematically tuning up cross-talk in the cross-resonance gate. *Physical Review A*, 93(6):060302, 6 2016.

[29] Jennifer L. Dodd, Michael A. Nielsen, Michael J. Bremner, and Robert T. Thew. Universal quantum computation and simulation using any entangling Hamiltonian and local unitaries. *Physical Review A*, 65(4):040301, 4 2002.

[30] P.J.J. O'Malley, R. Babbush, I.D. Kivlichan, J. Romero, J.R. McClean, R. Barends, J. Kelly, P. Roushan, A. Tranter, N. Ding, B. Campbell, Y. Chen,

Z. Chen, B. Chiaro, A. Dunsworth, A.G. Fowler, E. Jeffrey, E. Lucero, A. Megrant, J.Y. Mutus, M. Neeley, C. Neill, C. Quintana, D. Sank, A. Vainsencher, J. Wenner, T.C. White, P.V. Coveney, P.J. Love, H. Neven, A. Aspuru-Guzik, and J.M. Martinis. Scalable Quantum Simulation of Molecular Energies. *Physical Review X*, 6(3):031007, 7 2016.

[31] Jarrod R. McClean, Sergio Boixo, Vadim N. Smelyanskiy, Ryan Babbush, and Hartmut Neven. Barren plateaus in quantum neural network training landscapes. *Nature Communications*, 9(1):1–6, 12 2018.

[32] M. Cerezo, Akira Sone, Tyler Volkoff, Lukasz Cincio, and Patrick J. Coles. Cost function dependent barren plateaus in shallow parametrized quantum circuits. *Nature Communications 2021 12:1*, 12(1):1–12, 3 2021.

[33] E. L. Hahn. Spin echoes. *Physical Review*, 80(4):580–594, 11 1950.

[34] Adrian Parra-Rodriguez, Pavel Lougovski, Lucas Lamata, Enrique Solano, and Mikel Sanz. Digital-analog quantum computation. *Phys. Rev. A*, 101:22305, 2020.

[35] Gaurav Bhole, Takahiro Tsunoda, Peter J. Leek, and Jonathan A. Jones. Rescaling Interactions for Quantum Control. *Physical Review Applied*, 13(3):034002, 2 2020.

[36] Takahiro Tsunoda, Gaurav Bhole, Stephen A. Jones, Jonathan A. Jones, and Peter J. Leek. Efficient Hamiltonian programming in qubit arrays with nearest-neighbor couplings. *Physical Review A*, 102(3):032405, 9 2020.

[37] Ana Martin, Lucas Lamata, Enrique Solano, and Mikel Sanz. Digital-analog quantum algorithm for the quantum Fourier transform. *Phys. Rev. Research*, 2, 2020.

[38] F. Lecocq, F. Quinlan, K. Cicak, J. Aumentado, S. A. Diddams, and J. D. Teufel. Control and readout of a superconducting qubit using a photonic link. *Nature*, 591(7851):575–579, 9 2020.

[39] S. Krinner, S. Storz, P. Kurpiers, P. Magnard, J. Heinsoo, R. Keller, J. Lütolf, C. Eichler, and A. Wallraff. Engineering cryogenic setups for 100-qubit scale superconducting circuit systems. *EPJ Quantum Technology*, 6(1):1–29, 12 2019.

[40] J. M. Gambetta, A. A. Houck, and Alexandre Blais. Superconducting qubit with purcell protection and tunable coupling. *Physical Review Letters*, 106(3):030502, 1 2011.

[41] Takahiko Satoh, Yuichiro Matsuzaki, Kosuke Kakuyanagi, William J Munro, Koichi Semba, Hiroshi Yamaguchi, and Shiro Saito. Scalable quantum computation architecture using always-on Ising interactions via quantum feedforward. *Phys. Rev. A*, 91:52329, 2015.

[42] Edward Farhi, Jeffrey Goldstone, and Sam Gutmann. A Quantum Approximate Optimization Algorithm, 2014.

[43] Alberto Peruzzo, Jarrod McClean, Peter Shadbolt, Man Hong Yung, Xiao Qi Zhou, Peter J. Love, Alán Aspuru-Guzik, and Jeremy L. O'Brien. A variational eigenvalue solver on a photonic quantum processor. *Nature Communications*, 5(1):1–7, 7 2014.

[44] Alexandre Blais, Ren Shou Huang, Andreas Wallraff, S. M. Girvin, and R. J. Schoelkopf. Cavity quantum electrodynamics for superconducting electrical circuits: An architecture for quantum computation. *Physical Review A - Atomic, Molecular, and Optical Physics*, 69(6):062320, 6 2004.

[45] Benjamin Schumacher. Quantum coding. *Physical Review A*, 51(4):2738–2747, 4 1995.

[46] Michael A. Nielsen and Isaac L. Chuang. Quantum Computation and Quantum Information: 10th Anniversary Edition. *Cambridge University Press*, 2011.

[47] Herbert Walther, Benjamin T.H. Varcoe, Berthold Georg Englert, and Thomas Becker. Cavity quantum electrodynamics. *Reports on Progress in Physics*, 69(5):1325–1382, 4 2006.

[48] H. Mabuchi and A. C. Doherty. Cavity Quantum Electrodynamics: Coherence in Context. *Science*, 298(5597):1372–1377, 11 2002.

[49] Anton Frisk Kockum, Adam Miranowicz, Simone De Liberato, Salvatore Savasta, and Franco Nori. Ultrastrong coupling between light and matter. *Nature Reviews Physics 2019 1:1*, 1(1):19–40, 1 2019.

[50] Bharath Kannan, Max J. Ruckriegel, Daniel L. Campbell, Anton Frisk Kockum, Jochen Braumüller, David K. Kim, Morten Kjaergaard, Philip Krantz, Alexander Melville, Bethany M. Niedzielski, Antti Vepsäläinen, Roni Winik, Jonilyn L. Yoder, Franco Nori, Terry P. Orlando, Simon Gustavsson, and William D. Oliver. Waveguide quantum electrodynamics with superconducting artificial giant atoms. *Nature*, 583(7818):775–779, 7 2020.

[51] Jens Koch, Terri M. Yu, Jay Gambetta, A. A. Houck, D. I. Schuster, J. Majer, Alexandre Blais, M. H. Devoret, S. M. Girvin, and R. J. Schoelkopf. Charge-insensitive qubit design derived from the Cooper pair box. *Physical Review A - Atomic, Molecular, and Optical Physics*, 76(4):042319, 10 2007.

[52] Morten Kjaergaard, Mollie E Schwartz, Jochen Braumüller, Philip Krantz, Joel I.-J. Wang, Simon Gustavsson, and William D Oliver. Superconducting Qubits:

Current State of Play. *Annual Review of Condensed Matter Physics*, 11(1):369–395, 2020.

[53] Petar Jurcevic, Ali Javadi-Abhari, Lev S. Bishop, Isaac Lauer, Daniela F. Bogorin, Markus Brink, Lauren Capelluto, Oktay Günlük, Toshinari Itoko, Naoki Kanazawa, Abhinav Kandala, George A. Keefe, Kevin Krsulich, William Landers, Eric P. Lewandowski, Douglas T. McClure, Giacomo Nannicini, Adinath Narasgond, Hasan M. Nayfeh, Emily Pritchett, Mary Beth Rothwell, Srikanth Srinivasan, Neereja Sundaresan, Cindy Wang, Ken X. Wei, Christopher J. Wood, Jeng-Bang Yau, Eric J. Zhang, Oliver E. Dial, Jerry M. Chow, and Jay M. Gambetta. Demonstration of quantum volume 64 on a superconducting quantum computing system. *Quantum Science and Technology*, 6(2), 8 2020.

[54] Joseph Rahamim. *Development of a coaxial circuit QED architecture for quantum computing - ORA - Oxford University Research Archive*. PhD thesis, University of Oxford, Oxford, 2019.

[55] Jay Gambetta, Alexandre Blais, D. I. Schuster, A. Wallraff, L. Frunzio, J. Majer, M. H. Devoret, S. M. Girvin, and R. J. Schoelkopf. Qubit-photon interactions in a cavity: Measurement-induced dephasing and number splitting. *Physical Review A - Atomic, Molecular, and Optical Physics*, 74(4):042318, 10 2006.

[56] Alexandre Blais, Arne L. Grimsmo, S.M. Girvin, and Andreas Wallraff. Circuit quantum electrodynamics. *Reviews of Modern Physics*, 93(2):025005, 5 2021.

[57] Nicolas Didier, Eyob A. Sete, Marcus P. Da Silva, and Chad Rigetti. Analytical modeling of parametrically modulated transmon qubits. *Physical Review A*, 97(2):022330, 2 2018.

[58] VoolUri and DevoretMichel. Introduction to quantum electromagnetic circuits. *International Journal of Circuit Theory and Applications*, 45(7):897–934, 7 2017.

[59] A. A. Houck, J. A. Schreier, B. R. Johnson, J. M. Chow, Jens Koch, J. M. Gambetta, D. I. Schuster, L. Frunzio, M. H. Devoret, S. M. Girvin, and R. J. Schoelkopf. Controlling the spontaneous emission of a superconducting transmon qubit. *Physical Review Letters*, 101(8):080502, 8 2008.

[60] Forschungszentrum Julich. Quantum Information Processing Lecture Notes. Technical report, FORSCHUNGSZENTRUM JULICH, 2013.

[61] J A Jones. Quantum Computing with NMR. *Prog. NMR Spectrosc.*, 59:91–120, 2011.

[62] Lorenza Viola, Emanuel Knill, and Seth Lloyd. Dynamical decoupling of open quantum systems. *Physical Review Letters*, 82(12):2417–2421, 3 1999.

[63] J. A. Jones and E. Knill. Efficient Refocusing of One-Spin and Two-Spin Interactions for NMR Quantum Computation. *Journal of Magnetic Resonance*, 141(2):322–325, 12 1999.

[64] Debbie W. Leung, Isaac L. Chuang, Fumiko Yamaguchi, and Yoshihisa Yamamoto. Efficient implementation of coupled logic gates for quantum computation. *Physical Review A - Atomic, Molecular, and Optical Physics*, 61(4):7, 3 2000.

[65] Tanja B C Behrle. Simulation and Measurements of Single and Coupled Coaxial lbits. *Master thesis*, 2017.

[66] X. Y. Jin, A. Kamal, A. P. Sears, T. Gudmundsen, D. Hover, J. Miloshi, R. Slattery, F. Yan, J. Yoder, T. P. Orlando, S. Gustavsson, and W. D. Oliver. Thermal and Residual Excited-State Population in a 3D Transmon Qubit. *Physical Review Letters*, 114(24):240501, 6 2015.

[67] T. Yamamoto, K. Inomata, M. Watanabe, K. Matsuba, T. Miyazaki, W. D. Oliver, Y. Nakamura, and J. S. Tsai. Flux-driven Josephson parametric amplifier. *Applied Physics Letters*, 93(4):042510, 7 2008.

[68] C. Macklin, K. O'Brien, D. Hover, M. E. Schwartz, V. Bolkhovsky, X. Zhang, W. D. Oliver, and I. Siddiqi. A nearâ€”quantum-limited Josephson traveling-wave parametric amplifier. *Science*, 350(6258):307–310, 10 2015.

[69] D. I. Schuster, A. A. Houck, J. A. Schreier, A. Wallraff, J. M. Gambetta, A. Blais, L. Frunzio, J. Majer, B. Johnson, M. H. Devoret, S. M. Girvin, and R. J. Schoelkopf. Resolving photon number states in a superconducting circuit. *Nature*, 445(7127):515–518, 2 2007.

[70] A. A. Houck, D. I. Schuster, J. M. Gambetta, J. A. Schreier, B. R. Johnson, J. M. Chow, L. Frunzio, J. Majer, M. H. Devoret, S. M. Girvin, and R. J. Schoelkopf. Generating single microwave photons in a circuit. *Nature*, 449(7160):328–331, 9 2007.

[71] E. Knill, D. Leibfried, R. Reichle, J. Britton, R. B. Blakestad, J. D. Jost, C. Langer, R. Ozeri, S. Seidelin, and D. J. Wineland. Randomized benchmarking of quantum gates. *Physical Review A - Atomic, Molecular, and Optical Physics*, 77(1):012307, 1 2008.

[72] Norman F. Ramsey. A molecular beam resonance method with separated oscillating fields. *Physical Review*, 78(6):695–699, 6 1950.

[73] F. Motzoi, J. M. Gambetta, P. Rebentrost, and F. K. Wilhelm. Simple Pulses for Elimination of Leakage in Weakly Nonlinear Qubits. *Physical Review Letters*, 103(11):110501, 9 2009.

[74] Navin Khaneja, Timo Reiss, Cindie Kehlet, Thomas Schulte-Herbrüggen, and Steffen J. Glaser. Optimal control of coupled spin dynamics: Design of NMR pulse sequences by gradient ascent algorithms. *Journal of Magnetic Resonance*, 172(2):296–305, 2 2005.

[75] Erik Lucero, Julian Kelly, Radoslaw C. Bialczak, Mike Lenander, Matteo Mariantoni, Matthew Neeley, A. D. O'Connell, Daniel Sank, H. Wang, Martin Weides, James Wenner, Tsuyoshi Yamamoto, A. N. Cleland, and John M. Martinis. Reduced phase error through optimized control of a superconducting qubit. *Physical Review A - Atomic, Molecular, and Optical Physics*, 82(4):042339, 10 2010.

[76] Easwar Magesan, Jay M. Gambetta, and Joseph Emerson. Characterizing quantum gates via randomized benchmarking. *Physical Review A - Atomic, Molecular, and Optical Physics*, 85(4):042311, 4 2012.

[77] J. M. Chow, J. M. Gambetta, L. Tornberg, Jens Koch, Lev S. Bishop, A. A. Houck, B. R. Johnson, L. Frunzio, S. M. Girvin, and R. J. Schoelkopf. Randomized benchmarking and process tomography for gate errors in a solid-state qubit. *Physical Review Letters*, 102(9):090502, 3 2009.

[78] R. Barends, J. Kelly, A. Megrant, A. Veitia, D. Sank, E. Jeffrey, T. C. White, J. Mutus, A. G. Fowler, B. Campbell, Y. Chen, Z. Chen, B. Chiaro, A. Dunsworth, C. Neill, P. O'Malley, P. Roushan, A. Vainsencher, J. Wenner, A. N. Korotkov, A. N. Cleland, and John M. Martinis. Superconducting

quantum circuits at the surface code threshold for fault tolerance. *Nature*, 508(7497):500–503, 4 2014.

[79] Scott Aaronson and Daniel Gottesman. Improved simulation of stabilizer circuits. *Physical Review A - Atomic, Molecular, and Optical Physics*, 70(5 A):052328, 11 2004.

[80] Yunseong Nam, Jwo Sy Chen, Neal C. Pisenti, Kenneth Wright, Conor Delaney, Dmitri Maslov, Kenneth R. Brown, Stewart Allen, Jason M. Amini, Joel Apisdorf, Kristin M. Beck, Aleksey Blinov, Vandiver Chaplin, Mika Chmielewski, Coleman Collins, Shantanu Debnath, Kai M. Hudek, Andrew M. Ducore, Matthew Keesan, Sarah M. Kreikemeier, Jonathan Mizrahi, Phil Solomon, Mike Williams, Jaime David Wong-Campos, David Moehring, Christopher Monroe, and Jungsang Kim. Ground-state energy estimation of the water molecule on a trapped-ion quantum computer. *npj Quantum Information*, 6(1):1–6, 12 2020.

[81] Google AI Quantum. Hartree-Fock on a superconducting qubit quantum computer. *Science*, 369(6507):1084–1089, 8 2020.

[82] Ying Li and Simon C. Benjamin. Efficient Variational Quantum Simulator Incorporating Active Error Minimization. *Physical Review X*, 7(2):021050, 6 2017.

[83] Kristan Temme, Sergey Bravyi, and Jay M. Gambetta. Error Mitigation for Short-Depth Quantum Circuits. *Physical Review Letters*, 119(18):180509, 11 2017.

[84] Abhinav Kandala, Kristan Temme, Antonio D. Córcoles, Antonio Mezzacapo, Jerry M. Chow, and Jay M. Gambetta. Error mitigation extends the com-

putational reach of a noisy quantum processor. *Nature*, 567(7749):491–495, 3 2019.

[85] Jarrod R. McClean, Jonathan Romero, Ryan Babbush, and Alán Aspuru-Guzik. The theory of variational hybrid quantum-classical algorithms. *New Journal of Physics*, 18(2):23023, 2 2016.

[86] Dave Wecker, Matthew B. Hastings, and Matthias Troyer. Progress towards practical quantum variational algorithms. *Physical Review A - Atomic, Molecular, and Optical Physics*, 92(4):042303, 10 2015.

[87] Suguru Endo, Simon C. Benjamin, and Ying Li. Practical Quantum Error Mitigation for Near-Future Applications. *Physical Review X*, 8(3):031027, 7 2018.

[88] Tudor Giurgica-Tiron, Yousef Hindy, Ryan LaRose, Andrea Mari, and William J. Zeng. Digital zero noise extrapolation for quantum error mitigation. *Proceedings - IEEE International Conference on Quantum Computing and Engineering, QCE 2020*, pages 306–316, 5 2020.

[89] Xiu-Hao Deng, Yong-Ju Hai, Jun-Ning Li, and Yao Song. Correcting correlated errors for quantum gates in multi-qubit systems using smooth pulse control. 3 2021.

[90] J. A. Jones, M. Mosca, and R. H. Hansen. Implementation of a quantum search algorithm on a quantum computer. *Nature*, 393(6683):344–346, 5 1998.

[91] Lieven M.K. Vandersypen, Matthias Breyta, Gregory Steffen, Costantino S. Yannoni, Mark H. Sherwood, and Isaac L. Chuang. Experimental realization of Shor's quantum factoring algorithm using nuclear magnetic resonance. *Nature*, 414(6866):883–887, 12 2001.

[92] Y. S. Weinstein, M. A. Pravia, E. M. Fortunato, S. Lloyd, and D. G. Cory. Implementation of the quantum Fourier transform. *Physical Review Letters*, 86(9):1889–1891, 2 2001.

[93] K G Beauchamp. *Applications of Walsh and related functions*. Academic Press, 1984.

[94] M. S. Lynn. On the Schur product of H-matrices and non-negative matrices, and related inequalities. *Mathematical Proceedings of the Cambridge Philosophical Society*, 60(3):425–431, 1964.

[95] Ray Freeman, Thomas A. Frenkiel, and Malcolm H. Levitt. Composite Z pulses. *Journal of Magnetic Resonance (1969)*, 44(2):409–412, 8 1981.

[96] Debbie Leung and Debbie W Leung. Simulation and reversal of n-qubit Hamiltonians using Hadamard matrices. *Journal of Modern Optics*, 49(8):1199–1217, 2002.

[97] David Hayes, Steven T. Flammia, and Michael J. Biercuk. Programmable quantum simulation by dynamic Hamiltonian engineering. *New Journal of Physics*, 16(8):083027, 8 2014.

[98] Jonathan Welch, Daniel Greenbaum, Sarah Mostame, and Alan Aspuru-Guzik. Efficient quantum circuits for diagonal unitaries without ancillas. *New Journal of Physics*, 16(3):33040, 3 2014.

[99] Robert G. Bland. The Allocation of Resources by Linear Programming. *Scientific American*, 244(6):126–144, 6 1981.

[100] George B. Dantzig. Reminiscences about the origins of linear programming. *Operations Research Letters*, 1(2):43–48, 4 1982.

[101] Ilan Adler, Mauricio G.C. Resende, Geraldo Veiga, and Narendra Karmarkar. An implementation of Karmarkar's algorithm for linear programming. *Mathematical Programming*, 44(1-3):297–335, 5 1989.

[102] William H Press, Saul A Teukolsky, William T Vetterling, and Brian P Flannery. *Numerical Recipes in C (2nd Ed.): The Art of Scientific Computing.* Cambridge University Press, USA, 1992.

[103] David Collins, K. W. Kim, W. C. Holton, H. Sierzputowska-Gracz, and E. O. Stejskal. NMR quantum computation with indirectly coupled gates. *Physical Review A - Atomic, Molecular, and Optical Physics*, 62(2):4, 7 2000.

[104] Navin Khaneja, Björn Heitmann, Andreas Spörl, Haidong Yuan, Thomas Schulte-Herbrüggen, and Steffen J. Glaser. Shortest paths for efficient control of indirectly coupled qubits. *Physical Review A - Atomic, Molecular, and Optical Physics*, 75(1):012322, 1 2007.

[105] J. A.J. Hall. Towards a practical parallelisation of the simplex method. *Computational Management Science*, 7(2):139–170, 4 2010.

[106] J. K. Kruschke. *Doing Bayesian Data Analysis.* Academic Press, Oxford, 2nd edition edition, 11 2014.

[107] P. A. Spring, T. Tsunoda, B. Vlastakis, and P. J. Leek. Modeling Enclosures for Large-Scale Superconducting Quantum Circuits. *Physical Review Applied*, 14(2):024061, 8 2020.

[108] Pinaki Sengupta and Leonid P Pryadko. Scalable Design of Tailored Soft Pulses for Coherent Control. *Phys. Rev. Lett.*, 95:37202, 2005.

[109] Amrit De and Leonid P Pryadko. Universal Set of Scalable Dynamically Corrected Gates for Quantum Error Correction with Always-on Qubit Couplings. *Phys. Rev. Lett.*, 110:70503, 2013.

[110] Amrit De and Leonid P Pryadko. Dynamically corrected gates for qubits with always-on Ising couplings: Error model and fault tolerance with the toric code. *Phys. Rev. A*, 89:32332, 2014.

[111] J J L Morton, A M Tyryshkin, A Ardavan, S C Benjamin, K Porfyrakis, S A Lyon, and G A D Briggs. Bang-bang control of fullerene qubits using ultrafast phase gates. *Nature Physics*, 2(1):40–43, 1 2006.

[112] Kenneth Appel and Wolfgang Haken. Solution of the Four-Color-Map Problem. *Sci. Am.*, 237(4):108–121, 1977.

[113] S. Filipp, P. Maurer, P. J. Leek, M. Baur, R. Bianchetti, J. M. Fink, M. Göppl, L. Steffen, J. M. Gambetta, A. Blais, and A. Wallraff. Two-qubit state tomography using a joint dispersive readout. *Physical Review Letters*, 102(20):200402, 5 2009.

[114] J. M. Chow, L. Dicarlo, J. M. Gambetta, A. Nunnenkamp, Lev S. Bishop, L. Frunzio, M. H. Devoret, S. M. Girvin, and R. J. Schoelkopf. Detecting highly entangled states with a joint qubit readout. *Physical Review A - Atomic, Molecular, and Optical Physics*, 81(6):062325, 6 2010.

[115] Robert Raussendorf and Hans J. Briegel. A One-Way Quantum Computer. *Physical Review Letters*, 86(22):5188, 5 2001.

[116] Robert Raussendorf, Daniel E. Browne, and Hans J. Briegel. Measurement-based quantum computation on cluster states. *Physical Review A*, 68(2):022312, 8 2003.

[117] R Raussendorf, J Harrington, and K Goyal. Topological fault-tolerance in cluster state quantum computation. *New Journal of Physics*, 9(6):199, 6 2007.

[118] Zaki Leghtas, Gerhard Kirchmair, Brian Vlastakis, Michel H. Devoret, Robert J. Schoelkopf, and Mazyar Mirrahimi. Deterministic protocol for mapping a qubit to coherent state superpositions in a cavity. *Physical Review A*, 87(4):042315, 4 2013.

[119] Reinier W. Heeres, Philip Reinhold, Nissim Ofek, Luigi Frunzio, Liang Jiang, Michel H. Devoret, and Robert J. Schoelkopf. Implementing a universal gate set on a logical qubit encoded in an oscillator. *Nature Communications 2017 8:1*, 8(1):1–7, 7 2017.

[120] Jeffrey M. Epstein, Andrew W. Cross, Easwar Magesan, and Jay M. Gambetta. Investigating the limits of randomized benchmarking protocols. *Physical Review A*, 89(6):062321, 6 2014.